REPORT DOCUMENTATION PAGE

Form Approved
OMB No. 0704-0188

1. REPORT DATE (DD-MM-YYYY) 15-4-2006	2. REPORT TYPE Final	3. DATES COVERED (From - To) 01-06-2002 to 31-5-2005

4. TITLE AND SUBTITLE

Applications of Optical Coherent Transient Technology to Pulse Shaping, Spectral Filtering, Arbitrary Waveform Generation and RF Beamforming

5a. CONTRACT NUMBER

5b. GRANT NUMBER
F49620-02-1-0275

5c. PROGRAM ELEMENT NUMBER

6. AUTHOR(S)
Wm. Randall Babbitt, Mingzhen Tian, and Kelvin Wagner

5d. PROJECT NUMBER

5e. TASK NUMBER

5f. WORK UNIT NUMBER

7. PERFORMING ORGANIZATION NAME(S) AND ADDRESS(ES)

Physics Department, EPS 264   Department of ECE, box 425
Montana State University   University of Colorado
Bozeman, MT 59717-3840   Boulder, CO 80309-0425

8. PERFORMING ORGANIZATION REPORT NUMBER
WRB-041506

9. SPONSORING / MONITORING AGENCY NAME(S) AND ADDRESS(ES)
Dr. Gernot Pomrenke
Air Force Office of Scientific Research
Ballston Common Towers III
4015 Wilson Blvd, Room 713
Arlington VA 22203-1954

10. SPONSOR/MONITOR'S ACRONYM(S)

11. SPONSOR/MONITOR'S REPORT NUMBER(S)
AFRL-SR-AR-TR-06-0150

12. DISTRIBUTION / AVAILABILITY STATEMENT
Approved for public release; distribution unlimited

13. SUPPLEMENTARY NOTES
The views, opinions and/or findings contained in this report are those of the author(s) and should not be construed as an official Department of the Air Force position, policy or decision, unless so designated by other documentation.

14. ABSTRACT

Under research conducted by Montana State University and the University of Colorado, several optical coherent transient (OCT) devices was developed and demonstrated, including pulse shaping, arbitrary waveform generation, optical spectral filtering, time integrating correlator, Doppler shifted arrays, and optical beam scanning. OCT's are particularly well suited for RF photonic processing because of their large bandwidths (tens to hundreds of GHz), spectral resolution well below a MHz, and time–bandwidth products (TBP) greater than 106. The advancement of OCT technologies is dependent on the development of supporting technologies. Under this grant, several supporting technologies were developed and demonstrated, including high efficiency OCT programming, tapered semi-conductor amplifiers at 793nm, cascaded injection locked amplifiers at 793nm, and frequency chirped lasers at 793nm.

15. SUBJECT TERMS
Optical Coherent Transients, Spatial-Spectral Holography, Analog Optical Signal Processing, Pulse Shaping, True-Time-Delay, Arbitrary Waveform Generation, Microwave Spectrum Analysis, Optical Scanner, Time-Integrating Correlator.

16. SECURITY CLASSIFICATION OF:			17. LIMITATION OF ABSTRACT	18. NUMBER OF PAGES	19a. NAME OF RESPONSIBLE PERSON Wm. Randall Babbitt
a. REPORT UNCLASSIFIED	**b. ABSTRACT** UNCLASSIFIED	**c. THIS PAGE** UNCLASSIFIED	UL	71	**19b. TELEPHONE NUMBER** (406) 994-6156

Standard Form 298 (Rev. 8-98)
Prescribed by ANSI Std. Z39.18

Final Performance Report

Applications of Optical Coherent Transient Technology to Pulse Shaping, Spectral Filtering, Arbitrary Waveform Generation and RF Beamforming

Grant #
AFOSR/DEPSCOR
F49620-02-1-0275

Period of Reported Performance
6/1/02-5/31/05

Period of Grant
6/1/02-5/31/05

Principal Investigators
PI: Wm. Randall Babbitt   (406) 994-6156
Co-PI: Mingzhen Tian   (406) 994-6286

Address
Physics Department, EPS 264
Montana State University
Bozeman, MT 59717-3840

Other Team Member
Prof. Kelvin Wagner, Univ. of Colorado (CU), (303) 492-4661

Program Manager
Dr. Gernot Pomrenke

Project Summary

Under research conducted by Montana State University and the University of Colorado, several optical coherent transient (OCT) devices was developed and demonstrated, including pulse shaping, arbitrary waveform generation, optical spectral filtering, time integrating correlator, Doppler shifted arrays, and optical beam scanning. OCT's are particularly well suited for RF photonic processing because of their large bandwidths (tens to hundreds of GHz), spectral resolution well below a MHz, and time–bandwidth products (TBP) greater than 10^6. The advancement of OCT technologies is dependent on the development of supporting technologies. Under this grant, several supporting technologies were developed and demonstrated, including high efficiency OCT programming, tapered semi-conductor amplifiers at 793nm, cascaded injection locked amplifiers at 793nm, and frequency chirped lasers at 793nm.

Table of Content

1. Project objectives

Year 1: (06/01/02-05/31/03)

MSU: We will develop a chirped external cavity diode laser (CECDL) to be used as a linear frequency chirp (LFC) source with the ability to chirp over 20GHz within 100 μs, and with an output power ~20mW. We will continue proof-of-concept experiments on OCT pulse shaping and AWG over a narrow band including simulations to examine the performance characteristics to be expected on the broadband. After completion of proof of concepts and simulations, we will use our current 2 GHz CECDL to bring the pulse shaping and AWG to 2GHz bandwidths. Optical filtering using holeburning will be demonstrated initially using our 12 GHz phase modulator and optical filtering using gratings will be demonstrated with the 2GHz CECDL. We will continue our study on linear phase chirps, pushing the programming bandwidth beyond 3GHz and exploring their unique abilities for spatial multiplexing. In collaboration with Prof. Rufus Cone's group, we will develop and characterize the materials needed for processing bandwidths over 20GHz along with the cooperation of Scientific Materials.

CU: Programming Arrays of Time Delays with Photon Echoes We will investigate acousto-optic techniques for controlling and programming arrays of time delays for both scanner applications and the true-time-delay beamsteering functionality of photon echo systems being developed at MSU. Systems capable of producing arrays of frequency shifted spots using counter-propagating chirp techniques will be designed and analyzed.

Year 2: (06/01/03-05/31/04)

MSU: The CECDL will be characterized and used in broadband experiments. We will demonstrate TTD on signals greater than 3GHz with TBP greater than 1000. A broadband detection system based on field correlation will be built and used to detect signals with more than 3GHz bandwidth. The multi element antennas far field radiation pattern and the composition of TTD's for beamforming will be studied through simulation. Main lobe steering and narrow band side lobe nulling will be studied first, then the broadband nulling. The simulation results will be used to design the 2-element beamforming experiment. Upon completion of the CECDL characterization, we will use its multi-GHz abilities to demonstrate the pulse shaping and AWG on a broadband using the field correlation detection system to analyze the waveforms. Optical filtering using gratings will also be demonstrated with the 20GHz CECDL.

CU: Experimental Demonstration of A demonstration experiment will be performed using acousto-optic devices to programmably frequency shift an array of beams by Bragg diffracting from counter-propagating chirp waveforms. This array of signals will be applied to an OCT medium to demonstrate a linear ramp of programmed time-delays, and this technology will be transitioned to Montana State University to enhance and enable their broadband true-time-delay system experiments.

Year 3: (06/01/04-05/31/05)

MSU: We will directly show the removal of jammer signals from various spatial directions and show the subsequent reception and coherent summing of the wanted signal. Pulse shaping, AWG, and optical filtering will be completed upon a broadband with the results of analog waveforms being reapplied to further OCT experiments. These analog signals will also be spectrally filtered using the optical filtering techniques as a final demonstration.

2. Summary of most important results
2.1.Pulse shaping programmed with Temporally Overlapped Chirped Pulses.

In our previous work[1] we demonstrated that two temporally overlapped linear frequency chirps (TOLFCs) could be used to create a spectral grating in an inhomogeneously broadened medium. Similarly, more than one pair of the chirps can program a more complex grating structure. Probing such a grating with a brief pulse or a chirped pulse can generate a series of echoes with different delays. These generated echoes can be used as quasi-delta function pulse that make up a data sequence to compose any arbitrary waveform within the programmed bandwidth by varying the delays, the amplitudes, and the phases of the echoes. The delays, amplitudes, and phases of the echoes can be controlled by the settings of the programming chirps. We have developed two programming and probe schemes shown in Figure 1 a and b, where the programming processes for each data bin (or delayed echo) shares a common chirp called the reference and a specifically designed multi-chirp, called the control, that defines the property of each generated echo.

To avoid the interference between the control chirps, the angled beam configuration is needed where the reference chirp propagates in a different direction from the control chirps as labeled as directions $\vec{k}_+$ and $\vec{k}_-$, respectively, in the figure. The probe propagates in the same direction as the reference and the echoes are generated in the direction of the controls. In order to create an echo sequence with required delays, amplitudes, and phases, certain conditions on the chirp rates and phases of the reference, control, (and the probe in Figure 1b case) must be satisfied in order to rephase the echoes with the same phase. We have derived these conditions for pulse shaping and AWG using TOLFCs. The field of a linear frequency chirped field with uniform amplitude can be written as

$$\varepsilon(t) = Ae^{i[(\omega_0+\omega_s)t+\frac{1}{2}\alpha t^2]+i\varphi} = E_c(t)e^{i\omega_0 t} \tag{1}$$

with $E_c(t) = Ae^{i\omega_s t+i\frac{1}{2}\alpha t^2+i\varphi}$, ω_s is the start frequency, and α is the chirp rate. The Fourier transform gives

$$\tilde{E}_c(\omega) = \int E_c(t)e^{-i\omega t}dt = Ae^{i\varphi}\int e^{i\,\text{sign}(\alpha)[(\frac{1}{2}|\alpha|t^2\pm(\omega_s-\omega)t]}dt \tag{2}$$

where function $\text{sign}(\alpha)$ returns the sign of α, positive chirp rate corresponds to upward frequency-chirped field, while negative chirp rate downward chirped field . The integration gives

$$\tilde{E}_c(\omega) = A'e^{-i\frac{(\omega_s-\omega)^2}{2\alpha}}e^{i\frac{\pi}{4}\text{sign}(\alpha)+i\varphi} \tag{3}$$

with $A' = A\sqrt{\dfrac{2\pi}{|\alpha|}}$. This is an ideal frequency-chirp field, which has uniform amplitude in both temporal and spectral domain. It is a good approximation for the chirped field with time bandwidth product (TBP) $\gg 1$. Even for small TBP chirped field, there is no difference when discussing the chirp rate condition and phase compensation in pulse shaping.
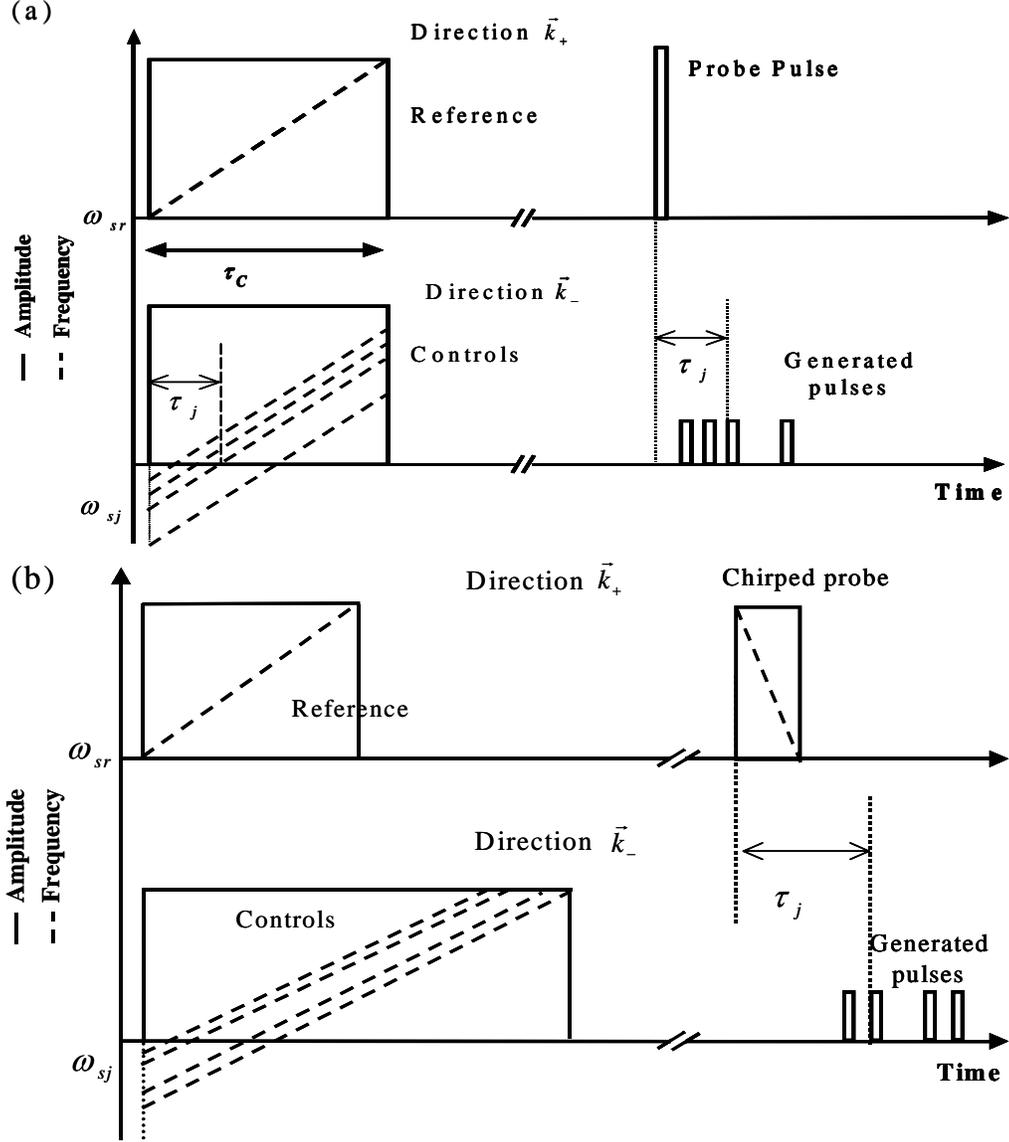
Figure 1. The TOLFC pulse shaping and AWG processes. Multiple frequency-chirped controls with different frequency offset in direction –k are temporally overlapped with chirped reference in direction k. After dephasing, a brief or chirped probe in direction k is diffracted by the spatial spectral grating producing multiple echoes in direction –k with delays corresponding to the frequency offset of controls. (a) The probe is a brief pulse, and (b) the probe is a downward frequency chirped pulse.

The spectral grating generated by two chirped fields (the reference and one control) with time delay and frequency offset is written as

$$\tilde{G}(\omega) = \tilde{E}_r^{*}(\omega)e^{i\omega t_r}\tilde{E}_j(\omega)e^{-i\omega t_j} = A_r' A_j' e^{-i\frac{(\omega_{sj}-\omega)^2}{2\alpha_j}+i\frac{(\omega_{sr}-\omega)^2}{2\alpha_r}} e^{-i\omega\tau_{jr}+i\varphi_j-i\varphi_r+i\frac{\pi}{4}[\text{sign}(\alpha_j)-\text{sign}(\alpha_r)]}$$

(4)

where subscript r is for reference pulse and j is for jth control. Probing this spectral grating with a pulse with spectrum $\tilde{E}_p(\omega)$, the echo's spectrum will be $\tilde{E}_{echo}(\omega) = \tilde{G}(\omega)\tilde{E}_p(\omega)$. In this pulse shaping and AWG technique, the probe can be brief pulse or frequency chirped field.

$$
\tilde{E}_{echo}(\omega) =
\begin{cases}
A'e^{-i\frac{\omega^2}{2}(\frac{1}{\alpha_j}-\frac{1}{\alpha_r})} \; e^{-i\omega(t_p+\tau_{jr}-\frac{\omega_{sj}}{\alpha_j}+\frac{\omega_{sr}}{\alpha_r})} \; e^{-i\frac{\omega_{sj}^2}{2\alpha_j}+i\frac{\omega_{sr}^2}{2\alpha_r}+i\varphi_j-i\varphi_r} \; e^{i\frac{\pi}{4}[\text{sign}(\alpha_j)-\text{sign}(\alpha_r)]} \\
\qquad\qquad\qquad\qquad\qquad\qquad\qquad\qquad \textit{for brief probe} \\[4pt]
A'e^{-i\frac{\omega^2}{2}(\frac{1}{\alpha_p}+\frac{1}{\alpha_j}-\frac{1}{\alpha_r})} \; e^{-i\omega(t_p+\tau_{jr}-\frac{\omega_{sp}}{\alpha_p}-\frac{\omega_{sj}}{\alpha_j}+\frac{\omega_{sr}}{\alpha_r})} \; e^{-i\frac{\omega_{sp}^2}{2\alpha_p}-i\frac{\omega_{sj}^2}{2\alpha_j}+i\frac{\omega_{sr}^2}{2\alpha_r}+i\varphi_p+i\varphi_j-i\varphi_r} \; \times \\
e^{i\frac{\pi}{4}[\text{sign}(\alpha_p)+\text{sign}(\alpha_j)-\text{sign}(\alpha_r)]} \qquad\qquad\qquad \textit{for chirped probe}
\end{cases}
\tag{5}
$$

where $A' = A'_r A'_j A'_p$. For the purpose of pulse shaping, the echo should be rephased at the same instant, which means the phase of the echo should not be a quadratic function of the frequency. This set the rules for the chirp rate as,

$$
\begin{cases}
\alpha_r = \alpha_j & \textit{for brief probe} \\[6pt]
\dfrac{1}{\alpha_p} + \dfrac{1}{\alpha_j} - \dfrac{1}{\alpha_r} = 0 & \textit{for chirped probe}
\end{cases}
\tag{6}
$$

This is the necessary condition for generating a Fourier transform-limited echo using chirped pulses. The second phase term in the above equation determines the time delay of the echo, with a total delay time after the starting time of the probe chirp,

$$
\tau_{dj} =
\begin{cases}
\dfrac{\omega_{sr}-\omega_{sj}}{\alpha_r} & \textit{for brief probe} \\[10pt]
\dfrac{\omega_{sp}}{\alpha_p} - \dfrac{\omega_{sj}}{\alpha_j} + \dfrac{\omega_{sr}}{\alpha_r} & \textit{for chirped probe}
\end{cases}
\tag{7}
$$

For pulse shaping with TOLFCs, we generally have $\text{sign}(\alpha_1) = \text{sign}(\alpha_2)$. The delay can be adjusted by properly choosing the starting frequencies. To get uniform phase echoes, we can set the initial phase for jth control to be,

$$
\varphi_j = \frac{\omega_{sj}^2}{2\alpha_j}
\tag{8}
$$

This phase compensation is not the sole condition to get uniform phase echoes, but this guarantees that the grating has constructive fringe at a preset frequency ω_0 (usually the center frequency of the probe). Therefore, the echo phase only depends on the phase of the probe. This technique allows generating the pulses with phase modulation by simply adding different phases to the controls and the amplitude modulation by setting different control amplitudes.
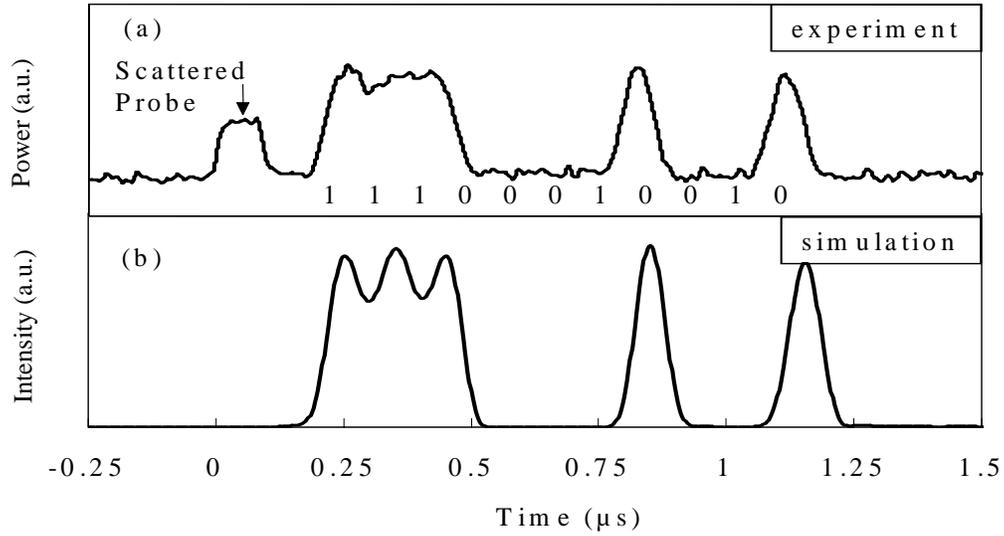
Figure 2. Generated pulses in the pulse shaping process with 20MHz bandwidth TOLFCs and a 100ns brief probe. Output is the 11 bits barker code in binary amplitude modulated format (11100010010). (a) Experimental results and (b) Simulation results.

2.2. Narrow band demonstrations of pulse shaping

Proof-of-concept demonstrations of the TOLFC pulse shaper for the different processes described above were performed. In the initial demonstrations acoustic-optic modulators (AOMs) were used to create the linear frequency chirps with bandwidth up to 20 MHz. Experiments were performed using an external cavity diode laser with an injection locked amplifier lasing at the $^3H_4$-$^3H_6$ transition in Tm^{3+}:YAG (~793 nm). The laser beam was split with a 50/50 beam splitter, passed through two separate AOMs driven by arbitrary waveform generators to create the reference and control chirps. The two beams were then focused to a waist of ~60∓m and overlapped in the crystal. The crystal was cooled to ~4.5 K. Powers before the crystal were ~15mW on each path. The echo output was incident onto a 50 MHz amplified silicon photodetector. The RF waveform used to program the reference chirp was $\sin(2\pi f_1 t + \frac{1}{2}\alpha t^2)$, where f_1 is the start frequency of the chirp. The control chirps were frequency offset copies of the reference chirp.

First we tested the pulse shaper's ability to produce pulse trains with arbitrary times and phases. The goal was to program two complex spectral gratings that produced the 11 bit Barker code (11100010010) in both amplitude (AM) and phase modulated (PM) forms at 10 Mbits/sec. Programming chirps were 5∓s long with 20MHz bandwidth giving a chirp rate of 4MHz/∓s. The frequency offset between individual control chirps needed to produce the 10 MHz bit rate was 400kHz. The bits were controlled via the phase and amplitude of each control chirp. For "1" bits, $A_n =1$. For "0" bits, $A_n =0$ for AM and $A_n = -1$ for PM. A 100ns probe pulse processed by the two different complex gratings produced the expected code in both the binary AM coding (Figure 2a) and the bi-phase (0, ≺) PM coding (Figure 3a). The phase encoding (0,π) is

8

observed as nulls at phase transitions in intensity plots in Figure 3. The exponential homogeneous decay of the output was compensated for by adjusting the relative amplitude of each control chirp, creating uniform bit amplitudes across the echoed data sequence.
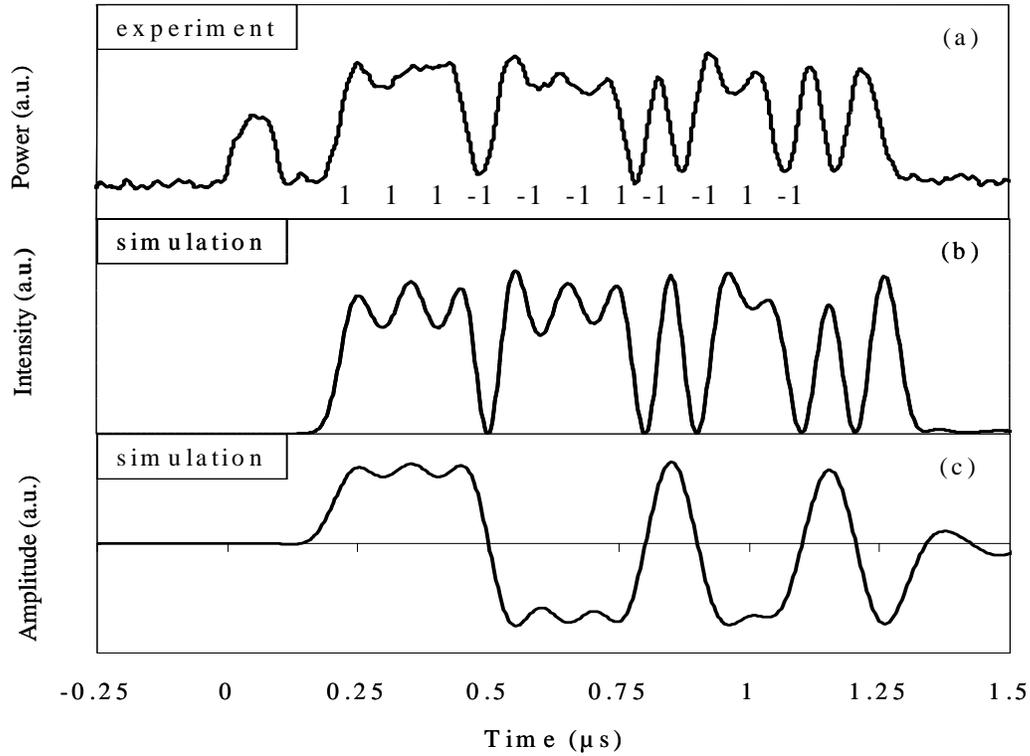
Figure 3. Generated pulses in the pulse shaping process with 20MHz bandwidth TOLFCs and a 100ns brief probe. Output is the 11 bits barker code in binary phase modulated format (+++---+--+-). (a) experimental results, (b) intensity in the simulation, and (c) the field in the simulation.
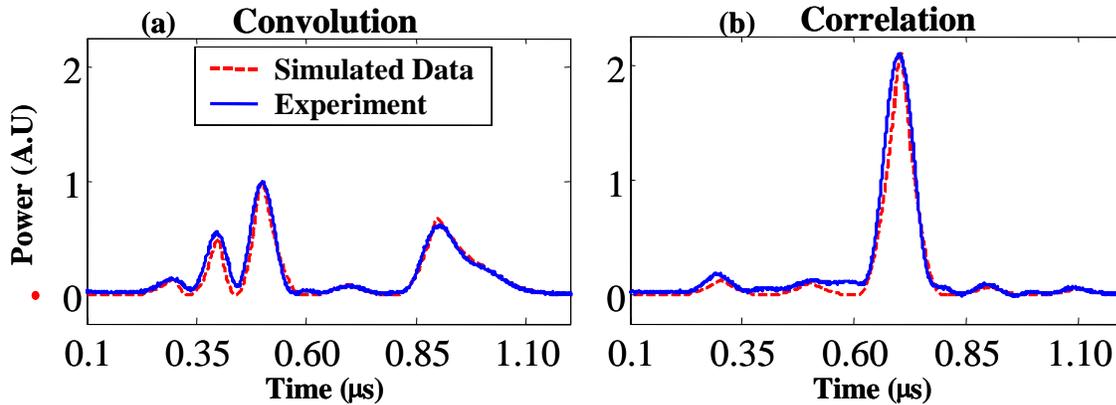
Figure 4. The calculated (dashed curve) and experimental (solid curve) output of the pulse shaper programmed with the (a) time reverse of the bi-phase 5 bit Barker code (1,-1,1,1,1) and (b) the time forward (1,1,1,-1,1). The resultant operations of (a) self-convolution and (b) auto-correlation were performed on the probe pulse (1,-1,1,1,1).

The ability of the pulse shaper to reshape arbitrary probe pulses was tested next. We demonstrated this by programming the bi-phase 5-bit Barker code (1,1,1,-1,1) and the time-reverse (1,-1,1,1,1) versions of the code into the material. We then probed each grating with the code (1,-1,1,1,1). This yielded the operations of self-convolution and auto-correlation of the probe pulse, respectively. This also tested the pulse shaper's phase control. In the first experiment since only the intensity of the output waveform was detected, phase transitions appeared only as nulls in the output. For faithful correlation and convolution, the phase must be well controlled. The theoretical outputs (with decay) are shown in Figure 4 along with the experimental outputs of the pulse shaper. The agreement between the experiment and calculated outputs confirms that good phase control is obtained.
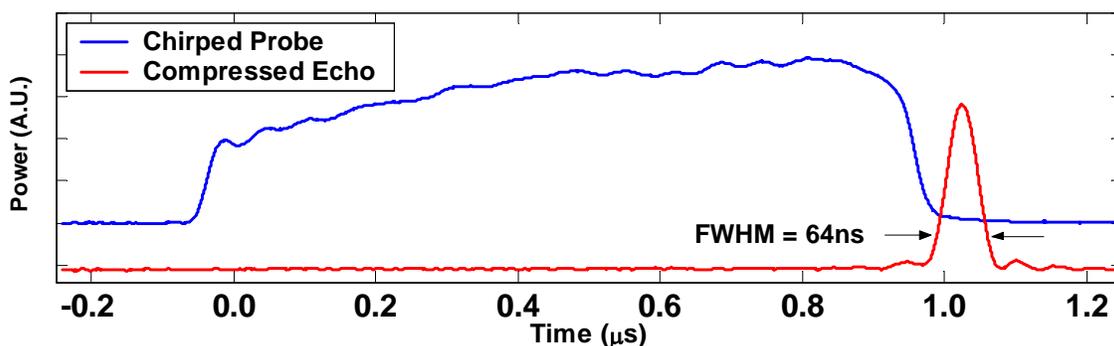

Figure 5. Test of chirped pulse compression. A 1 µs, 20 MHz chirp was diffracted off a chirp compressing grating producing the narrow echo. The full width half max of the echo measured at one quarter the intensity is 64 ns, close to the bandwidth limit. The probe and echo are plotted on different scales.
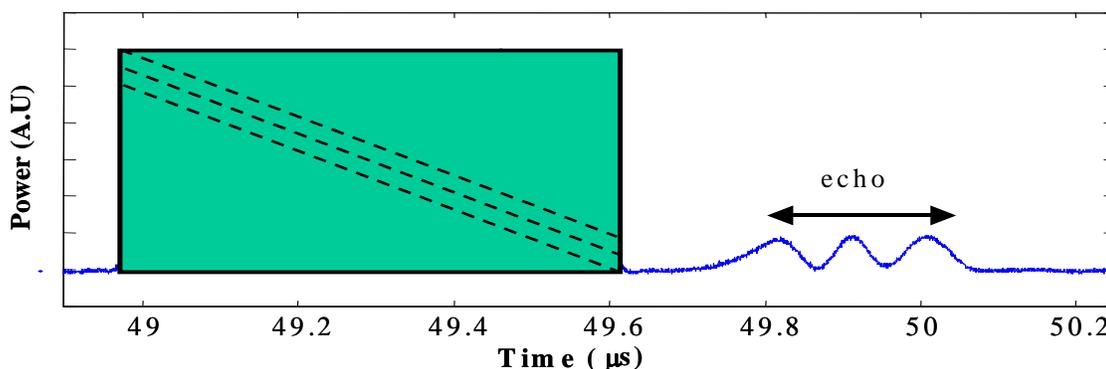
Figure 6. Multi-echo pulses from chirped probe with multiple frequency offsets.

Finally we used this TOLFC pulse shaping method to perform arbitrary waveform generator via linear frequency chirped pulse compression of a 1 µs chirped pulse with a –20 MHz/µs chirp rate. For a 6 µs long 20 MHz up chirped reference pulse, the required chirp rate for the second chirp is 4 MHz/µs. An offset of 0.3 MHz was added to the second chirped pulse giving a ~90 ns delay between the end of the chirped probe and the echo. Figure 5 shows the probe chirp and the compressed echo output. The temporal width of the echo measured at ¼ the intensity was 64 ns. This gives a compression factor of ~16 with compressed echo duration close to the expected

value of 50 ns for a 20 MHz bandwidth limited pulse. To test the multi-pulse generation ability we probed this grating with a 1us 10 MHz chirp with three different frequency offsets as shown in Figure 6. This resulted in three output echoes.

As the chirped bandwidth of the pulses increases, the compression factor should increase. This ability to compress chirps can be combined with the basic multiple-TOLFC process described above. By adding more control chirps to create multiple chirp-compressing gratings with different time delays and choosing the proper delays and phases of these compressed echoes, a multi-GHz chirped probe pulse can produce a multi-GHz analog optical signal with arbitrary shape of nanosecond to microsecond duration. In addition to being able to shape brief pulses into arbitrary waveforms, this versatile OCT pulse shaper can perform pulse shaping on arbitrarily shaped probe signals, including chirps, as well as perform the operations of convolution, correlation, and compression. Unlike previous demonstrations of OCTs, such as true time delay and optical memory, where the output echo mimicked one of the three input pulses, this new programming method produces a unique and well-controlled output signal of arbitrary shape.

2.3. Broadband demonstrations with chirped external cavity diode lasers

Recently developed high bandwidth compact chirped external cavity diode lasers (ECDL) (see picture in Figure 7) should make it possible to control the shape of multi-GHz output signals with only low bandwidth (MHz) electronics and acoustic-optic modulators. We demonstrated this ability using the setup shown in Figure 7 where the chirped ECDL was used as the broadband laser source.
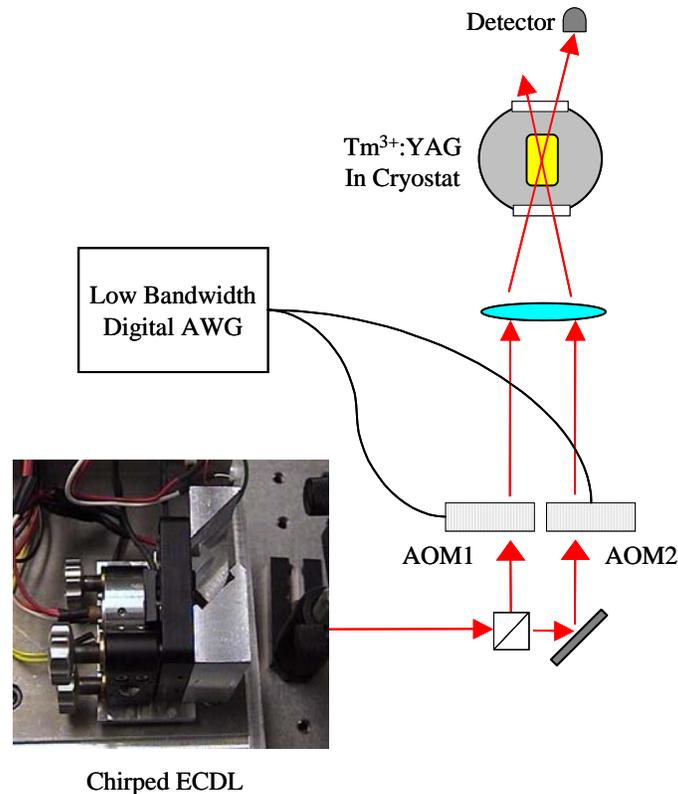
Figure 7. Experiment setup for broadband pulse compression and pulse shaping.

The pulse compression scheme used in Figure 1b was employed. AOM1 and AOM2 in the setup controlled by a low band digital arbitrary waveform generator were synchronized to the frequency chirp from the ECDL to create the reference, control, and the probe pulses.
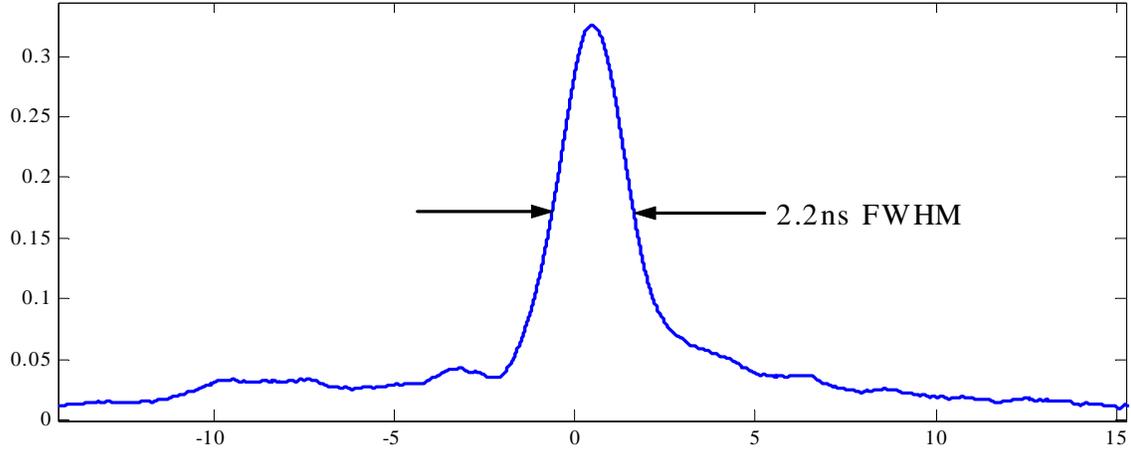
Figure 8. The echo pulse from a 1μs probe pulse chirped over 700MHz. The compression factor is 450.

We first demonstrated single chirped pulse compression. Figure 8 shows a 2.2ns echo pulse from a 1μs–long probe pulse chirped over 700 MHz. This results in a compression ratio of 450. Unfortunately, instabilities in the laser phase or the chirp destroys the compression and makes the width fluctuate and the above captured waveform is not typical.
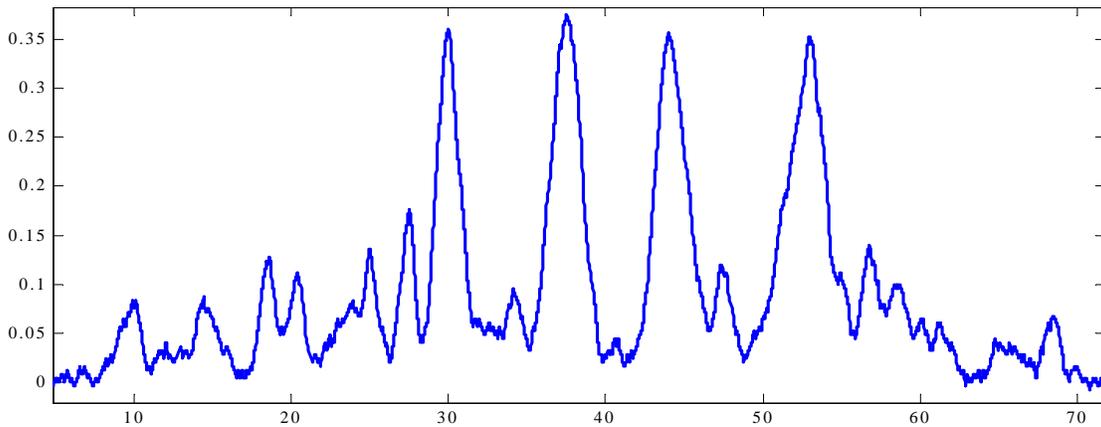
Figure 9. Four echo pulses from a 1GHz chirped probe pulse. The noise is mainly caused by the frequency and phase jitters of the laser source.

We also did a preliminary demonstration of the generation of broadband multi-pulse using the chirp compression scheme. Figure 9 shows four echo pulses have been generated from 1GHz chirped probe. The noise in this process is attributed mainly to the frequency and phase instability of the chirped ECDL and we are continuing to characterize the chirped ECDL to

improve its stability and chirp bandwidth. In addition, we are collaborating with a local company, AdvR on a waveguide chirped ECDL that promises high performance.

2.4. Broadband demonstration with linear frequency side band chirp

The approach to achieving pulse shaping or arbitrary waveform generation discussed here is based upon chirped compression using S2 holography. Here the spatial-spectral interference of two spatially distinct, temporally shaped optical fields, are stored as spatial-spectral gratings within an inhomogeneously broadened transition of a cryogenically cooled rare-earth ion doped crystal. This grating acts as a spectral filter that persists for the population lifetime, T_1 and can be refreshed as conditions and timings change or maintained in a quasi-steady state. A subsequently applied third pulse, causes a radiated electric field that is spectrally filtered by the stored grating in a spatially phase matched output direction.
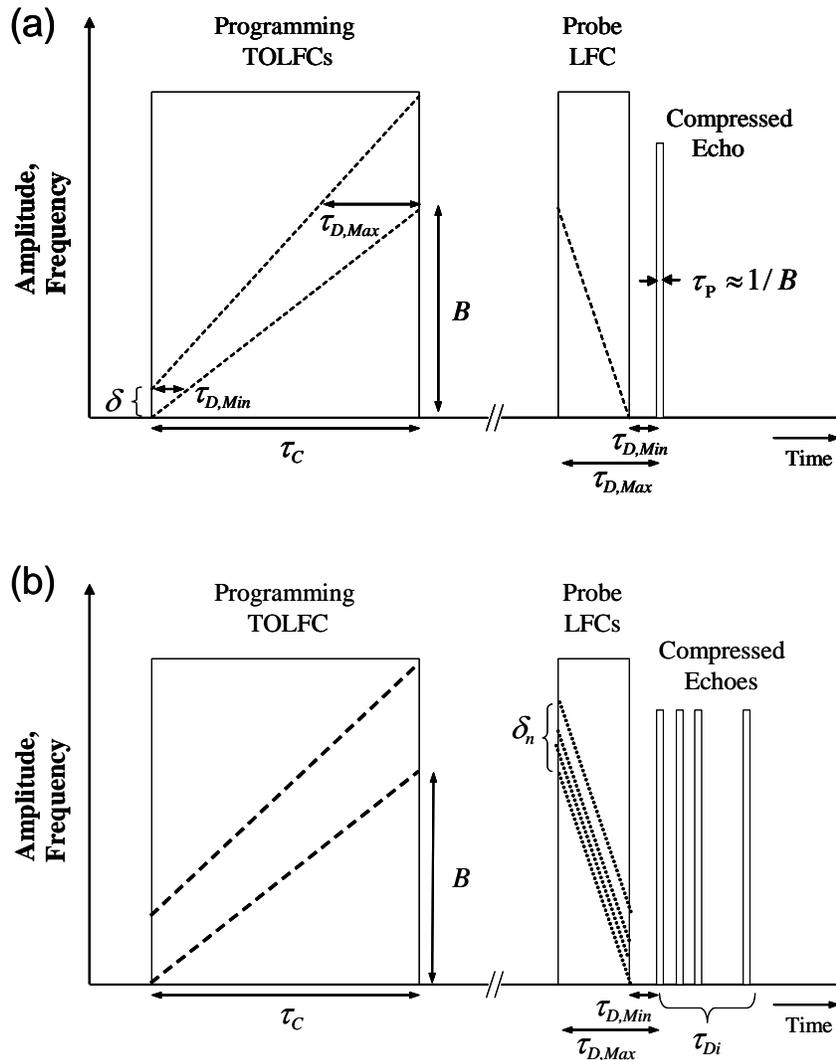
Figure 10 (a) Programming approach for chirp compression. (b) An approach for extending chirped pulse compression to AWG.

13

The temporally overlapping chirped programming approach for pulse compression is shown in Figure 10 (a). The vertical scale shows both optical instantaneous frequency (dashed lines) as well as amplitude (solid lines). Here two temporally overlapping chirped pulses are spatially overlapped within an S2 material. These two pulses interact with the ions to produce a spectral grating whose period is chirped as a function of frequency. At the lower frequencies, just when the two pulses spectrally overlap, the stored grating has an instantaneous period equal to $1/\tau_{D,Min}$. At the last point where the two chirps spectrally overlap, the stored grating has an instantaneous period equal to $1/\tau_{D,Max}$. If this grating is probed by a down chirp with the appropriate chirp rate, all of the diffracted energy will occur at a single point in time as illustrated. The relation between the chirp rates for this type of chirped compression has been found to be

$$\alpha_2 = (\alpha_1\alpha_3)/(\alpha_3 - \alpha_1),$$ (9)

where, α_1 is the chirp rate of the frequency up-shifted programming pulse (referred to as the reference chirp), α_2 is the chirp rate of the frequency downshifted programming pulse (referred to as a control chirp), and α_3 is the chirp rate of the probe pulse. The stored time delay of the grating, τ_d, becomes a function of instantaneous frequency, f, and can be found to be

$$\tau_d(f) = \frac{f}{\alpha_2} - \frac{f}{\alpha_1} + \frac{\delta}{\alpha_1}.$$ (10)

This technique and similar non-temporally overlapping approaches have successfully demonstrated that chirp compression can occur over low bandwidths (~20MHz) and that the temporal duration, τ_P, of the output pulse closely matches the theoretical value of $1/B$. The largest pulse compression factor, a ratio between the probe pulse and the compressed pulse, reported to our knowledge is ~450. Here we increase the bandwidths of the chirps as well as provide a method to utilize the compressed pulse for creation of arbitrary waveforms, thus making the approach more practical.

Microwave AWG
The chirped pulse compression technique can be extended to create arbitrary waveforms in a straightforward and practical manner. By simply adding multiple frequency offset probe chirps, each with their own phase and amplitude control, multiple compressed pulses can be formed on the output. This is shown in Figure 10 (b). If one wishes to create a waveform consisting of N such compressed pulses, then N frequency offset pulses, each with a different offset, δ_n, as well as a compensating phase factor are used. In essence, the arbitrary waveform is created with a set of phase and amplitude controllable delta functions (the compressed pulses).

In this approach, some amount of over sampling is needed. In order to create an arbitrary waveform with a bandwidth of 1 GHz, it is necessary that at least two pulses create this waveform due to the Nyquist sampling theorem. Thus, the compression bandwidth would need to be at least 2 GHz. Typically small frequency offsets (10s of kHz) are needed to create the proper pulse spacings. Thus, low bandwidth electronics can be utilized to control the hig bandwidth arbitrary waveform generation, adding to the practicality of this approach. However, a broadband, linear optical chirp is needed as a source.

Extension to Linear Sideband Chirp Approach

There are essentially three main approaches for creating fast (~MHz/µs) linear frequency chirped optical pulses: (1) using acousto-optic modulators (AOMs) driven with a chirped RF source, (2) using EOPMs driven with a chirped RF source, (3) utilizing a peizo or intracavity electro-optic material to change the cavity length of a laser. Unfortunately, AOMs have low bandwidths (<1GHz) and thus can not provide the broadband chirp necessary to create compressed pulses shorter than a nanosecond. The third approach has shown some promise. Here high bandwidth chirped external cavity diode lasers (CECDLs) have been developed and utilized with chirped programming approaches to create spectral gratings in excess of 2 GHz. Unfortunately, these lasers rely on internal changes to the laser cavity to produce LFCs and thus suffer problems with long term stability as well as chirp linearity. The stability and precision of such lasers has been reported to be ~500 kHz over a 10 ms time scale. Thus to record spectral gratings with features narrower than 500 kHz, which is required for the type of arbitrary waveform generation discussed here, these CECDLs would need complicated chirp stabilization circuits that have yet to be developed. The second approach, when driven with broadband digitized chirping RF signals from a pulse pattern generator and using a stabilized optical source in essence chirps the sidebands created by the electro-optic modulator. This approach, known as the linear sideband chirped (LSC) approach, has shown the ability to create broadband optical chirps and allows the creation of spectral gratings with features < 500kHz.
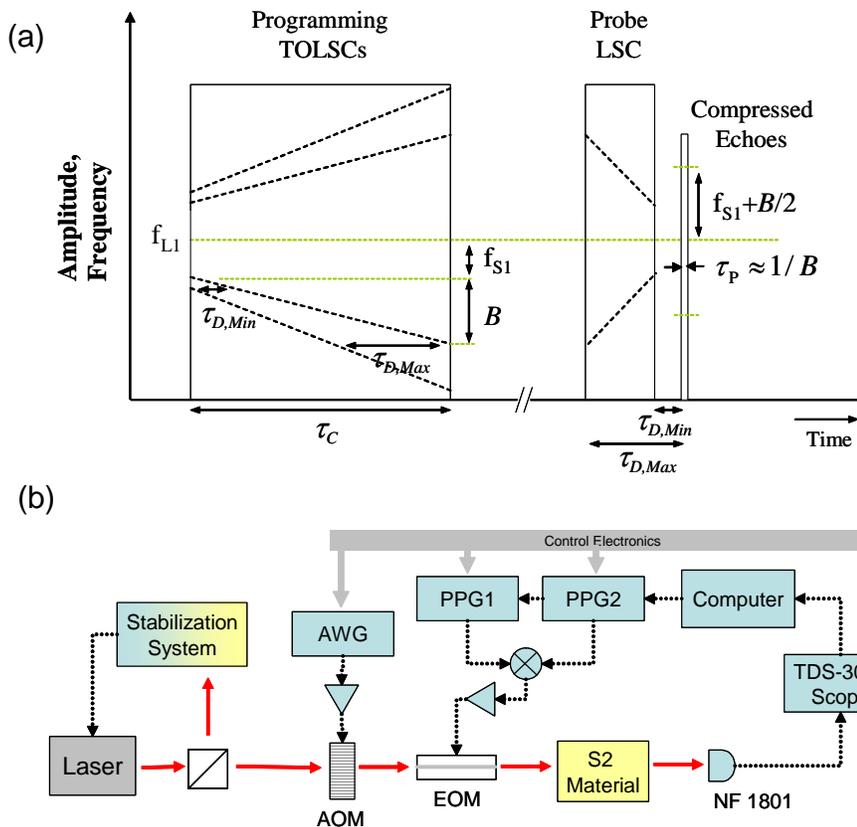
Figure 11. (a) The programming approach using LSCs.
(b) The experimental setup for the demonstrations.

Figure 11 (a) shows how chirped compression can be programmed and probed with LSC pulses. Here we show only the chirping first order sidebands created around a stable optical source with frequency f_{L1}. The control chirp starts with an offset frequency of f_{S1} and chirps over the bandwidth B during the optical pulses duration, τ_C. The reference chirp has a faster chirp rate and has an additional offset frequency, δ. The probe pulse is a down chirp with the appropriate chirp rate and produces two compressed echo pulses, separated in frequency by $\Delta f = 2f_{S1} + B$. Note that these two pulses are temporally overlapped and if observed on a detector would beat at Δf.

The above discussion can be directly applied to the LSC chirped compression approach as well. However, one now has the flexibility to create the frequency offsets with either the EOPM or the AOM. Here we utilize the AOM approach, which essentially breaks the symmetry of how the upper and lower frequency spectral gratings are probed. Essentially, the probe chirps are offset with respect to the central point of symmetry causing the echo output from one grating to be delayed with respect to the output of the other. When multiple probe chirps are used for AWG, the probe chirps will stimulate two pulse trains, one forward in time and one backwards in time around the point of symmetry given by what is known as $\tau_{D,Max}$.
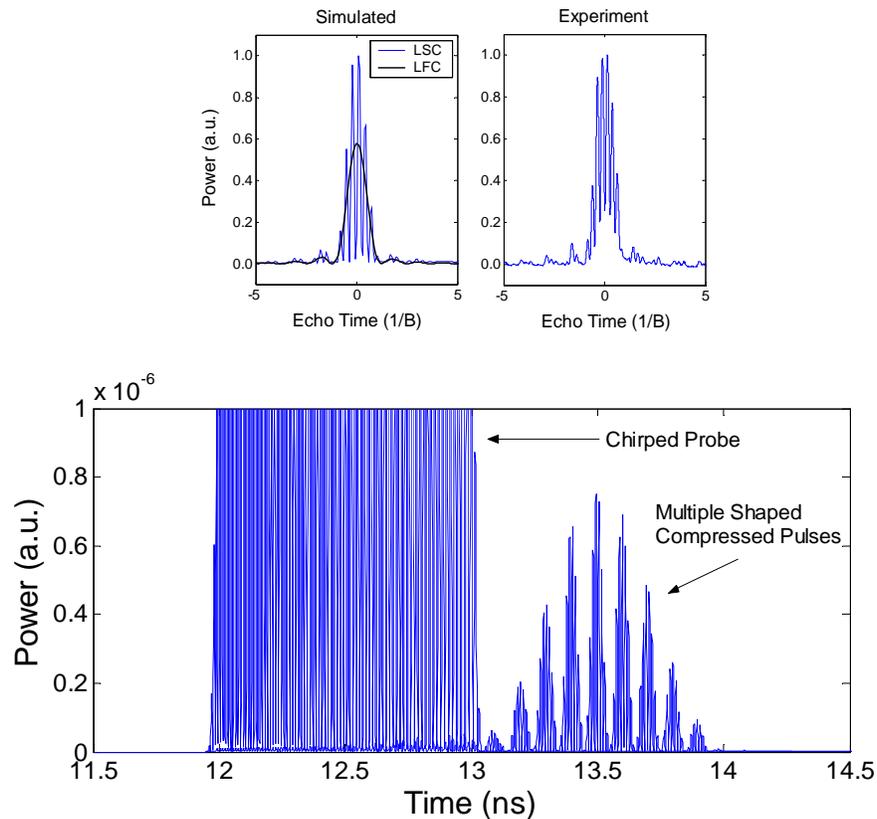
Figure 12. (Top left) Two different simulations of chirp compression. One showing traditional LFC programming (section II-A) and the other showing the LSC approach (section II-C). (Top right) An experimental demonstration of the LSC approach showing the beat between the two echoes. (Bottom) Simulation showing how the LSC approach can be extended to produce arbitrarily shaped pulses as discussed in section II-C. Here half a period of a sine wave is programmed.

16

Simulations of Linear Sideband Chirp Approach
Here we utilized a previously developed Maxwell-Bloch simulator to model the output of the photonic arbitrary waveform generator ((PAWG). Figure 12 (top left) shows the compressed pulse using the traditional LFC approach (no beat) and one using the LSC approach. Here $B = 20$GHz, the duration of the probe pulse was 1 ns, and $\tau_{D,Max} = 2.5$ ns. As expected, the pulse is compressed to $\sim 1/B$, and a beat frequency is observed between the two temporally overlapping frequency offset echo fields.

Simulations were also performed to demonstrate the capability of the material to perform AWG. Here we shaped the compressed output pulses into a series of pulses with different amplitudes to represent half a period of a sine wave. Figure 12 (bottom) shows the simulated chirped probe pulse and the train of shaped compressed pulses. Here the spacing between the pulses was greater than the width of the pulses, however, this is not necessary and simulations have shown good reproducibility of the desired waveform even when the compressed pulse width is equal to the spacing between them.

Experimental Setup
The experimental setup used is as shown in Figure 11 (b). The master optical oscillator was a frequency stabilized Ti:Sapphire laser, locked to a regenerative spectral hole frequency reference. Two pulse pattern generators (PPGs) were used to generate digital binary codes that were subsequently summed, amplified and fed to an EOPM. The PPGs were each programmed with an individual digital chirp representing one of the programming pulses and one PPG was additionally programmed with a probe chirp. Here the duration of the programming and probe were 500 μs and 4 μs respectively. The probe chirp was additionally modulated with frequency offsets from an AOM to create shaped compressed pulse trains. The modulated optical output of the EOPM (~1 mW) was amplified by injection locking of a high power diode laser and further amplified to ~300 mW with a semiconductor optical amplifier. This light was made to irradiate a volume of a Tm:YAG sample held at 4K (~100 μm diameter measured at 1/e points over the sample length). The compressed echo pulses were detected with an avalanche photodiode with ~1 GHz of bandwidth.

Low Bandwidth Field Verifications
To verify the predictions of the simulator, we first conducted a low bandwidth demonstration, where the beat note between the two temporally overlapped, frequency offset echoes could be observed. As can be seen, in Figure 12 (Top right) the compressed echo output does have a beat note as expected. The duration of the pulse also closely matched the expected $1/B$. Here $B = 100$ MHz and $f_{s1} = 150$ MHz.

High Bandwidth Chirped Compression, AWG, and pulse shaping
We also demonstrated the systems performance at higher bandwidths and its ability to produce shaped pulse trains. Figure 13 shows the 4 μs probe pulse and the compressed echo output for a $B = 1.25$ GHz, $f_{s1} = 1.3$ GHz and $\tau_{D,Max} = 7$ μs. The inset plot shows a zoom of the compressed echo, here with a measured FWHM of 0.90 ns, closely matching the expected 0.8 ns width. This is a compression factor of ~4440, to our knowledge the largest reported to date. The beat note is not visible due to detector bandwidth limits.
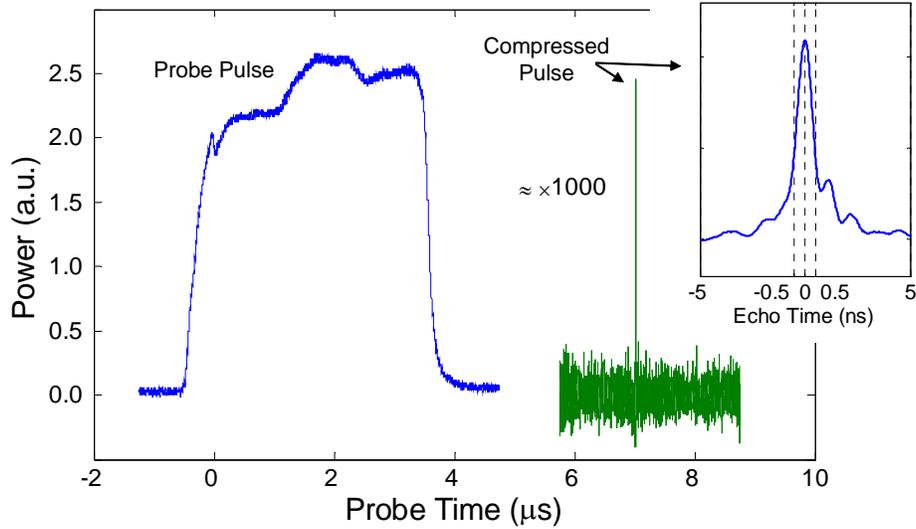
Figure 13. (Left) Experimental 4.00 μs probe chirp and compressed echo pulse. (Right) A zoom of the compressed pulse with a FWHM of 0.90 ns giving a measured compression factor of 4440. Gridlines are shown at 0.5 ns.

Figure 14 shows an experimental demonstration for pulse shaping a series of compressed pulses. Here we demonstrate that the pulse train can be shaped and the pulse's time delays controlled using low bandwidth frequency offsets. Typically the offset frequency to create pulses was around ~0.5 MHz and were created with an AOM. Thus, the pulse train theoretically should be symmetric around the central peak. In this demonstration, we attempted to create a half period of a sine wave similar to that simulated and shown in Figure 12. The left plot of Figure 14 shows the output pulse trains for $B = 500$ MHz with a pulse spacing of ~8 ns. The middle plot shows the result for $B = 500$ MHz with ~4 ns spacing and the right plot shows results for $B = 1$ GHz with ~4ns spacing. The slight non-symmetry in the outputs is likely due to the detector returning from saturation. These outputs represent the first step towards the demonstration of a PAWG based upon chirp compression in S2 materials.
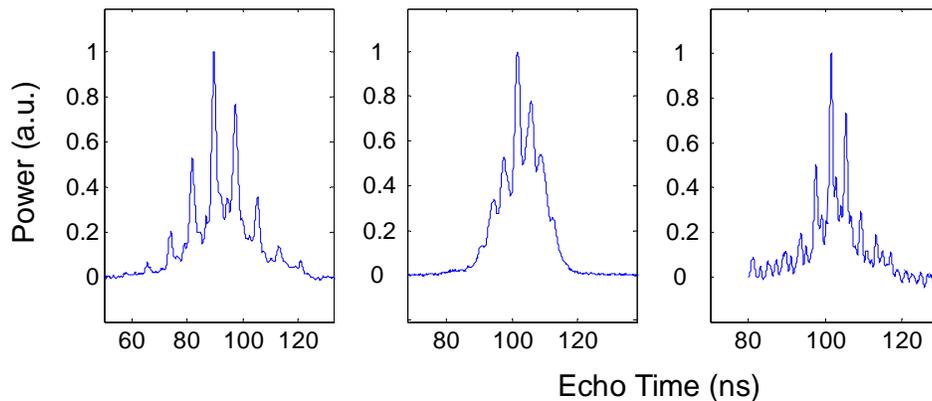
Figure 14. An experimental demonstration showing a series of shaped compressed pulses. (Left) 500 MHz bandwidths with spacing between pulses of ~8 ns. (Middle) 500 MHz bandwidths with ~4 ns spacing. (Right) 1 GHz bandwidths with ~4ns spacing.

2.5. Multi-GHz arbitrary waveform generation

The Double SideBand (DSB) PAWG approach is pictured in Figure 15 and is similar to the single-sideband (SSB) PAWG approach described in the earlier section. The key difference is that the DSB PAWG technique creates two spectral gratings, one above the laser frequency, f_{L1}, and one below it, each offset from f_{L1} by an amount f_{S1}. The frequency offsets of the probe pulse were still created using an AOM. Since the AOM shifts both sidebands of the probe in the same direction, the symmetry about the laser frequency is broken. This results in two arbitrary waveform being created: One is time forward at the upper frequency and one is time reverse at the lower frequency.
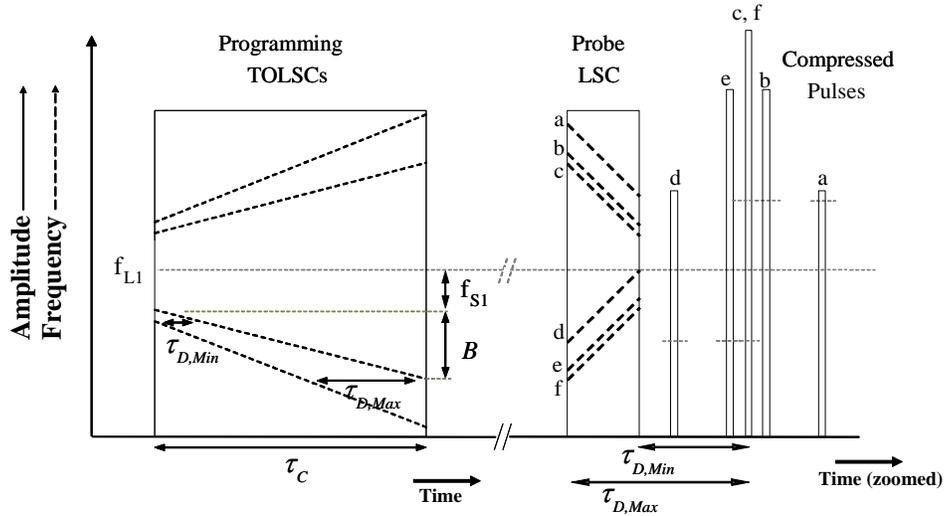
Figure 15 Timing Diagrams for double sideband (BSB) PAWG

The TOLFCs are amplified and sent to an electro-optic phase modulator (EOPM) which mixes them onto a narrow band optical source (793 nm laser light) producing TOLFC sidebands around the laser frequency. The experimental setup used to create (realize) the waveform schematic in Figure 15 is shown in Figure 16.

Figure 17 shows typical PAWG data. Figure 17.a is a chirp pulse compression results with DSB technique, with x1500 compression. Figure 17.b shows thecompressed pulse with a bandwidth of 4 GHz that had a full-width half-maximum (FWHM) duration of 260 ps, (in good agreement with the 1/B expected duration of 250 ps). The 4 GHz probe pulse, that was compressed by the filter to form this 260 ps compressed pulse, had a duration of 4 μs. This gives the filter a compresson factor of >1500, the best chriped compression produced to our knowledge. Figure 17.c shows fifteen compressed echo pulses whose peak power and phase were adjusted to create a single period of a sine wave. These compressed echoes are each 0.8 ns in duration and are spaced at 3.2 ns.

In order to practically implement PAWG in the millimeter-wave regime, future work will focus on utilizing next generation S2 materials that have ~300 GHz absorption features and on developing highly linear broadband chirping laser sources, like a chirped external cavity diode laser. This will enable the creation of ~3 ps compressed echo pulses, allowing the arbitrary generation of >100 GHz waveforms, which would exceed current electronic capabilities by about two orders of magnitude.
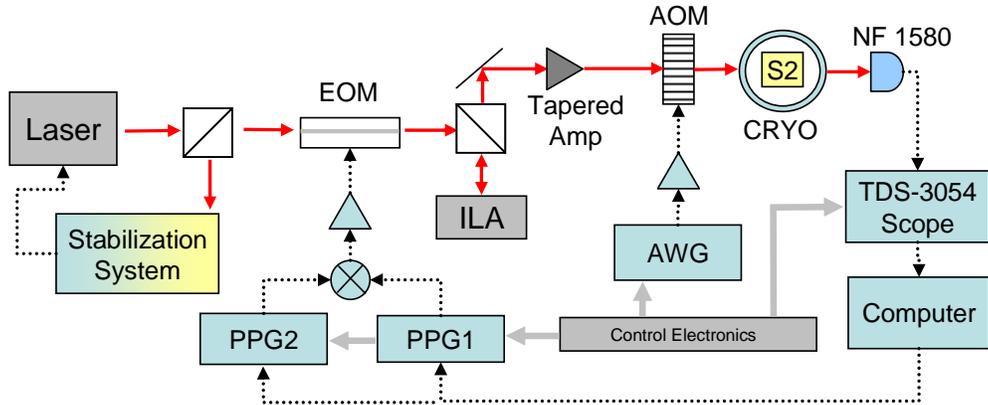
Figure 16. Experimental set-up for DSB PAWG. EOM is the electro-optic phase modulator, which is driven by two pulse pattern generators (PPG). An injection locked amplifier (ILA) is use to boost the output of the EOM to a level acceptable for the tapered amplifier. The acousto-optic modulator (AOM) driven by a low bandwidth arbitrary waveform generator (AWG) creates the multiple sidebands. The cryostat (CRYO) holds the S2 material at 4K. A New Focus detector (NF1580) is used to detect the generated waveforms and capture them on a Tektronix TDS-3054 oscilloscope.
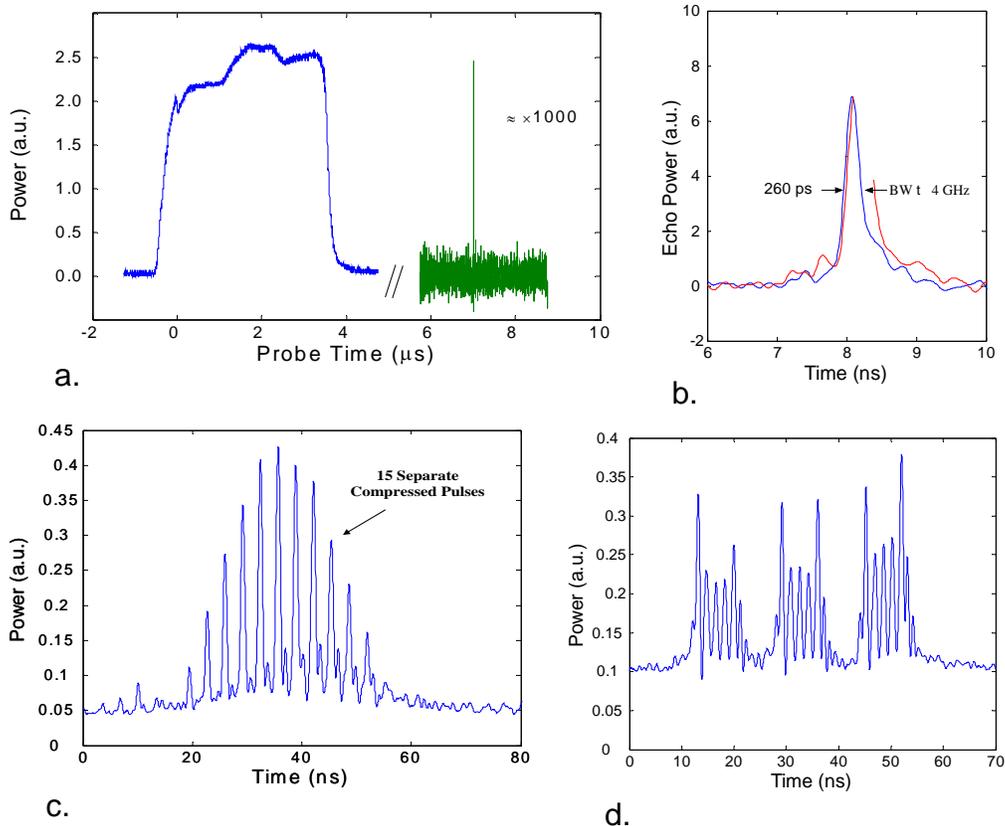
Figure 17 Experimental Data. Part (a.) a typical probe pulse and compressed pulse on the same time scale. Part (d.) a typical compressed pulse. Part (c.) fifteen compressed pulses added together to create a single period of a sine wave. Part (d.) fifteen compressed pulses added together to create three periods of a square wave.

2.6. Spectral filtering

Non-permanent spectral holeburning, such as in rare-earth-doped crystals, allows dynamic optical filtering of signals. This can be used to in radar signal processing to remove jammer or spurious signals. An unprogrammed absorptive inhomogeneously broadened medium with high optical density acts to block any signal transmission over a broad absorption band, on the order of 10-100 GHz range. Such medium can be programmed through spectral hole burning to select certain spectral windows that allow wanted signals to be transmitted with well-controlled transmittances. The center frequency, the shape, and the transmission level of a spectral window are usually programmed by a frequency chirped pulse with modified temporal shape, chirp rate, and optical power. The maximum extinction ratio of the unwanted signal is by the medium's original optical density. The related levels of the wanted signals can be regulated by the programmed transmittances of the spectral windows.

In collaboration with members of Spectrum Lab, we have investigated the method of programming spectral windows using various types of frequency chirped pulses, including:
   1) linear chirp with squared envelope,
   2) linear chirp with squared envelope apodized with Gaussian or cosine function on both ends,
   3) linear-square chirp with ends that have hyperbolic secant envelopes and hyperbolic tangent frequency ramps.
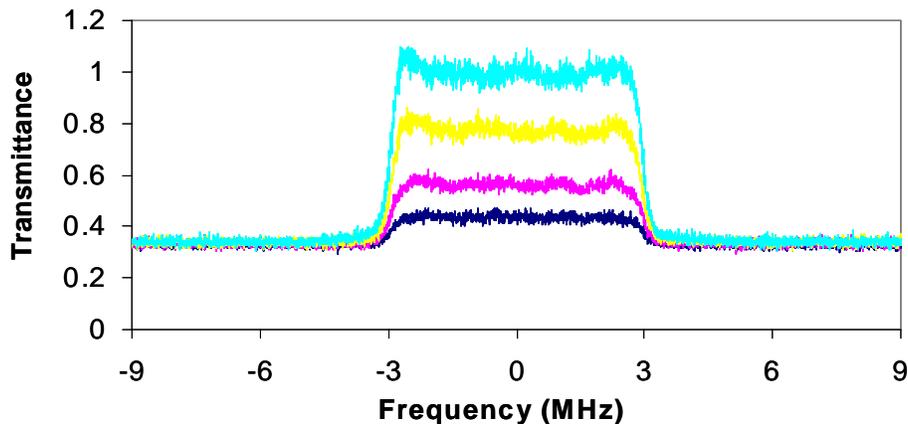
Figure 18. Transmission spectral window programmed by a hyperbolic chirped pulse with different optical powers and probed by a weak linear frequency chirped pulse.

We concluded that the chirp type number 3 produced spectral windows with well defined sharp edges usually on the order of 100 MHz and uniform transmissions within and outside the window. Figure 18 is an example of experimental results where a 6MHz –wide spectral window was programmed with a hyperbolic chirp in a medium of an initial optical density of 0.47 (corresponding to absorption length of 1.1 and transmittance of 0.33). Figure 18 plots various transmittances as function of the frequency, which is programmed by different optical power. The transmittances were measured using a probe pulse with frequency linearly chirped over 18MHz including the programmed window. The plot shows the transmission in the spectral window can be set to a value between the minimum, 0.33, and the maximum, 1 while the transmission stays at the minimum level throughout the non-programmed spectrum.

2.7. Simulator development and simulations

To model OCT processes the coupled Maxwell-Bloch equations have been used successfully for the collinear configuration in thick media.[2] In this theory the coherent effects of light on the inhomogeneously broadened absorbers are described by Bloch equations, where the electric field acts as a driving source to the atomic dipoles. The propagation effects are governed by Maxwell's equations, where the macroscopic polarization caused by the atomic dipole moments acts as a source to the electric field. This simple model, however cannot handle the OCT processes with more complex configurations, such as, frequency chirp, phase modulation, and angled beam, which are required for the pulse shaping and the arbitrary waveform generation. We have developed a theoretical model that includes these complex features and the numerical simulators based on this model. The work was supported by this grant and our DARPA grant.

Figure 19 shows the spatial configuration and the timing of the input pulse sequence of the OCT process of the angled beams. The vectors of the two angled beams defined as $\vec{k}_- = \vec{k}_z - \vec{k}_x$ and $\vec{k}_+ = \vec{k}_z + \vec{k}_x$, respectively, where $\vec{k}_z$ is the wave vector component in propagation direction and $\vec{k}_x$ is the component in the transverse direction x. Since the small angle assumption, we have $\vec{k}_x << \vec{k}_z$ and $\vec{k}_z \approx \vec{k}$. The electric field of the any beam is
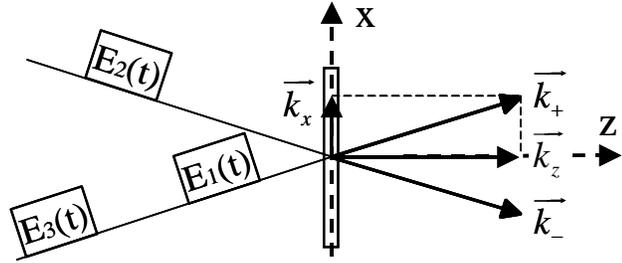
Figure 19. The angled-beam scheme for OCT processes with two beams in direction $\vec{k}_+$, and $\vec{k}_-$, respectively.

$$E(x,z,t) = \frac{\hbar}{\mu}\Big[\Omega_C(x,z,t)\cos(\omega_0 t - k_z z) + \Omega_S(x,z,t)\sin(\omega_0 t - k_z z)\Big] \quad (11)$$

where

$$\Omega_C(x,z,t) = \Omega^{(\vec{k}_+)}(z,t)\cos\Big[\varphi^{(\vec{k}_+)}(t) + k_x x\Big] + \Omega^{(\vec{k}_-)}(z,t)\cos\Big[\varphi^{(\vec{k}_-)}(t) - k_x x\Big] \quad (12)$$

$$\Omega_S(x,z,t) = -\Omega^{(\vec{k}_+)}(z,t)\sin\Big[\varphi^{(\vec{k}_+)}(t) + k_x x\Big] - \Omega^{(\vec{k}_-)}(z,t)\sin\Big[\varphi^{(\vec{k}_-)}(t) - k_x x\Big] \quad (13)$$

are in-phase and in-quadrature field components, respectively, ω_0 is an arbitrary stationary frequency, $\varphi^{(\vec{k})}(t)$ is the general phase term that includes phase and frequency modulations of the field in that direction. The interaction between the field and the atoms is described by coupled Maxwell-Bloch equations,

$$\frac{\partial r_1(x,z,t,\Delta)}{\partial t} = \Delta r_2(x,z,t,\Delta) - r_3(x,z,t,\Delta)\Omega_S(x,z,t) - \frac{r_1(x,z,t,\Delta)}{T_2} \quad (14)$$

$$\frac{\partial r_2(x,z,t,\Delta)}{\partial t} = -\Delta r_1(x,z,t,\Delta) + r_3(x,z,t,\Delta)\Omega_C(x,z,t) - \frac{r_2(x,z,t,\Delta)}{T_2} \quad (15)$$

$$\frac{\partial r_3(x,z,t,\Delta)}{\partial t} = -r_2(x,z,t,\Delta)\Omega_C(x,z,t) - r_1(x,z,t,\Delta)\Omega_S(x,z,t) - \frac{1 + r_3(x,z,t,\Delta)}{T_1} \quad (16)$$

where $r_1(x,z,t,\Delta)$ and $r_2(x,z,t,\Delta)$ are the in-phase and in-quadrature components of the atoms' polarization, $r_3(x,z,t,\Delta)$ is the population inversion, T_2 is the homogeneous decay time. T_1 is the lifetime of the excited state. $\Delta = \omega - \omega_0$ is the detuning of atoms' resonance ω from the laser frequency ω_0. After similar calculation of the polarization obtained from Bloch equations in reference and using retarded time $t' = t - \dfrac{z}{c}$, the propagation equation of the in-phase and out-of-phase components of field are written as

$$\frac{d\Omega_C(x,z,t')}{dz} = \frac{\alpha}{2\pi}\int_{-\infty}^{\infty} r_2(x,z,t',\Delta)g(\Delta)d\Delta \tag{17}$$

$$\frac{d\Omega_S(x,z,t')}{dz} = -\frac{\alpha}{2\pi}\int_{-\infty}^{\infty} r_1(x,z,t',\Delta)g(\Delta)d\Delta \tag{18}$$

where the parameter α is the absorption coefficient. An optically thick medium can be sliced into thin layers and Maxwell-Bloch equations are applied to each layer successively from the input side to the output side of the medium. The output field from a layer is applied as the inputs to the next layer. The spatial Fourier transform is applied only for the output field of the last layer to get the propagation of each beam. However, due to the arbitrary phase modulation, the transmitted in-phase and in-quadrature field along any direction are obtained.

$$\Omega_C^{(\vec{k}_\pm)}(z_f,t') = \frac{1}{2\pi}\int_0^{2\pi}\left[\Omega_C(x,z_f,t')\cos(k_x x) \mp \Omega_S(x,z_f,t')\sin(k_x x)\right] \tag{19}$$

$$\Omega_S^{(\vec{k}_\pm)}(z_f,t') = \frac{1}{2\pi}\int_0^{2\pi}\left[\pm\Omega_C(x,z_f,t')\sin(k_x x) + \Omega_S(x,z_f,t')\cos(k_x x)\right]d(k_x x) \tag{20}$$

where $\Omega_C^{(\vec{k}_\pm)}(z,t') = \Omega^{(\vec{k}_\pm)}(z,t')\cos[\varphi^{(\vec{k}_\pm)}(t')]$, $\Omega_S^{(\vec{k}_\pm)}(z,t') = -\Omega^{(\vec{k}_\pm)}(z,t')\sin[\varphi^{(\vec{k}_\pm)}(t')]$, and z_f is the last layer of the medium. From the transmission of the in-phase and in-quadrature field components, the output field of any direction is obtained as

$$E^{(\vec{k}_\pm)}(z_f,t') = \frac{\hbar}{\mu}\left[\Omega_C^{(\vec{k}_\pm)}(z_f,t')\cos(\omega_0 t' - k_z z_f) + \Omega_S^{(\vec{k}_\pm)}(z_f,t')\sin(\omega_0 t' - k_z z_f)\right] \tag{21}$$

Notice that the field is calculated by combining the in-phase and in-quadrature field components, instead of calculation for the field amplitude and phase. The phase modulation in this model is arbitrary that allows the field with static phase, frequency chirped field, frequency detuned field, and phase noise and frequency jitter of the laser source.

Using the numerical tool developed from the theoretical model, we simulated two pulse shaping methods as previously shown in Figure 1. Figure 2 shows the comparison of the simulations (b) and experimental results (a) for pulse shaping with TOLFCs and brief probe. In both experiments and simulations, the reference and controls are TOLFCs with 20MHz bandwidth and 5µs chirp Time. The reference is in direction +k and the controls are in direction –k with relative frequency offset 0.4*j MHz for jth control. The TOLFCs are phase compensated for generating pulses with uniform phase. In the simulations, the probe is a 100 ns width brief pulse in direction +k. The 11 bits Barker code (11100010010) is produced in amplitude modulated (AM). Figure 3b and c

show the simulation results for the 11 Barker code in phase modulated (PM) form generated under the same condition as the experiment (Figure 3a). The pulse width and shape depend on the bandwidth of the spectral grating generated by TOLFCs and the spectral of the brief probe. The bandwidth of the spectral grating created by the reference pulse and each control pulse depends on the overlapping of the spectra of the two pulses. When generating a long pulse sequence, the controls should have larger bandwidth (compared to the probe) to compensate the frequency offset so that each spectral grating has the same bandwidth.
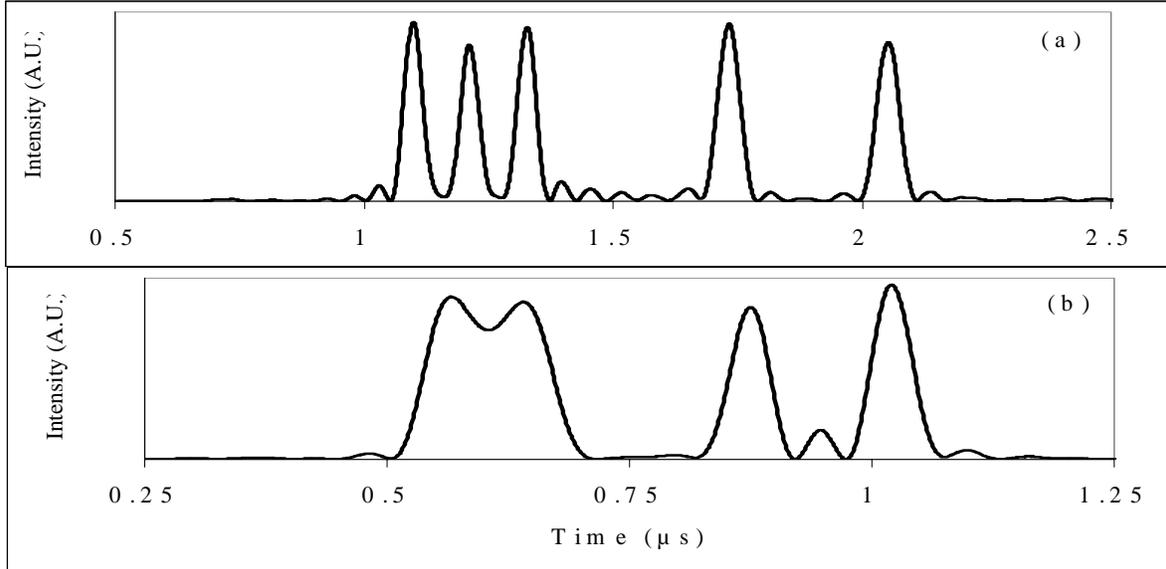
Figure 20. Simulations for the pulse shaping process with 20MHz bandwidth TOLFCs and a 20MHz bandwidth chirped probe. Output is the 11 bits barker code in binary amplitude modulated format (11100010010). (a) Return-to-zero code produced with larger frequency offsets of controls. (b) Non-return-to-zero code produced with smaller frequency offset of the controls.

Figure 20 gives the simulations for pulse shaping and AWG pulse compression using chirped probe. In this case the rephrasing condition for the chirp rates is different from the brief probe as shown in expression (6). We simulated a case where the reference is an upward frequency chirped pulse with 20 MHz bandwidth and 6μs chirp time, controls are upward TOLFCs with 20 MHz bandwidth and 7μs chirp time, and the probe is a downward frequency chirped pulse with 20 MHz bandwidth and 1μs chirp time. The echo widths depend on the bandwidth of the chirped pulses and the delays depend on the frequency offset. This technique allows generating the pulses in the form of return-to-zero (RZ) or non-return-to-zero (NRZ) code by adjusting the echoes' widths and delays. 20MHz bandwidth of both spectral grating and the probe pulse gives the echo width of 0.05μs. Figure 20 (a) shows the simulation for generating 11 bits barker code in RZ form. The frequency offset for jth control is 0.3*j MHz, that corresponds to a 0.105μs separation of adjacent pulses. The NRZ 11 bits barker code generation is shown in Figure 20 (b). The frequency offset for jth control is 0.15*j MHz that gives 0.0525μs pulse separation. This RZ/NRZ method is also applicable to pulse shaping with TOLFCs and brief probe by similarly adjusting the spectral bandwidth and delay time.

2.8. High efficiency programming using linear frequency chirped laser pulses

The experimental and theoretical investigation of the efficiency of programming has led to a more detailed study of the trade-offs between efficiency and uniformity of the output signal, which has further led to new techniques for shaping the linear frequency chirped laser pulses to minimize non-uniformity while achieving high efficiencies. Extensive simulations of these techniques have been carried out. Verification experiments of these techniques have been designed and extensive experimental data is being taken with the benefit of a well designed computerized data acquisition system. A preliminary set of data has been obtained and the data processing is under way. The results provide us with an understanding of the trade-offs between efficiency and uniformity.

The preferred method for programming an OCT material to perform TTD and AWG involves temporally overlapped linear frequency chirps (TOLFCs), where two pulses with linear frequency modulation are overlapped in time. For TTD, the overlapped pulses chirp at the same rate, but with a frequency offset Δ between them. For AWG, the chirp rates may differ and multiple offset frequencies may be introduced. For simplicity, we will focus on the simpler TTD case. If the frequency offset between the programming pulses is small compared to the overall bandwidth of the chirp, then the frequency offset is equivalent to a time delay $\tau_D = \Delta/\kappa$ between the pulses, where κ is the chirp rate. When the overlapped programming pulses illuminate the OCT material, ions at a given frequency within the bandwidth of the overlapped chirps will thus be excited sequentially by the two pulses, with time delay τ_D between excitations. The delay causes a phase shift between the pulses in the frequency domain, which results in the frequency-dependent population redistribution of ions, such that a spectral population grating is created in the crystal with grating period $1/\tau_D$. This spectral grating introduces a delay τ_D on all frequency components of an additional input pulse over the bandwidth of the grating. Broadband TTD is critical to the performance of arrayed radar antenna systems. If this spectrally stored information is probed by a single brief pulse, a time-delayed photon echo is produced that is in essence the impulse response of the stored population grating. Applications such as those listed above employ one or more such gratings to create a tailored impulse response, resulting in a complex sequence of multiple echoes when probed by a brief pulse. The performance of TTD and AWG devices depends on these echoes having both high efficiency and uniform efficiency over a broad range of programmed time delays.

We have shown that the efficiency and uniformity of the photon echoes have strong dependence on the programming pulse strength and envelope shape. The effects of these parameters are investigated first through simulation in the Fourier transform approximation, where both saturation and propagation effects in the material are ignored. In this case the echoes are dependent only on the spectral interference of the programming pulses, independent of pulse strength. Results of Bloch simulations, which also ignore propagation effects but do take material saturation into account, are also presented. To explore the effects of material saturation on echo efficiency and uniformity, numerical simulation based on the Maxwell-Bloch equations, which include the effects of propagation of both the input and output pulses in an optically thick medium, are briefly discussed. Finally, experimental results for an optically thick crystal that show the dependence of efficiency and uniformity on material saturation and propagation are presented.

Theoretical Model for Fourier Transform Approximation
The simplest approach to analyzing OCT processes is known as the Fourier transform approximation. This method is valid only for weak input pulses (the crystal responds linearly to the pulses) and optically thin media (absorption and propagation effects are ignored). In this approximation the OCT crystal is assumed to respond linearly to the power spectrum of the combined programming pulses, $E_1(t)$ and $E_2(t)$. The spectral grating in the crystal is proportional to $E_1^*(\omega)E_2(\omega)$, where $E_i(\omega)$ is the Fourier transform of $E_i(t)$. The grating then acts as a complex spectral filter that processes further inputs, $E_3(t)$, as required by the application. In AWG, for example, several chirped programming pulses ($E_1(t)$ and $E_2(t)$) may be used to program echoes with various amplitudes and time delays, all of which are recalled by a single probe pulse ($E_3(t)$) to produce a high-bandwidth arbitrary waveform. In TTD, after programming ($E_1(t)$ and $E_2(t)$), the subsequent input ($E_3(t)$) is typically an unknown RF waveform on an optical carrier, which is delayed by the OCT device. Independent of the application, the causal output of the programmed filter is given in the frequency domain as

$$E_{echo}(\omega) \propto E_1^*(\omega)E_2(\omega)E_3(\omega). \tag{22}$$

For TOLFC programming, pulses 1 and 2 are the overlapped chirped programming pulses, which are frequency offset with respect to one another. Pulse 3 is a modulated waveform on an optical carrier at the center frequency of the chirped pulses. Because the Fourier transform approximation does not take into account the nonlinear saturation effects that determine the echo efficiency in an actual OCT process, absolute echo efficiencies are not calculated using this method. Echo fluctuation can be examined using this method, however, as long as it is normalized to be independent of overall echo efficiency.

Programming Pulses
Echo fluctuations in the Fourier transform approximation have been investigated for two types of TOLFC envelopes, both of which are shown in Figure 21. Both pulses have rounded edges, which are formed from half periods of cosine waves that smoothly roll from a center (constant amplitude) section of the pulse to zero amplitude on either side. The chirp bandwidth is $B_C = 15$ MHz, which is limited by the bandwidth of the acousto-optic modulator (AOM) used in experiment to modulate the frequencies of the pulses. Because the range over which a laser beam can be tuned is typically the limiting factor in practice, the bandwidth defined here is the maximum frequency excursion of the laser beam. Thus there is a loss of bandwidth when smooth edges are introduced on a chirped pulse, as is the case in an actual bandwidth-limited device. The total duration of the chirped pulses (including the smoothed edges) is $\tau_C = 4$ µs. For "sharp" programming pulse envelopes (shown in Figure 21 (a)), the rounded edges are very brief ($\tau_{edge} = 50$ ns each) and are intended to simulate the rise time of the AOM. In this case, the bandwidth of the edges ($\sim 1/\tau_{edge}$) is comparable to the bandwidth of the chirp, B_C. For "smooth" envelopes (shown in Figure 21 (b)), each edge makes up 10% ($\tau_{edge} = 400$ ns) of the total chirp duration. In this case, the edge bandwidth is much smaller than B_C. Although the edges on the smooth chirp envelopes have the positive effect of smoothing the pulse in the frequency domain, the edges also result in the loss of some excitation bandwidth at the edges of the chirp ($\sim \tau_{edge}\kappa/2$ at each edge). In both cases, the frequency continues to chirp linearly at the same rate ($\kappa = 3.75$ MHz/µs) over these edges, so that the total chirp bandwidth is the same for both types of chirps.
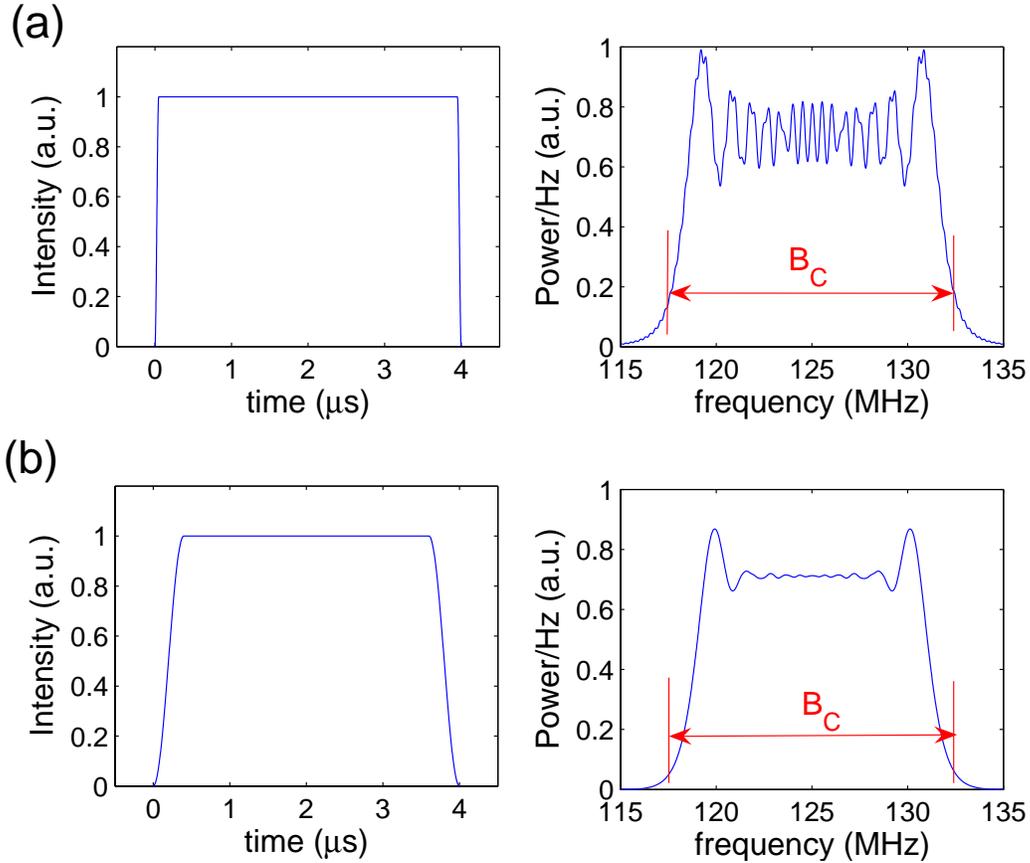
Figure 21 (a) The envelope and power spectrum of a single "sharp" chirped RF programming pulse envelope centered at 125 MHz are shown. Half periods of cosine waves (50 ns each) are used to round the edges. (b) The envelope and power spectrum of a single "smooth" chirped RF programming pulse envelope of the same total bandwidth and duration, but with 400 ns cosine edges. Both chirps have total bandwidths, B_C, = 15 MHz and duration (including edges) of $\tau_C = 4\mu s$.

As the time-bandwidth product ($\tau_C B_C$) of a chirped pulse increases, the power spectrum of the pulse in the frequency domain becomes flatter over the bandwidth of the chirp.[10] Due to the finite bandwidth and duration of any chirped pulse, however, there will always be some distortion in the power spectrum. In the simulations and experiments presented, τ_C is chosen so as to yield a moderate time-bandwidth product ($\tau_C B_C = 60$) in order to show the dramatic effect smooth edges have on the distortions in the power spectrum of the chirps, as well as to illustrate the effect of the edges on echo efficiency and uniformity in TTD sequences. In practical devices, longer chirp durations would typically be used to reduce edge effects, although the duration would ultimately be limited by the desired processing time and the upper state lifetime of the material ($T_1 \sim 800\,\mu s$ in Tm^{3+}:YAG).

Spectral Overlap of Input Pulses

Because the echo is dependent on the spectral interference of the programming pulses, the bandwidth of ions programmed by the input pulses must be considered. In the frequency domain, the two programming pulses are identical, but offset by the frequency shift Δ. Only the ions that have resonant transitions within the frequency range of the overlap of the two chirps contribute to a photon echo. Because the frequency offset increases linearly with the programmed time delay τ_D, the number of ions contributing to the echo decreases with increasing delay. For smooth programming pulses, the region of overlap is even narrower due to the loss of excitation bandwidth, which causes efficiency to fall off more quickly as a function of τ_D. The following expression approximates the full-width at half maximum programming bandwidth for the chirped programming pulses:

$$B_{prog} \approx B_C - \Delta - \tau_{edge}\kappa. \tag{23}$$

The maximum frequency offset used between programming pulses is $\Delta = 5.6$ MHz. This gives a minimum programming bandwidth of $B_{prog} \approx 9.2$ MHz for sharp programming pulses, and a minimum of $B_{prog} \approx 7.9$ MHz for smooth programming pulses. The full width at the 1/e point for the field of the Gaussian probe pulse in the frequency domain is $B_P = 5$ MHz. The duration of the probe pulse is chosen so that its bandwidth is well within the bandwidth of the programming pulses. If the programming bandwidth approaches the probe bandwidth, such that $B_{prog} \approx B_{probe}$, then a portion of the probe pulse's energy will interact with ions outside of the programming region, leading to distortion in the echo and steady loss in efficiency as Δ is increased. This effect determines the upper limit on programmable time delay using the TOLFC method. Although increasing τ_{edge} further would reduce distortion in the power spectrum, it would also decrease the programming bandwidth and the range of programmable delays. In OCT applications, chirp parameters must be chosen to provide low levels of fluctuation, while maintaining the condition $B_{prog} > B_{probe}$.

Fourier Simulation Results

Even in the weak field limit, the spectral non-uniformity of the programming pulses leads to fluctuation in echo efficiency as a function of τ_D. Because τ_D increases linearly with the frequency offset Δ between the programming pulses, the spectral interference of the non-uniform programming pulses is different for each programmed time delay. This delay dependent interference leads to non-uniform echoes for various delays. Fluctuation is defined as

$$fluctuation \equiv \frac{\eta_{rms}}{\eta_{avg}} = \frac{\sqrt{\sum_{i=1}^{N}(\eta_i - \eta_i^{line})^2}}{\eta_{avg}\sqrt{N}}, \tag{24}$$

where η_i is the echo efficiency for time delay τ_D^i, η^{line} is the value of a linear fit to the data at τ_D^i (echo efficiency tends to fall off as a function of delay, for reasons discussed below), and η_{avg} is the average echo efficiency over all time delays, which normalizes the data so that fluctuations can be compared independent of absolute efficiency. Echo efficiency η_i is defined as the ratio of the peak echo intensity at τ_D^i to the peak probe intensity. The number of time delays (N) used to calculate fluctuation is 14, with echoes uniformly spaced from $\tau_D = 416$ ns to $\tau_D = 1500$ ns, consistent with other simulations and experimental data, which are discussed below. Time delays less than 416 ns are not used because the echoes cannot be clearly resolved from the edge of the probe pulse. Longer time delays are not used because the coherence dephasing time of the

ions ($T_2 \sim 15$ µs) causes an exponential drop in echo intensity as a function of time delay, and we wish to stay in the range where this decay is small and approximately linear. The delay between the programming pulses and probe pulse is 20 µs, which is greater than the dephasing time of the ions but much less than the upper state lifetime of the ions. The relative loss in efficiency due to population decay is approximately $1 - \exp[-2(20\text{µs}/800\text{µs})] = 0.05$.

Figure 22 shows simulated echo intensities for various time delays. With the input parameters given above, the fluctuation (as defined in Eq. (3)) given by the Fourier approximation for sharp chirp envelopes is 0.04, and for smooth chirp envelopes is 0.01. The sharp edges, which introduce delay-dependent distortion in the Fourier transform of the overlapped chirped pulses, cause significant fluctuation in echo efficiency as a function of delay. The largest fluctuation, which occurs at $\sim \tau_C/3 = 1.3$µs, is the result of interference between the spectral grating and the distortions in the power spectrum of the chirped programming pulses. Fig. 1(a) shows that the distortion in the power spectrum of a chirped pulse with sharp edges has a varying spectral period. When $\tau_D \sim \tau_C/3$, the frequency offset between the chirps ($\sim B_C/3$) causes these distortions to overlap constructively, and the spectral period of these combined distortions is $\sim 3/\tau_C$ at the laser frequency. Because the programmed frequency grating has a spectral period of $1/\tau_D \sim 3/\tau_C$, the chirp distortions interfere with the grating near the laser frequency. And because the Gaussian probe pulse is centered at the laser frequency, it is the center of the grating that contributes to the echo. If the distortions are in phase with the grating, a strong echo is produced. If the distortions are out of phase with the grating, a weak echo is produced.
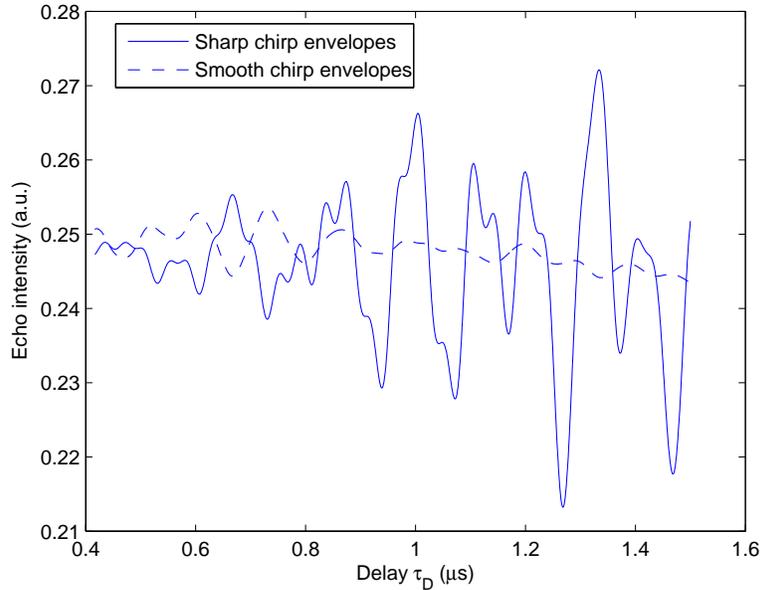

Figure 22. Echo intensities simulated by the Fourier transform approximation are shown for various time delays for both sharp envelope and smooth envelope programming pulse sequences. For sharp programming pulses, the highest level of fluctuation occurs at $\sim \tau C/3$ = 1.3µs. In both cases $\tau C = 4$ µs, BC = 15 MHz, and Bprobe = 5 MHz.

Because this interference occurs only near the center of the grating at the laser frequency, increasing the probe bandwidth, which causes ions with resonant frequencies away from the center frequency to contribute to the echo, leads to decreased fluctuation at $\sim \tau_C/3$ and a more constant level of echo fluctuation for all time delays. As we discussed above, however, the range of programmable delays is limited by the probe bandwidth, making a high bandwidth probe pulse undesirable. A better approach is to use programming pulses with smoothed edges, which lead to a much lower level of echo fluctuation while causing only a slight loss in programming bandwidth and range of programmable delay. Figure 22 shows that the smooth TOLFCs have much lower fluctuation due to their significantly smoother Fourier transforms, and there is no apparent increase in fluctuation at $\sim \tau_C/3$.

Thin Medium Bloch Simulation
Numerical simulation based on the Maxwell-Bloch equations in a thin medium constitutes the next level of complexity in OCT analysis. Saturation effects are investigated, but the crystal is assumed to be optically thin ($\alpha L \ll 1$, where α is the absorption coefficient and L is the length of the crystal), so that propagation effects do not need to be considered. The coupling between the electric field and the resonant ions being excited is characterized by the Rabi frequency, $\Omega = \mathbf{p} \bullet \mathbf{E}/\hbar$, where $\mathbf{p}$ is the ionic dipole moment and $\mathbf{E}$ is the envelope of the incident field. The peak amplitudes of the chirped programming pulses are both set to the same value, Ω_C. Because the Rabi frequency is defined only in terms of field amplitude, it has no dependence on other chirp parameters, such as chirp rate or chirp bandwidth. When the chirped pulses are overlapped, their combined field drives the ions. Figure 23 shows simulated fluctuations for various values of Ω_C. The values for chirp bandwidth, chirp duration, probe bandwidth, and time delays are the same as those used in the Fourier simulations. The peak Rabi frequency of the Gaussian probe pulse is $\Omega_P = 0.55$ MHz, chosen so that its pulse area, which is defined as the Rabi frequency (in rad/s) integrated over time, is equal to $\pi/4$. This pulse area provides a fairly strong echo signal without saturating the medium.

For small values of Ω_C, the fluctuations shown in Figure 23 are close to the values predicted in the Fourier simulations, as expected for both smooth and sharp TOLFC programming pulses in the weak pulse limit. The fluctuation increases dramatically for both types of programming pulses, however, at large values of Ω_C (>0.5 MHz). This is because the echo efficiency peaks and begins to fall off for large values of Ω_C due to saturation of the material, while the non-uniformity in efficiency for different delays continues to increase. The amplitude of the delay-dependent distortion in the power spectrum due to edge effects is smaller than the overall grating and so continues to grow approximately linearly with programming pulse strength.

For sharp programming pulses, these thin medium simulations give both a peak echo efficiency and minimum fluctuation at $\Omega_C = 0.50$ MHz. Simulations based on the coupled Maxwell-Bloch equations for an optically thick medium ($\alpha L = 2.0$) were performed with identical input parameters, giving a peak echo efficiency at $\Omega_C = 0.60$ MHz. Greater programming pulse strength is needed for maximum efficiency in this case due to propagation loss caused by absorption in the material. Experimental results discussed below, however, indicate that this value of Ω_C leads to relatively high fluctuation. Although optically thick media have the most highly efficient echoes, some of that efficiency must be sacrificed in order to have highly uniform echoes.
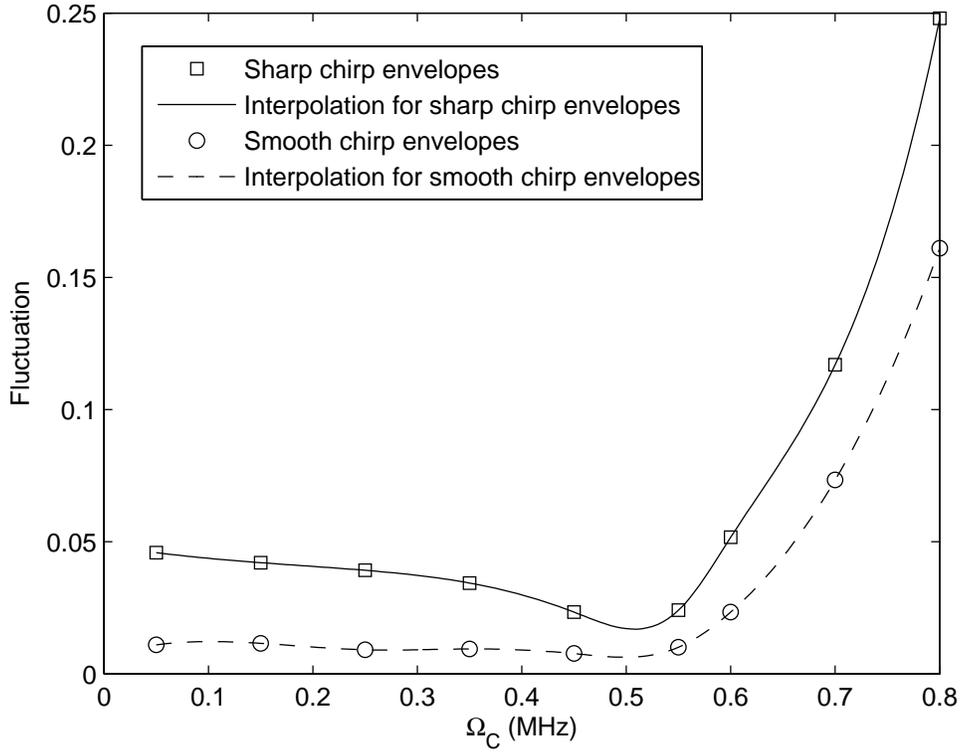
Figure 23. Simulation of echo fluctuation for an optically thin medium. Fluctuation is smaller in sequences with smooth chirped programming pulse envelopes because of the smoother power spectrum of these pulses. The increase in fluctuation for large values of ΩC indicates that this fluctuation is related to saturation in the material. Here BC = 15 MHz, τC = 4 µs, Bprobe = 5 MHz, Ωprobe = 0.55 MHz.

Experimental Results

Experiments were performed in 0.1 at. % Tm[3+]:YAG at 4 K using a λ = 793 nm Ti:Sapphire laser, which is frequency stabilized by locking to a spectral hole in the crystal. The laser beam passes through an AOM, which creates the pulses by modulating the beam's amplitude and frequency. A beam splitter is used to direct a small portion of the beam to a photodetector before the crystal, while the rest of the beam is focused into the crystal and imaged onto a second photodetector. In this way the efficiency can be determined by dividing the peak echo intensity after the crystal by the peak probe intensity before the crystal and multiplying by a calibration factor, which is obtained by sending a probe pulse through the crystal at a temperature much greater than 4 K, where there are no resonance losses, and taking the ratio of the probe intensities detected before and after the crystal. The crystal used is relatively optically thick, with αL = 2.0, which has been shown in simulations to be a good thickness for high efficiency with strong pulses. All input parameters are the same as those used in the simulations described above, and all data are averaged 60 times. The quoted Rabi frequencies are based on the peak amplitude at the spatial center of the beam.

Figure 24(a) shows experimental echo efficiencies for various time delays (the same delays used in simulations), programmed with sharp programming pulse envelopes. The greatest

efficiency occurs for $\Omega_C = 0.60$ MHz, consistent with results from Maxwell-Bloch simulations. The consistent oscillatory behavior of the efficiencies demonstrates that the fluctuations are deterministic and not random. Figure 24(b) shows echo efficiencies for the same set of delays and programming pulse areas, but now with smooth programming pulse envelopes. A slight increase in efficiency is apparent for all programming pulse strengths with smooth chirp envelopes compared to sharp programming pulse sequences. This may be due to the smooth programming pulses having more uniform spectral distributions, which causes less of the echo energy to be spread into sidebands.
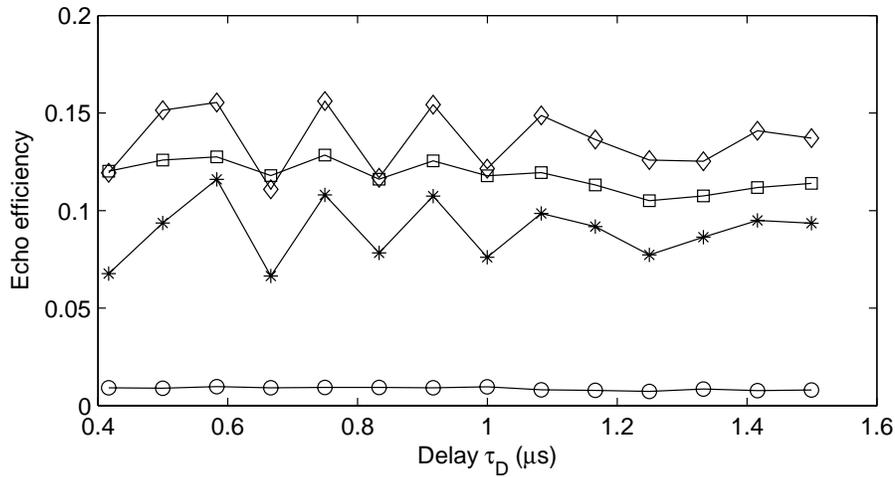
(a)
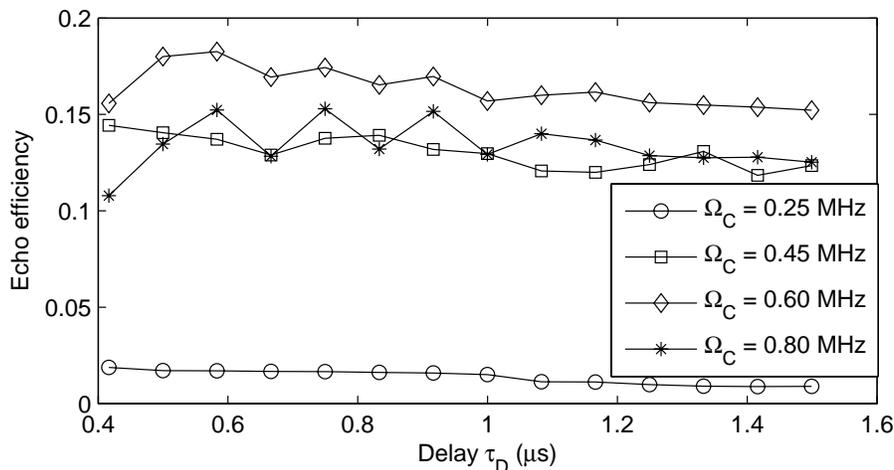
(b)

Figure 24 (a) Experimental values of echo efficiencies for various programmed time delays with sharp programming pulse envelopes. The peak efficiencies occur for $\Omega C = 0.60$ MHz, although this comes at the cost of large fluctuations. (b) Experimental values of echo efficiencies programmed with smooth programming pulse envelopes. These echoes display greater efficiency and uniformity than those shown in (a). In both plots, BC = 15 MHz, $\tau C = 4$ μs, Bprobe = 5 MHz, and Ωprobe = 0.55 MHz
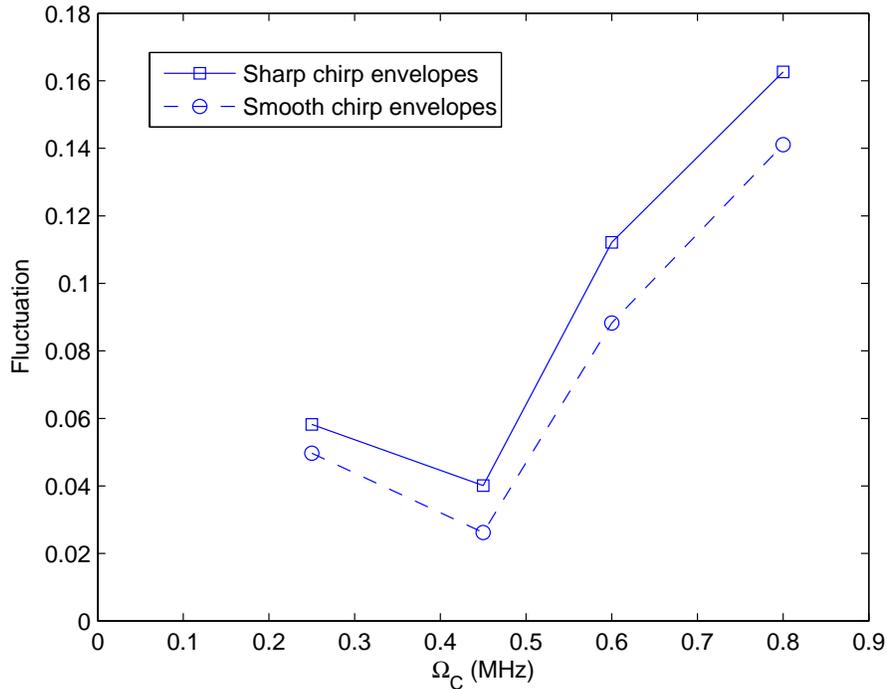
Figure 25. Experimental echo fluctuations, calculated from the data shown in Figure 24. As expected from simulations, smooth programming pulse envelopes generate echoes with slightly less fluctuation. Experimental noise explains the high values compared with simulation for small values of ΩC, where the echo intensity is low and close to the noise floor. Here BC = 15 MHz, τC = 4 μs, Bprobe = 5 MHz, and Ωprobe = 0.55 MHz.

Figure 25 shows experimental echo fluctuations calculated from the data shown in Figure 24. The minimum fluctuation occurs at Ω_C = 0.45 MHz, showing that there is a trade-off between echo efficiency and uniformity in an optically thick medium. Fluctuations are lower for smooth programming pulse sequences than for sharp programming pulse sequences for all values of Ω_C, consistent with results from thin medium simulations. This can also be attributed to the lower level of distortion in the power spectrum of these pulses. A higher level of fluctuation for Ω_C = 0.25 MHz is apparent in the experimental results shown in Figure 25 compared to the simulations shown in Figure 23. This is probably a noise-related effect. Because the echo intensity for Ω_C = 0.25 MHz is very weak, the signal and noise are at comparable levels. The noise thus contributes significantly to the fluctuations as calculated.

Summary of efficiency and fluctuation work
Efficiency and fluctuation in photon echo sequences have been examined through experiment and simulation. Similarities between experimental results and thin medium simulations have shown that propagation effects do not contribute significantly to echo fluctuations in a thick medium. The main contributors to non-uniform echo efficiency are programming pulse edge effects and material saturation due to strong programming pulses. Using smooth edges on the programming pulse envelopes, although causing a slight loss in programming bandwidth, has a

significant benefit of both increasing efficiency and decreasing fluctuation. The fluctuations are greater for large programming pulses because the echo efficiency saturates, while the distortion in the power spectrum continues to grow.

There is ultimately a trade-off between echo efficiency and uniformity. An OCT device that requires a high degree of echo uniformity must be programmed with weaker pulses than a device that requires maximum efficiency at the cost of increased fluctuation, while other devices may be used with intermediate operating conditions as a compromise between these two factors. In general, minimized fluctuation ($\Omega_C \sim 0.5$ MHz) can be obtained with only a slight sacrifice in efficiency. Smoothed edges on programming pulse envelopes have the effect of increasing overall efficiency and lowering fluctuations for all values of Ω_C, although they do cause a greater falloff in efficiency for longer delays. The choice of programming pulse strength and shape ultimately depends on the application, but the results presented here will act as a guide in the determination.

2.9. Cascaded injection-locking for broadband optical signal amplification

Amplification of high bandwidth phase modulated optical signals from an electro-optic modulators (EOM) at 793 nm (the $^3H_6$-$^3H_4$ transition in Tm^{3+}) has been experimentally demonstrated using an injection locking technique[3] to meet the power requirement to program and probe spectral gratings for pulse shaping and AWG applications. However, a bandwidth limitation of ~3 GHz for CW phase modulated signals was found for high gains (16dB) associated with output powers of ~80mW. To explore the techniques for optical signal amplification beyond 3GHz, we designed a cascaded injection locking system. We obtained the amplification of 1mW input to 70 mW output with bandwidth up to 9 GHz. Figure 26 illustrates the maximum bandwidth is inversely proportional to the square root of the output power of the slave laser. Thus, lowering the output power for a fixed input allows higher bandwidth for CW phase modulated signals. In our case, however, the optical signal to be amplified came from an electro-optical modulator (EOM) with optical power limited to less than 1 mW and the goal was to obtain an output power in the range of 50 –100 mW. In order to achieve high bandwidth and high amplification gain simultaneously it requires two cascaded slave lasers to amplify the optical signals successively, with the output of the first slave injected into the second slave. For a given injected power to the system and desired output power, one can maximize the bandwidth by adjusting the output power from the first slave laser.

In our experiment, we used an external cavity diode laser modulated by an EOM as the master laser and two similar free-running anti-reflective coated diode lasers as the slaves. The input powers of the CW phase modulated light just outside the first and the second slave lasers were 1 mW and 5 mW, respectively. The output powers just outside the first and second slaves were 20 mW and 70 mW respectively. The two slaves were locked with the master and the locking was stable up to 9GHz. Figure 27 shows the typical spectra of the cw phase modulated optical output signals from the master (a), the first (b) and the second (c) slave lasers.

We have demonstrated amplification (with 18 dB gain) of weak optical signal (~1mW) up to 9GHz bandwidth using a cascaded injection locking system. Whether this is the best amplification technique remains undecided until the investigation on the tapered semiconductor amplifier is completed.
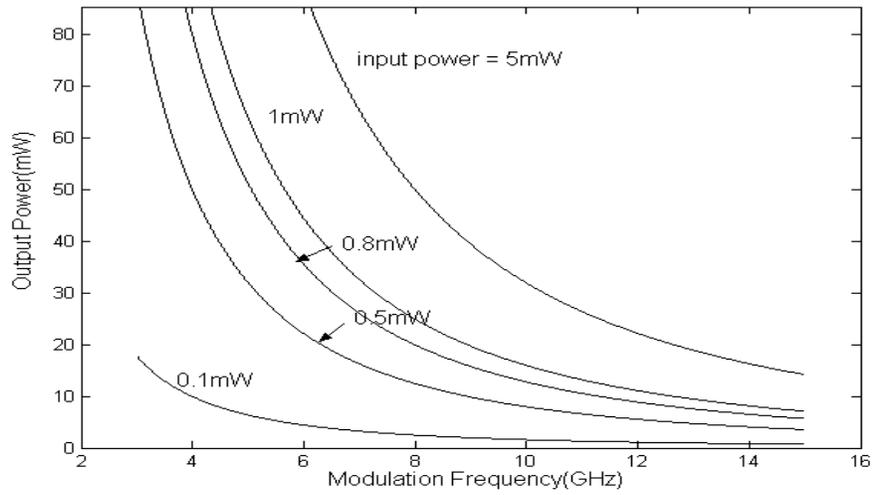
Figure 26. Relation between maximum bandwidth of CW phase modulation and output power of the injection locking system for various input power as marked in the plot.
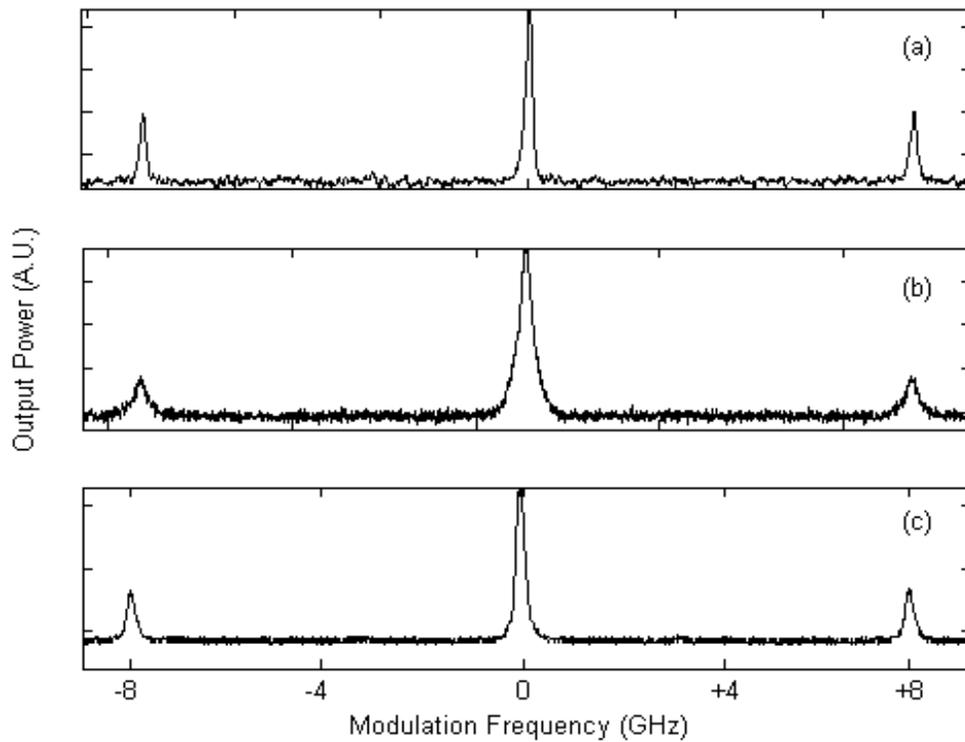
Figure 27. The spectra of 8 GHz CW phase modulated signals in cascaded injection locking system from (a) master laser; (b) the first slave, and (c) the second slave. Each spectrum is normalized to the peak at its carrier frequency

2.10. Tapered semiconductor optical amplifier

Compared to the cascaded injection–locking amplifier, the advantages of using tapered amplifier include less optical and electronic parts required, low cost and reliability. We built and tested an amplifier using the tapered amplifier chips made by Eagleyard Photonics. The optical parts involved are two fiber coupler ports for input and output to the chip, two optical isolators, and a beam shaping optics. The chip consists of an anti-reflection coated tapered gain region, which allows the user to inject a weak optical signal on the narrow end of the taper and an amplified signal emits on the broad end. The system is shown in Figure 28.

We completed the design and build of a broadband optical amplifier system using semiconductor tapered amplifier chips. Several iterations of the design were performed based on the results of preliminary characterization.   The characterization is now completed and the results are favorable. The power output of the amplifier is up to 500mw from the chip itself and we have ~150mW of fiber-coupled output power. The measured gain is about 14 dB. These levels are sufficient for carrying out high bandwidth AWG programming and probing experiment
.
Amplifier setup
The tapered amplifier (TA) setup was designed to be as inexpensive and easy to piece together as possible.   The system is injected with a fiber coupled ECDL that is z-folded into the first coupling lens. This lens is mounted in a xy lens mount that is mounted to a translation stage for fine control of z. The input is fed into the TA where it is amplified and sent into the output lens. The output is of similar design to the input without the translation stage. The beam exits the TA with a diverging horizontal beam that goes through a cylindrical lens to collimate it.   The cylindrical lens being used is not the correct one so the beam is also going through a prism pair to further reduce the spot size. The amplified beam then goes through an optical isolator (OI), to protect the TA from any feedback, and finally is fiber coupled on the output.
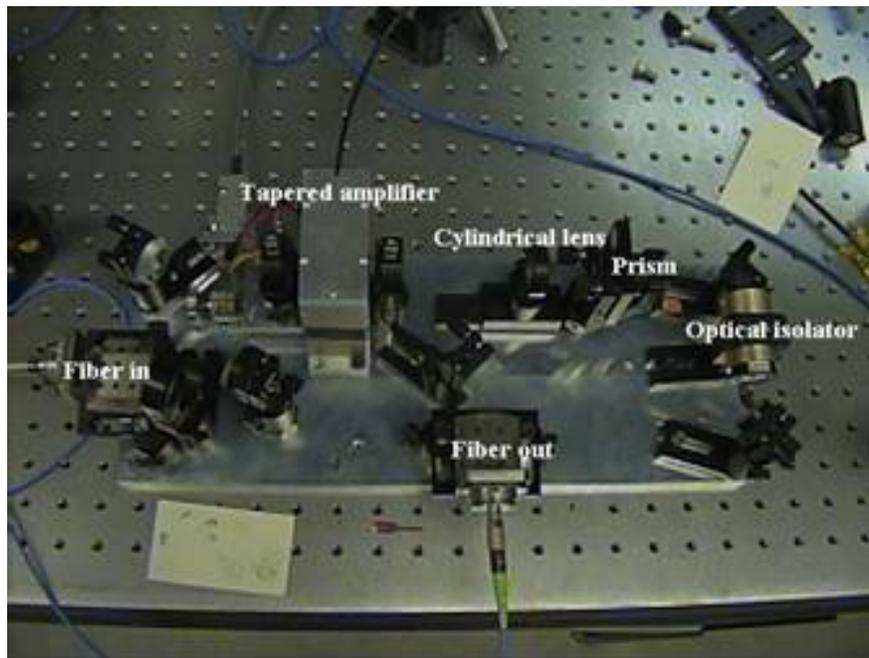
Figure 28 The tapered amplifier system with labels

Tapered amplifier characterization

Before the amplified beam was sent through the OI and output fiber, extensive characterizations were done with different currents and injection powers. The results are shown in Figure 29, Figure 30, and Figure 31. The seed laser was injected into the TA with 16.34mW of power and the system was allowed to stabilize to 24˚C. The current was set at 1A to begin and measurements of the amplified output power and amplified spontaneous emission (ASE) were made. The current was then raised in .1A increments up to 1.8A, with amplified power and ASE power measurements taken at each point. At a current of 1.8A the output was 235.3mW with 16.24mW due to the ASE emission. These measurements were done several times to ensure that the TA was performing correctly and that the data was reliable.
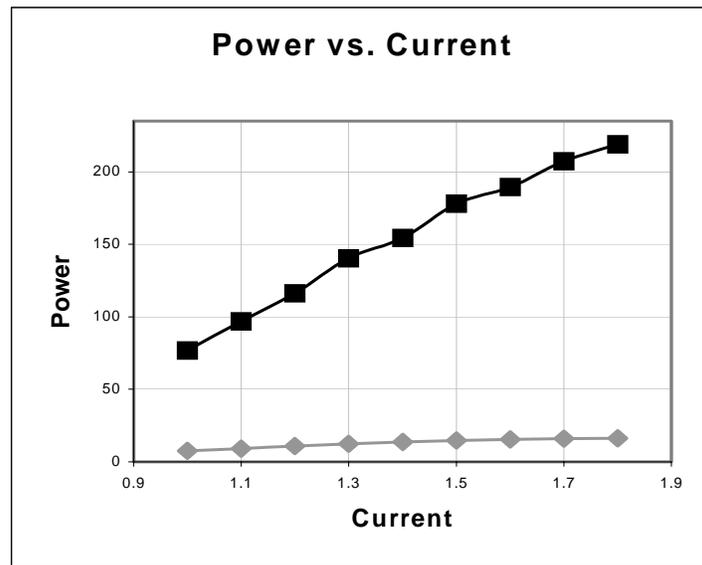
Figure 29. Characterization data for tapered amplifier. Grey is unseeded TA, black is the amplified seed. The maximum at 1.8A with input of 7mW
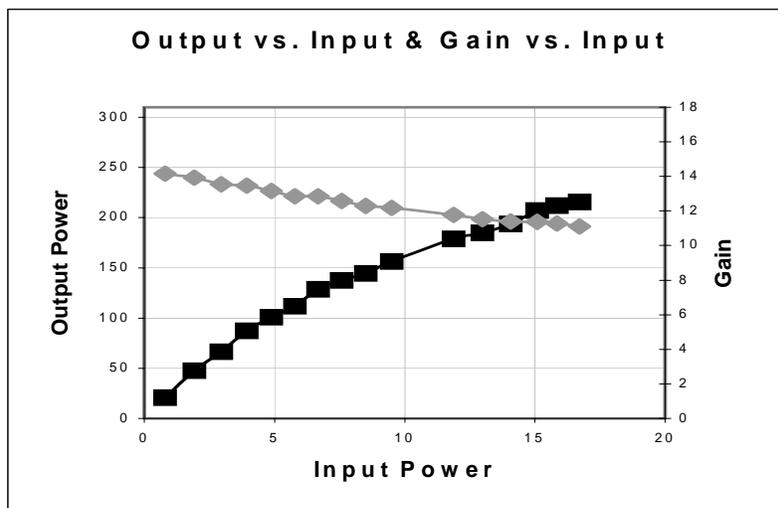
Figure 30 The black line is the amplified out put power (without ASE) vs. the seed laser input power. The gray line is the gain (in dB) vs. the input power.

Gain
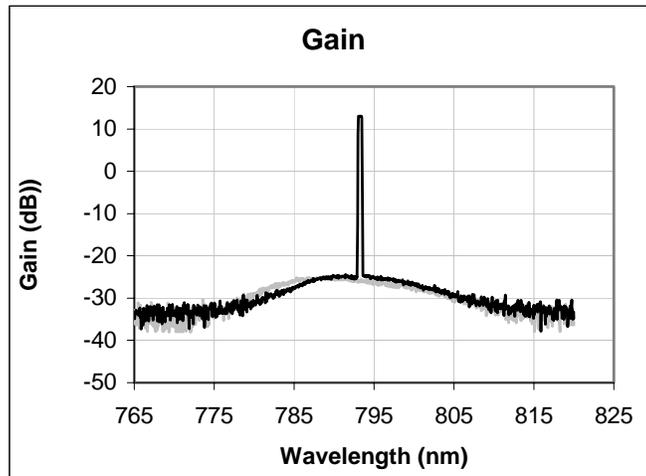
Figure 31. Tapered amplifier output with input of 16mW at 1.8A (black line) and unseeded (gray line).

Several measurements were also taken to see how the TA performs with different input powers. The amplifier's current was set to 1.8A and the seed lasers current was raised from an input power of .801mW to an input power of 16.72mW. The maximum amplified power with an input of 16.72mW is 231.6mW with 15.84mW due to the ASE. This is giving a gain of about 11.5dB that may go up as components are realigned.

The work on the tapered amplifier was aided considerably by co-development that was going in Kelvin Wagner's group at CU.

2.11. *Frequency chirped laser sources up to 10 GHz*

The chirped laser design we originally planned to pursue based on Levin's design did not meet the requirement of the OCT devices. Kevin Repasky, now an assistant professor of electrical engineering at MSU, was working with AdvR of Bozeman to produce a waveguide laser that can chirp over several GHz and can be packaged in a compact butterfly package. Unfortunately, that work was delayed and is now being pursued (as of January 2005) through collaboration between Spectrum Lab and AdvR, supported under a DARPA project. Elizabeth Noonan of AdvR joined Spectrum Lab as a PhD candidate in Physics and is working on the design and characterization of electro-optic tuned waveguide lasers. The results will extend beyond our needs for a tunable laser for broadband OCT devices and S2CHIP devices and provide AdvR with valuable results on the tuning range of their KDP waveguides. The data from this laser are included here as an indicator of the stability of a well-packaged EO tunable laser. The operation of an electro-optically tunable Bragg grating ECDL will be evaluated under another program.

Electro-Optically Tuned External Cavity Waveguide Lasers
The ability to tune an external cavity diode laser (ECDL) for either long term stability or frequency chirping is useful in areas of research such as microwave photonics, optical processing, and remote sensing. Currently, lasers that are narrow in linewidth are relatively narrow in tuning range. Likewise, those with a wide tuning range tend to have a wider linewidth.

The ECDL designs based on external grating and intra-cavity electro-optic EO tuning have alignment and vibrational stability issues that make them impractical for most applications. A waveguide embedded in potassium titanyl phosphate (KTP) shows great promise as the core component of an external cavity diode laser, which will offer both narrow linewidth and wide tuning range, while also being providing stable and continual operation in environments with significant vibration. For this purpose a semiconductor laser will be stabilized by optical feedback from a waveguide containing a Bragg grating embedded in KTP. A non EO version of such the laser has shown stable operation even under conditions of significant vibration.

Design
The basic design and operation of an electro-optically tuned ECDL using a waveguide embedded in KTP is shown in Figure 32.
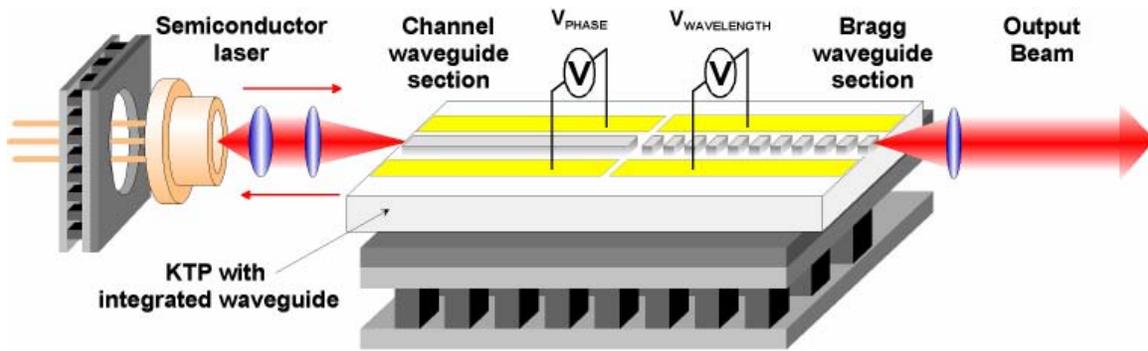
Figure 32. A schematic of a Bragg grating stabilized diode laser is shown. Optical feedback from the Bragg section of the KTP waveguide stabilizes and tunes the wavelength of the semiconductor laser. (Drawing supplied by AdvR, Inc.)

The operation of the laser will depend on the characteristics of the diode laser and the Bragg grating as well as the component between them, including the non Bragg portion of the waveguide. The main characteristics of the diode laser that are important are the reflectivity of the back facet, the AR coating of the front facet, the gain profile of the diode.

One characteristic of the Bragg grating is the effective index of the waveguide. This is determined by looking at both the index of refraction of the bulk KTP as well as the modal index of the ion-exchanged sections containing a combination of KTP and RTP. The index of refraction of the bulk KTP is determined by the Sellmeier equations,

$$n(\lambda) = \sqrt{A - D\lambda^2 + \frac{B}{1 - \frac{C}{\lambda^2}}} \qquad (25)$$

where A, B, C, and D are material dependant coefficients. The amount of Rubidium in this section depends on factors such as exchange time and temperature and is determined experimentally.

The frequency of light that is reflected due to a Bragg grating is

$$v_{Bragg} = \frac{cm}{2n_{eff}\Lambda}$$

(26)

where m = 1, 2, 3…, n_{eff} = the effective index of the waveguide, Λ=The Bragg period, and c=speed of light. The main electro-optic characteristic of the KTP is that the index of refraction can be modified by applying an electric field. An optical field with polarization parallel to the z axis of the crystal will experience a change of index given by:

$$\delta n = \frac{1}{2} n_{eff}^3 r_{33} E$$

(27)

where E is the magnitude of the external electric field applied parallel to the z axis, and r_{33} is the electro-optic coefficient.

When an electric field is applied through the Bragg grating it changes its index of refraction. In the equations above, we see that this changes the reflected frequency. Putting the above equations together

$$\delta v = -\frac{cmnr_{33}E_{Bragg}}{4\Lambda}$$

(28)

We see that we can change the wavelength of the laser linearly with a change in electric field.
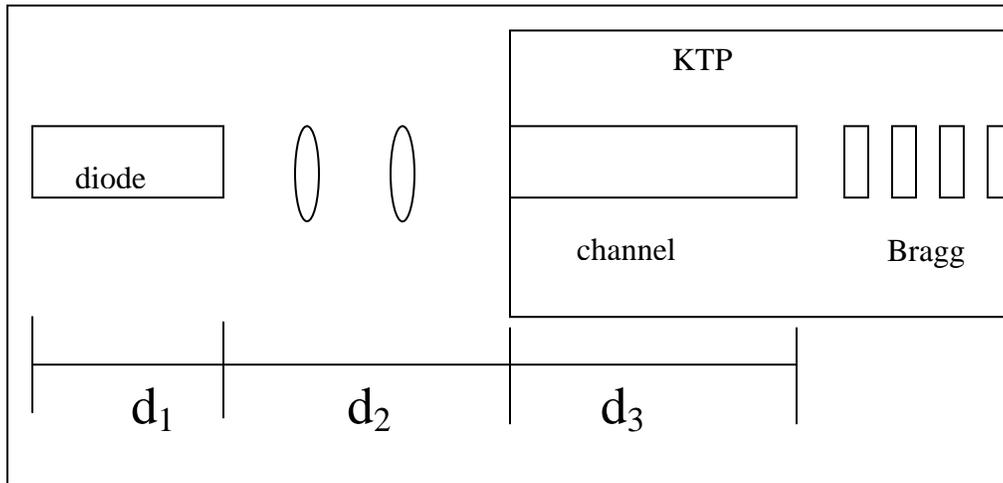
Figure 33. A schematic drawing of the ECDL. For phase tuning we need to determine how the electric field inside the non-Bragg section of the KTP affects the optical path length of the cavity.

The frequencies allowed in a Fabry–Perot cavity are:

$$v = \frac{qc}{2d} \qquad \text{where } q\text{=1,2,... and } d = \text{optical path length of cavity}$$

(29)

The external cavity of the proposed laser has length d = d_1 + d_2 + d_3. Where d_1 is the optical path length inside the gain medium, d_2 is the free space path length outside of the diode and waveguide and d_3 is the optical path length within the non-Bragg section of waveguide.

By using the electro-optic response of the KTP we can change the index of refraction inside the waveguide (for the distance d_3) and therefore change the frequency supported for the ECDL cavity. We can see that a change in the path length (d) will offer a change in the frequency.

$$\Delta \nu = -\frac{qc}{2d^2}\Delta d$$ (30)

$$\text{where } \Delta d = \Delta d_3 = \Delta n l_3$$

Combining equations we get:

$$\Delta \nu = -\frac{qcn_{eff}^3 r_{33} l_3 E_{phase}}{4d^2}$$ (31)

If we change the frequency supported in the ECDL at the same rate at which we change the Bragg frequency, we will have mode-hop free tuning. By setting equal and allowing the index of refraction of the two sections of KTP to be equal

$$E_{phase} = \frac{d^2 \lambda_{Bragg}}{qn_{eff}^3} E_{Bragg}$$ (32)

The variables in front of E_{Bragg} are constants. We can tune the phase and Bragg with a single voltage source and a voltage divider. The range of tuning is limited to the applied electric field.

Determination of the affect of the electric field in the KTP waveguide
To determine the voltage necessary for the frequency tuning one must determine the size of the electric field and the distance between electrodes:

$$V = \int E \bullet dl$$ (33)

The placement of the electrodes across the KTP determines the shape of the electric field. By placing them coplanarly we can keep them closer together compared to the ~1mm capacitive setup required to sandwich the KTP. This will increase the electric field by orders of magnitude.
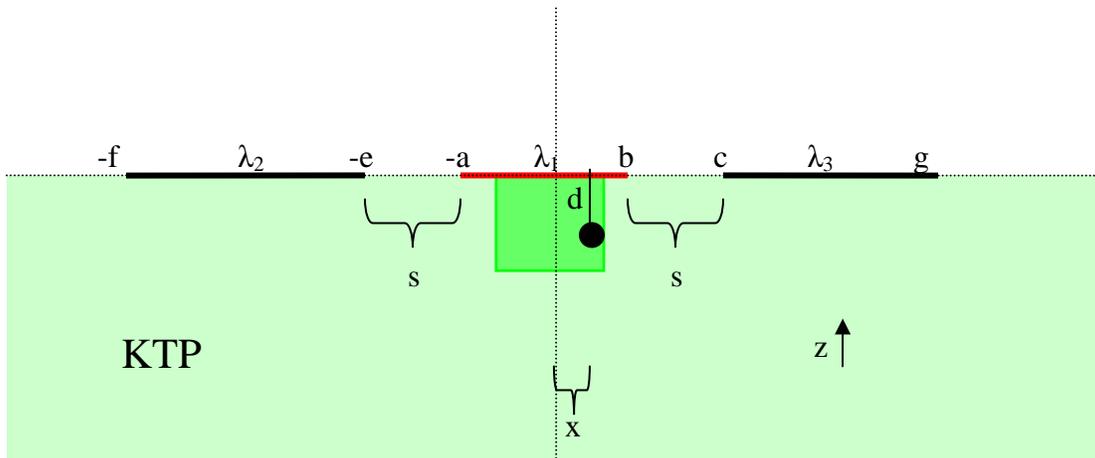
Figure 34. Diagram shows the electrode configuration on the KTP. By placing the anode (red) directly above the waveguide we can maximize the electric field in the z direction.

Figure 34 shows a coplanar configuration of electrodes the electric field for a point in the KTP and distance d from the x axis. The electric field must take into consideration edge effects of the electrodes from the electrodes in both x and y directions as the waveguide is separated from the electrodes by epoxy a thickness that is on the order of the waveguide thickness. This electric field is very difficult to determine. However, using finite element analysis one can iteratively approach the steady state potential field inside the KTP by merely apply the boundary conditions of the voltage on the electrodes. The distribution of the charge on the electrodes will not be uniform throughout, but this will be a fair assumption to within first order.
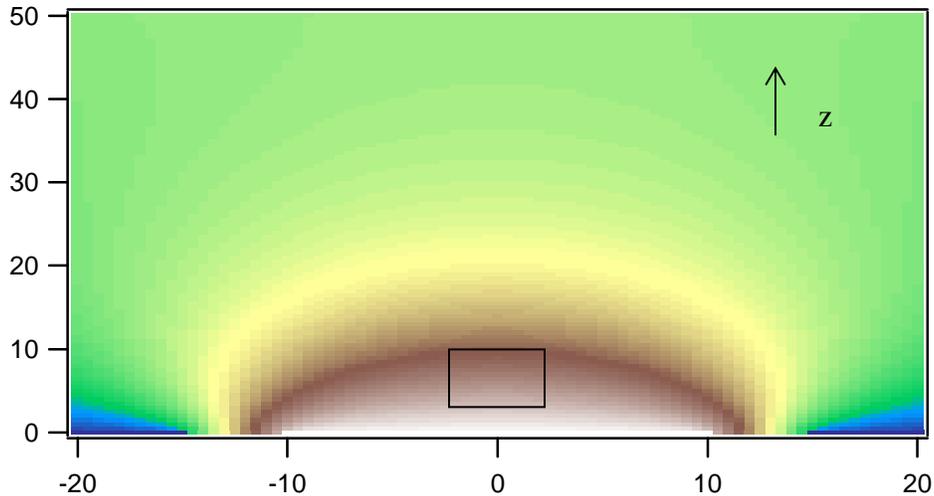
Figure 35. The image of a potential field inside KTP with an electrode configuration as described in Figure 34(cathode is white and anodes in blue). The typical waveguide dimensions are 4 µm wide and 8µm deep (axes are in µm).

From Figure 35 we see that the potential field inside the waveguide (black box) is uniform in the z direction. We are using vertically polarized light and the only useful part of the electric field is the z component. The above numerical calculation is a 2D representation. Further numerical analysis needs to be done to determine the optimal electrode configuration, especially when 3D considerations are included.

Further work on the tunable waveguide laser is being continued under our DARPA contract.

2.12. *Potential application and specifications*

Several potential application areas have been studied and competing technologies have been assessed. The competing technology of femtosecond pulse shaping has not progressed significantly over the past few years and the need for AWG and pulse shapers that can operate at over 100 GHz bandwidth with time-bandwidth products greater than 1000 still exist, though the market at the moment is mostly scientific.

On the lower speed end of the competition, electronics is continuing to improve, though slowly. Current electronic AWGs are achieving a few GHz operation. The leading competition is the Tektronix AWG710B, which has a 2 GHz bandwidth, produces 4.2 gigasamples per second, with memory up to 64 megasamples, and about 6 bits of accuracy. The units sell for over $60K. S2

materials and OCT technology could meet and exceed the bandwidth of current electronics and with comparable specifications utilizing current chirped optical sources, but the performance advantage (less than a factor of 2 in bandwidth) is not sufficient for market entry with a radically new technology. Extension of OCT AWG technology to the 10 GHz and beyond would be required, but achieving these regimes of operation will require supporting technology to be developed: mainly optical chirped sources.

True-Time-delay is another application that is promising for OCT technology. The requirement is for a true-time-delay that has up to 20 GHz bandwidth with extremely high dynamic range. The impediments to market entry are again supporting technologies: optical chirped sources and shot noise limited high bandwidth detectors. If the supporting technologies are developed, the market would be significant, not only in military application, but in civilian applications that require the directional performance of phase arrayed antenna.

The pulse shaping market is not as straight forward and it is not clear that a large market exists for complex pulse shaping. Simple pulse shapers (chirp compensating fibers) exist and perform a very specific job up to 40 GHz bandwidth for telecommunication applications.   Full performance complex pulse shapers will not be needed in telecommunication until the fiber capacity is pushed to its limits. Given the current over capacity of fiber, this could be decades. Other areas for pulse shaping are scientific and the market for a stand alone unit is not large.

The cryogenic requirements of OCT technology are no longer an impediment to market entry. Our collaborator on our DARPA project, Northrop Grumman, has closed cycle cryo-coolers that are less than a cubic foot and provide all the cooling requirements needed for OCT technology. The advancement of super-conducting digital electronic is pushing the commercialization of these cryo-coolers.   There use in a number of military applications has greatly reduced the reluctance of defense agencies to pursue cryogenics technologies.

2.13.   OCT materials with bandwidth more than 20 GHz

Prof. Rufus Cone's group in the Physics Department of Montana State University has developed (under separate grants) several materials for use in OCT devices. Most notable is the Tm doped material (Tm:LiNbO$_3$) that has 300 GHz of bandwidth, a relatively narrow linewidth (sub-MHz), and a higher oscillator strength than the materials we are currently using. This will enable OCT technologies to be extended to up to several hundred GHz of bandwidth, provided supporting technologies are developed to meet the requirements. The development of crystals by Prof. Cone's group and Scientific Materials is summarized in the following table produced by Prof. Cone (Figure 36), which is a list of currently well-known materials. Materials with greater than 20 GHz bandwidth are currently available at 793nm (our currently operating regime) and at 1.5 microns (where telecommunications technology can be leveraged). Prof. Cone has also studied potential S2 materials that can work at other wavelengths with over 200 GHz of bandwidth. He has identified 13 materials that work across the wavelength span of 650nm to 1800nm. The broad range of potential operating wavelengths affords supporting technologies flexibility in meeting the requirement of high bandwidth OCT technologies.

	Γ_H (kHz) $(1/\pi T_2)$	Γ_{in} (GHz) $(1/\pi T_2^*)$	Γ_{In}/Γ_H	T1 (ms) Lifetime	Center λ(nm)
Tm: YAG	3.0 (@1.5K)	20	6.6×10^6	10	793.22
Tm: YGG	0.72 (@1.4K)	60	8×10^7	3.3	795.16
Tm:YLuAg	0.72 (@1.4K)	270	4×10^8	3.3	793.02
Tm:$Y_2Si_2O_7$	14 (@1.24K)	100	7×10^6	10	790.427
Tm:Y_2SiO_5(1)	57 (@1.3K)	2.6	4.5×10^4	10	791.05
Tm:Y_2SiO_5(2)	145 (@1.3K)	4.5	3.1×10^4	10	791.15
Tm:Chelates	2×10^5 (@1.4K)	3000	4.1×10^4	10 hrs	795
Er:$LiNbO_3$	1.9 (@1.5K, 20 kG)	200	1×10^8	1.2	1531.52
Er:Y_2SiO_5	0.55 (@1.5K, 55 kG)	0.5	1×10^6	13	1536.14
Er:YAG	4.2 (@1.7K)	30	7.1×10^6	0.030	1527
Er:$YAlO_3$	1.2 (@1.5K, 40 kG)	1	8.3×10^5	1.0	1514.38
Er:Y_2O_3	17.7 (@1.5K, 0 kG)	1	5.6×10^4	1.0	1535.28
Eu:Y_2SiO_5(1)	0.122 (@1.4K, 100 G)	4.1	3.3×10^7	days	579.88
Eu:Y_2SiO_5(2)	0.167 (@1.4K, 100 G)	3.8	2.3×10^7	days	580.05
Eu:$YAlO_3$	5.3 (@2.0K)	4.0	7.5×10^5	>1 hour	578.5
Pr:Y_2SiO_5(1)	2.8 (@1.4K)	4.4	1.6×10^6	Secs-days	605.977
Pr:Y_2SiO_5(2)	1.0 (@1.4K)	2.5	2.5×10^6	Secs-days	607.934
Pr:$YAlO_3$	4.0 (@1.9K)	3.8		0.160	610.5

Figure 36 Table of OCT materials and their characteristics relevant to OCT devices.

2.14. OCT TTD Control Using Acousto-Optic Distributed Local Oscillators (CU)

Prof. Kelvin Wagner's research group at the University of Colorado was subcontracted and tasked with designing and building an acoustooptic (AO) counter-propagating chirp control system for integration with optical coherent transient (OCT) processors being developed at Montana State University. They built an AO sub-system consisting of a pair of high efficiency acousto-optic Bragg cells with counter-propagating chirps applied, such that the diffracted field in an image plane consists of an array of Doppler shifted beams, where the Doppler shift varies linearly in space. Such a system can be used to either control MSU's true-time-delay (TTD) radio-frequency (RF) antenna beamsteering system or to record an optical scanner using chirp frequency shifts by an array of distributed local oscillator (DLO) Doppler shifted beams. For the TTD control system the rate of Doppler shift variation in space was controlled by the chirp rate

of the applied chirps. A low bandwidth OCT scanner was also built and tested in an OCT-based time-integrating correlator using only one acousto-optic Bragg cell for the programming of the OCT. This experiment acted as proof-of-concept demonstration, and illustrates that one can in fact record and later read out parallel banks of OCT processors. A full report on CU's efforts is given in Appendix A.

3. Personnel Supported

At MSU:
Senior personnel: Wm. Randall Babbitt. PI, professor
                     Mingzhen Tian, Co-PI, research scientist.
Other personnel: Norm Williams, machine shop supervisor
Graduate students: Hongyan Li, Steve Jia. Ijaz Zafarullah
Undergraduate students: Zeb Barber, Jason Dahl, Joe Fischer, Katrina Kujawa,
                          Christoffer Renner, Jim Murray
At CU:
Senior personnel: Kelvin Wagner
Graduate student: Friso Schlottau

4. Education and industrial interaction

Along with the major achievements described above, this work has met its other goals as outlined in the education and industrial interaction sections. This grant has directly supported the research of 4 Graduate and 6 undergraduate students. One of these students, Friso Schlottau at CU, has received his Ph.D. Ijaz Zafarullah, a graduate student at MSU working with the project, has gained valuable experience while assisting experiments for the project that enabled him to lead experiments in another projects in related fields. The undergraduates worked closely with the graduate students and PI's, receiving valuable training in physics, optics and, electronics. Zeb Barber and Jim Murray (both undergraduates at MSU) published in peer-review journals with first authorship. During this project the joint team worked with professionals nationwide. A strong cooperation has been built with local industries at Bozeman, Montana, such as ADVR, Scientific Materials, and S2 Corporation. We have contracted their work in various ways to assist the goals of this project. Collaboration between the research team with Spectrum Lab and other research groups at MSU (including Professors Cone and Repasky) has produced enabling techniques and devices, novel materials, and simulation tools for indispensable to the project. The techniques and knowledge gained through the collaboration have benefited various federal and state supported projects in the involved groups. Overall, the OCT technology has advanced by the generous support of AFOSR under this grant, which has found an extended array of applications in rf signal processing, spectral analysis, and quantum information storage and processing.

5. Publications fully or partially funded by this grant
5.1. Peer review journal

1. Z. Barber, M. Tian, R. Reibel, and W. R. Babbitt "Optical pulse shaping using optical coherent transients", Opt. Exp. 10, 1145 (2002)

2. R. Reibel, Z. Barber, M. Tian, W.R. Babbitt, Z. Cole, and K.D. Merkel, "Amplification of high bandwidth phase modulated signals at 793nm," J. Opt. Soc. Am. B. 19, 2315 (2002)

3. L. Tsang, C. Sjaarda Cornish, and W. R. Babbitt, "Analytic Solutions of the Maxwell-Bloch Equations for High Photon Echo Efficiency of Multiple Pulse Sequences," JOSA B 20, 379-390 (2003)

4. T. Chang, M. Tian, Wm R. Babbitt, "Numerical modeling of optical coherent transient processes with complex configurations— II. Angled beams with arbitrary phase modulations", J. Lumin. 108,138 (2004).

5. T. Chang, M. Tian, Wm R. Babbitt, "Numerical modeling of optical coherent transient processes with complex configurations—I. Angled beam geometry" J. Lumin. 108,129 (2004).

6. T. Chang, M. Tian, R. K. Mohan, C. Renner, K. D. Mekel, and W. R. Babbitt, "Recovery of spectral features readout with frequency-chirped laser fields", Opt. Lett. 30, (2005).

7. Jim Murray, Hongyan Li, Mingzhen Tian, Tiejun Chang, and W. Randall Babbitt, "Efficiency and uniformity considerations in optical coherent transient devices", accepted by JOSA B.

8. F. Schlottau and K. Wagner,Demonstration of a continuous scanner and time-integrating correlator using spatial-spectral holography Journal of Luminescence, Vol 107, no 1-4, pp 90-102, 2004.

5.2. Participation/presentation at meetings, conferences, seminars

Talks: (*: Presenter)

1. Wm. Randall Babbitt*, "Overview of Activities in Optical Coherent Transient Signal Processing", OpTeC'2002 (Sept. 13-14, 2002, Bozeman, Montana).

2. Zeb Barber*, "Optical Pulse Shaping using Optical Coherent Transients", OpTeC'2002 (Sept. 13-14, 2002, Bozeman, Montana).

3. Zeb W. Barber*, Jesse Law, Mingzhen Tian, and W. R. Babbitt, "Optical Coherent Transient High Bandwidth Arbitrary Waveform Generation and Pulse Shaping", HBSM'2003, (Jul. 27-31, Bozeman. Montana).

4. Randy R. Reibel*, Tiejun Chang, Mingzhen Tian, and W. R. Babbitt, "Optical Linear Sideband Chirp Compression for Microwave Arbitrary Waveform Generation," Proc. of Topical Meeting on Microwave Photonics (MWP 2004), Ogunquit, Maine, October 4-5 2004.

5. T. Chang, M. Tian*, R. K. Mohan, C. Renner, K. D. Merkel, W. R. Babbitt, "Recovery Technique for Chirped Readout of Spectral Features", ", CLEO2005, May 22-27 2005, Baltimore, MD.

6. C. J. Renner*, T. Chang, R. R. Reibel, M. Tian, W. R. Babbitt, "Photonic Chirp Compression and Arbitrary Waveform Generation for Micro- and Millimeter-Wave Applications", CLEO2005, May 22-27 2005, Baltimore, MD.

7. Kelvin H. Wagner, Friso Schlottau, and Jaap Bregman, Array Imaging Using Spatial-Spectral Holography, Optics in Computing, Taiwan, 2002.

8. Kelvin Wagner, Friso Schlottau, and Jaap Bregman, "Array Imaging using Spatial-Spectral Holography", IOG Information Optics meeting, Mannheim Germany, September 19-20, 2002.

9. V. Lavielle, J.L. LeGouet, I. Lorgere, F. Schlottau, and K. Wagner, Efficient engraving of dispersive filters for time-to-frequency Fourier transform, Hole burning and related spectroscopies, Bozeman, MT, July 2003.

10. Friso Schlottau and Kelvin H. Wagner, Demonstration of a Continuous Scanner and Time-Integrating Correlator using Spatial-Spectral Holography, Hole Burning and Single Molecules, HBSM03, Bozeman, MT, July 2003.

Posters: (*: Presenter)

1. Steve Jia* "Cascade Injection Locking System for Amplification of High Bandwidth Signals", OpTeC2002 (Sept. 13-14, 2002, Bozeman, Montana).

2. Hongyan Li* Steve Jia, Randy Reibel, Zeb Barber, Joe Fischer, Mingzhen Tian, and Wm. R. Babbitt, "Demonstration for Highly Efficient True Time Delay with OCT", OpTeC'2002 (Sept. 13-14, 2002, Bozeman, Montana).

3. Hongyan Li*, Zeb W.Barber, Tiejun Chang, Mingzhen Tian, Ijaz Zafarullah, Joe A.Fischer, and Wm.Randall Babbitt, "Highly Efficient True-Time Delay Photon Echoes", HBSM'2003, (Jul. 27-31, Bozeman. Montana).

4. R. Reibel*, M. Tian, Z. Barber, J. Fischer and W. R. Babbitt, "Theory and Application of Linear Sideband Chirp Programming", HBSM'2003, (Jul. 27-31, Bozeman. Montana).

5. T. Chang*, M. Tian, Z. W. Barber, and W. R. Babbitt, "Modeling and Simulation of Optical Coherent Transient processes I: Optical Pulse Shaping," HBSM'2003, July 27-31, 2003, Bozeman, Montana.

6. H. Li*, Z. W. Barber, T. Chang, M. Tian, I. Zafarullah, J. A. Fischer, and Wm. R. Babbitt,. , OpTeC'2003, September 19-20, 2003, Bozeman, Montana.

Patents:
None

Honors:
Two of the undergraduates funded under this grant, Zeb Barber and Christoffer Renner, received Goldwater scholarships based on the research they carrier out under the grant.

Transitions:

Many of the techniques developed under this grant are now used in the work at Spectrum Lab at Montana State University and by S2 Corporation of Bozeman. S2 Corporation was spun off from Scientific Materials Corporation and is dedicated to the commercialization of spatial-spectral holographic technology. S2 Corporation is currently funded under a \$15M ASMDC SBIR phase 3 and a SBIR phase 2 from MDA, with sub-contracts to the Spectrum Lab.

The efforts on under this grant, coupled with other work, helped lead to the spatial spectral holographic spectrum analyzer work being carried out at Spectrum Lab under a DARPA phase 3 in collaboration with the Northrop Grumman and the University of Colorado.

Eight (8) MSU SSH patents/patent applications were licensed to Scientific Materials Corporation of Bozeman and subsequently by S2 Corporation of Bozeman. While none of these patents were developed under this grant, the techniques developed under this grant were key in enabling the commercialization of those patents.

6. Appendices

6.1. Appendix A: Final Report on Subcontract to the University of Colorado

The final report on the subcontract to Kelvin Wagner at the University of Colorado is on the following pages.

7. References

[1] R. Reibel, Z. Barber, M. Tian, W.R. Babbitt, "Temporally overlapped linear frequency-chirped pulse programming for true-time-delay applications," Opt. Lett. 27, 494 (2002). R. Reibel, Z. Barber, M. Tian, W.R. Babbitt, "High Bandwidth Spectral Gratings Programmed with Linear Frequency Chirps," J. of Lumin. 98, 355 (2002)

[2] M.Azadeh, C.Sjaarda Cornish, W.R.Babbitt, and L. Tsang, Physical Review A, 57, 4662(1998).

[3] R. Reibel, Z. Barber, M. Tian, W.R. Babbitt, Z. Cole, K.D. Merkel, "Amplification of High Bandwidth Phase Modulated signals at 793nm," J. Opt. Soc. Am. B 19 (2002)

Optical-Coherent-Transisent Time-Delay Control Using Acousto-Optic Distributed Local Oscillators

**A subcontract final report by the University of Colorado to
Montana State University as part of Prof. Randall Babbit's DEPSCoR proposal**
January 17, 2006

Subcontract by :	The University of Colorado
Contact :	Professor Kelvin Wagner
	University of Colorado
	Dept of ECE
	Campus Box 425
	Boulder, Colorado 80309-0425
Phone :	(303)492-4661
FAX :	(303)492-3674
email :	kelvin@optics.colorado.edu
Attention :	Prof. Randall Babbit
	Physics Department
	Montana State University
	Bozeman, MT 59717-3840
	babbitt@physics.montana.edu
	Phone: (406) 994-6156
	Fax: (406) 994-4452

Summary:

For Prof. Randy Babbitt's DEPSCoR program, Prof. Kelvin Wagner's research group at the University of Colorado was subcontracted and tasked with designing and building an acousto-optic (AO) counter-propagating chirp control system for integration with optical coherent transient (OCT) processors being developed at Montana State University. We built an AO sub-system consisting of a pair of high efficiency acousto-optic Bragg cells with counter-propagating chirps applied, such that the diffracted field in an image plane consists of an array of Doppler shifted beams, where the Doppler shift varies linearly in space. Such a system can be used to either control MSU's true-time-delay (TTD) radio-frequency (RF) antenna beamsteering system or to record an optical scanner using chirp frequency shifts by an array of distributed local oscillator (DLO) Doppler shifted beams. For the TTD control system the rate of Doppler shift variation in space was controlled by the chirp rate of the applied chirps. A low bandwidth OCT scanner was also built and tested in an OCT-based time-integrating correlator using only one acousto-optic Bragg cell for the programming of the OCT. This experiment acted as proof-of-concept demonstration, and illustrates that one can in fact record and later read out parallel banks of OCT processors.

1 OCT scanner for Wide-band RF Signal Processing

Spatial-spectral holograms (SSH) have the potential to duplicate the functional operation of acousto-optic (AO) deflectors, but with bandwidths (BW) in excess of 10 GHz and Time-Bandwidth Products (TB) over 10^3 by recording the desired scanning function in an OCT medium. This compares with acousto-optic technology that is limited to bandwidths of 1 GHz and TBs of 1000. Time-domain recording of an impulse and traveling spot, or stabilized frequency-domain recording of a chirped laser and tilting plane wave can be utilized to program an OCT scanner/spectrum analyzer.[1] Although the frequency domain recording approach by Le Gouët is the first concrete demonstration of this type of functionality, it can not be used as a more versatile traveling wave modulator or scanner due to the lack of coherence between the different frequencies. In this project, we built two optical systems to demonstrate the feasiblity of creating a SSH Bragg cell that does preserve the coherence between the various frequencies, thus allowing us to use this SSH Bragg cell in coherent spatial-temporal signal processing applications.

The first optical system was intended as a subsystem for MSU's OCT processor, and involved using two counterpropagating AODs driven with chirps to create a linearly varying set of frequency shifted output spots. These linearly varying frequency shifted output spots could then be used to create linearly varying true-time delay ramps for antenna array processing in OCT media. By varying the rates of the chirps driving the AODs, the range of frequency shifts across the output plane is also varied, allowing such a system to create linearly varying TTD ramps across an antenna, as is required for the broadband beam steering application. This first system was demonstrated independently from any OCT media, but has the characteristics required to implement a broadband TTD beam former in an OCT-based system.

The second optical system also used an acousto-optic deflector to create a scanned optical signal that was recorded in an OCT crystal. The scanner functionality of the AOD was thus transfered to the OCT material, in order to test if such a coupled spatio-temporal SSH could in fact be recorded and read out. Upon reading out the OCT scanner, the diffracted output signal was interfered on a CCD with a correlation reference in order to produce the time-integrated correlation output. This system was built primarily to demonstrate that the parallel channels recorded in the SSH were in fact phase coherent, as would be required in several more sophisticated SSH array processors, such as an antenna array beamformer. Both of these systems and the experimental results are described in the following sections.

2 OCT True-Time-Delay Control using Acousto-Optics

One of the uses of OCT signal processing investigated in this project involves the generation of programmable time delay for True-Time-Delay (TTD) beam forming. The chirp frequency shift technique originally developed by Merkel and Babbitt at MSU[2] is illustrated in Fig. 1, and can be used to record a parallel bank of coherent OCTs in which we control the True-Time Delays. Figure 1 shows the chirp-evolution of the optical signals required to record and read out a TTD spectral grating. The fundamental chirp (produced by a frequency-scanned laser or an electro-optically modulated CW laser), which can cover many GHz and has a chirp rate of b_c (in $\frac{\text{MHz}}{\mu\text{s}}$), is frequency shifted by a small amount, Δf_i, with an acousto optic modulator (shown in the frequency vs. time plot as a downward translation of the fundamental chirp line). This frequency shift results in a time-delay between equal frequency components of the fundamental chirp and the subsequent
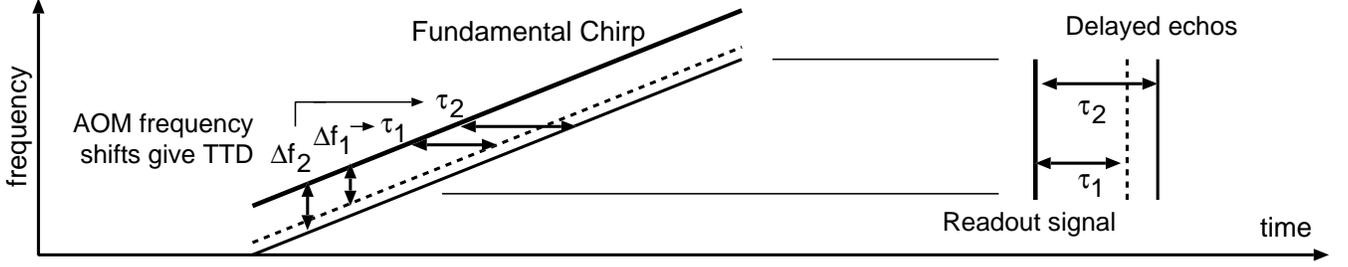
Figure 1: MSU's chirp frequency-shift technique for creating programmable time delay: A portion of a multi-GHz fundamental chirp is frequency shifted by some small amount Δf_i, and interfered in an OCT medium with the fundamental chirp. This interference creates the TTD grating. Any readout signals that fall within the bandwidth of this spectral grating will be time delayed and diffracted, as illustrated by a short readout pulse.

frequency shifted versions. The time delay is given by $\tau_i = -\frac{\Delta f_i}{b_c}$, and for realistic optical chirp rates on the order of 5 $\frac{\text{MHz}}{\mu s}$ and frequency shifts of $0 - 30$ MHz, the resulting time delays could span $0 - 6$ μs. After preparing an SSH with a parallel bank of such time delays, any signal whose bandwidth falls within that of the prepared SSH will be diffracted with the appropriate time delay. If the time-delays are varied linearly across space, such a TTD ramp can then be used in the broadband antenna beamforming application by delaying the signals from the different antenna elements. MSU has successfully demonstrated high bandwidth TTD OCT processing with single channels, so in the first half of this project we investigated only the system that would be used to create the linear ramp of frequency shifted outputs, which could then be incorporated into an actual array processor by MSU.

This effort builds a system to create the necessary array of frequency up- and down-shifted modulated chirps necessary to control the time delay of an entire linear array (see Figs. 2 & 3). To steer such a linear RF array, the linear time-delay ramp imposed on the transmitted beams must be varied, and this is accomplished in the following approach by varying the spatial ramp of a linear array of Dopler up- and downshifts, which are controlled by the applied RF frequency chirps.

The chirp modulation function with chirp rate b_c, center frequency f_0, duration T' and repetition period T is given by

$$s_0(t) \;=\; \sum_n \Pi\left(\frac{t-nT}{T'}\right) e^{i\pi b_c(t-nT)^2} e^{i2\pi f_0(t-nT)} + cc \tag{1}$$

This signal has a bandwidth $B = b_c T'$ which must be as large as the desired antenna beam-steering bandwidth. This is applied to a fiber coupled EO modulator whose exit fiber is placed at position x_0 with a Gaussian beam profile $g(x) = e^{-(x/w)^2}$ for modal width w. A second fiber coupled EO launches a second mode at position $(x, y) = (-x_0, y_0)$ symmetrically offset in x and tilted slightly in y, and is driven by a periodic chirp of twice the chirp rate and half the duration and thus the same bandwidth

$$s_0'(t) \;=\; \sum_n \Pi\left(\frac{t-T_0-nT}{T'/2}\right) e^{i2\pi b_c(t-T_0-nT)^2} e^{i2\pi f_0'(t-T_0-nT)} + cc \tag{2}$$

giving a total input field

$$E(x, y, t) \;=\; g(x-x_0, y)s_0(t) + g(x+x_0, y-y_0)s_0'(t) \tag{3}$$
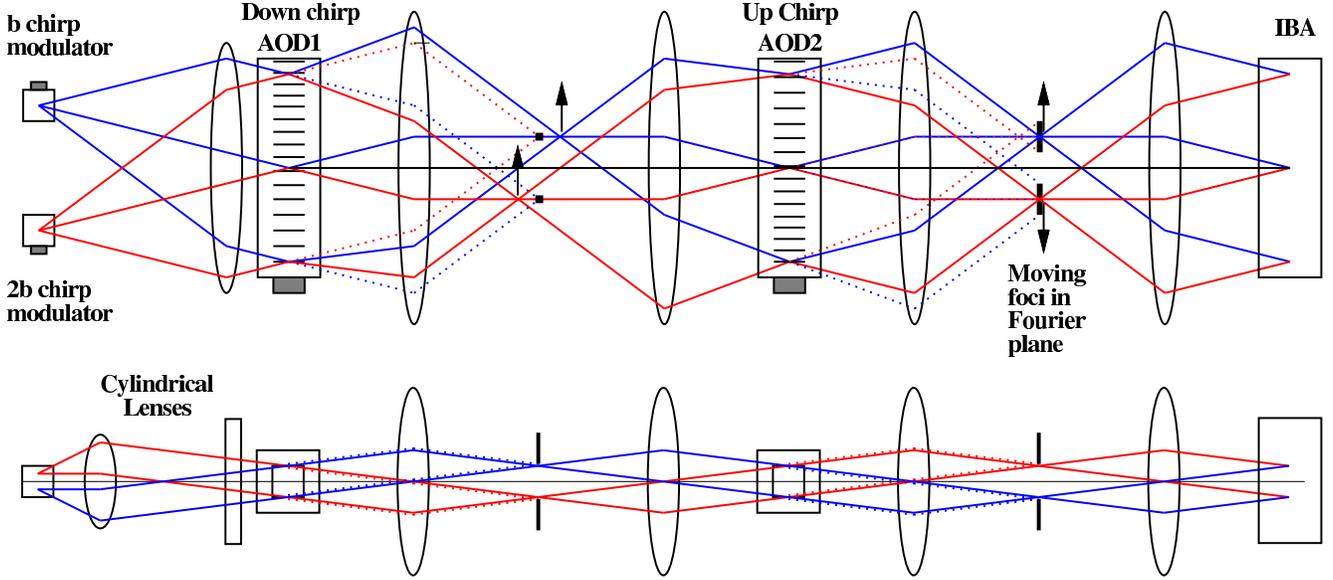
Figure 2: Acousto-optic system for forming up-shifted and down shifted array of chirps with a variable spatial scale factor of the distributed local oscillators. If the chirps are resolvable in the aperture of the AODs, the output plane should have a resolvable frequency ramp across it, which can be used to program an OCT delay ramp for TTD steering of a 1-D phased array.

These two spherical expanding waves are collimated by a Fourier lens with focal length F and incident on the first acoustooptic deflector at the positive and negative Bragg angles.

$$E_{1-}(x,y,t) = G(x/\lambda F)e^{i2\pi x_0 x/\lambda F}s_0(t) + G(x/\lambda F)e^{-i2\pi(x_0 xi - y_0 y)/\lambda F}s_0'(t) \tag{4}$$

The repetitive chirp applied to AOD1 is given by

$$s_1(t) = \sum_n \Pi\left(\frac{t-nT}{T"}\right)e^{-i\pi b(t-nT)^2}e^{i2\pi f_1(t-nT)} + cc \tag{5}$$

This signal is used for frequency shifting and beamsteering, and does not need to be high bandwidth, which allows the use of highly-efficient low-bandwidth acousto-optic devices such as slow shear TeO$_2$. When applied to AOD1 and illuminated by the positive and negative Bragg angle beams, the resulting first order diffraction for a single chirp repetition is given by

$$E_1(x,t) = E_{1-}(x,t)s_1(t-x/v) = G(x/\lambda F)e^{i2\pi x_0 x/\lambda F}s_0(t)\Pi\left(\frac{t-x/v}{T"}\right)e^{i\pi b(t-x/v)^2}e^{i2\pi f_1(t-x/v)} \tag{6}$$

$$+G(x/\lambda F)e^{-i2\pi(x_0 x - y_0 y)/\lambda F}s_0'(t)\Pi\left(\frac{t-x/v}{T"}\right)e^{-i\pi b(t-x/v)^2}e^{-i2\pi f_1(t-x/v)} \tag{7}$$

The diffracted light is Fourier transformed by a lens of focal length F and the undiffracted terms are blocked in the Fourier plane by using the slight vertical shift (y_0) of the two orders. The positive diffracted order of the chirp rate b signal off of the downchirp in AOD1 will yield a mis-focused diffracted beam that will produce a moving focus beyond the Fourier plane. At the same time the chirp rate $2b$ signal incident at the negative Bragg angle produces a Doppler down-shifted focusing diffracted order which will produce a moving focus before the Fourier plane. These contributions

are then re-Fourier transformed by another lens of focal length F producing an inverted image of AOD1 incident on AOD2. AOD2 physically co-propagates with AOD1, but that means the images are counter-propagating, and AOD2 is fed the opposite sign of repetitive chirp

$$s_1(t) \;=\; \sum_n \Pi\left(\frac{t-nT}{T"}\right) e^{i\pi b(t-nT)^2} e^{i2\pi f_2(t-nT)} + cc \tag{8}$$

The field incident on AOD2 consists of two Bragg angle incident terms which are the reverse image of the diffracted orders from AOD1, so that each term is re-diffracted by the counter-propagating reverse chirp. The double diffractions for a single repetition are given by

$$
\begin{aligned}
E_2(x,t) \;=\; & E_{1-}(-x,t)s_1(t+x/v)s_2(t-x/v) = e^{i\pi b(t-x/v)^2} e^{i2\pi f_2(t-x/v)} \\
& \left[G(x/\lambda F)e^{-i2\pi x_0 x/\lambda F} s_0(t)e^{i\pi b(t+x/v)^2} e^{i2\pi f_1(t+x/v)} \right. \\
& \left. + G(x/\lambda F)e^{i2\pi(x_0 x+y_0 y)/\lambda F} s_0'(t)e^{-i\pi b(t+x/v)^2} e^{-i2\pi f_1(t+x/v)} \right] \\
\;=\; & s_0(t)G(x/\lambda F)e^{-i2\pi x_0 x/\lambda F} e^{i2\pi(f_1+f_2)t} e^{i2\pi(f_1-f_2)x/v} e^{i\pi b[t^2-2tx/v+(x/v)^2-t^2-2tx/v-(x/v)^2}} \\
& + s_0'(t)G(x/\lambda F)e^{i2\pi(x_0 x+y_0 y)/\lambda F} e^{-i2\pi(f_1+f_2)t} e^{-i2\pi(f_1-f_2)x/v} e^{-i\pi b[t^2-2tx/v+(x/v)^2-t^2-2tx/v-(x/v)^2]} \\
\;=\; & \Pi\left(\frac{t-nT}{T'}\right) e^{i\pi b_c t^2} e^{i2\pi(f_0+f_1+f_2)t} e^{i2\pi 2btx/v} e^{i2\pi x_0 x/\lambda F} \\
& + \Pi\left(\frac{t-nT}{T'/2}\right) e^{i\pi 2b_c t^2} e^{i2\pi(f_0'-f_1-f_2)t} e^{-i2\pi 2btx/v} e^{-i2\pi(x_0 xi-y_0+y)/\lambda F}
\end{aligned}
\tag{9}
$$

The diffractions from AOD2 are Fourier transformed by a lens with focal length $F"$ and the un-diffracted orders are blocked by using the slight vertical tilts of the two beams and slightly vertically displaced knife edges. The filtered orders are re-transformed back to an image plane of AOD1 and AOD2. The resulting Doppler shift varies as a function of space for the two orders and is given by

$$f_+ = f_0 + f_1 + f_2 - 2bx/v = f_c - 2bx/v \tag{10}$$

and

$$f_- = f_0' - f_1 - f_2 + 2bx/v = f_c + 2bx/v \tag{11}$$

In order to have symmetric frequency offsets for the two spatial Doppler ramps we require $f_c = f_0 + f_1 + f_2 = f_0' - f_1 - f_2$ so that $f_0' - f_0 = 2(f_1 + f_2)$ so for example with $f_1 = f_2 = 80\text{MHz}$ the frequency offset of the two chirp modulators is 320MHz. By varying the chirp rates b for the down and up chirps applied to AOD1 and AOD2 we vary the symmetric spatial Doppler ramps of the multiply diffracted orders. This is exactly what is required for programming the delay using chirp offsets in a photon echo based true-time-delay array control system.

2.1 Experimental demonstration of spatial frequency ramp

Figure 3 shows the layout of the experiment that was performed to verify that we can in fact create the required spatially varying frequency ramps. In this demonstration, the light from a laser is expanded and collimated before illuminating the first of two Bragg cells. The first Bragg cell was driven by an up-chirp from a direct digital synthesis (DDS) frequency sweeper covering the rage from f_0 to $2f_0$, and created the a diffracted, frequency-shifted order through the polarization-swiching acousto-optic interaction in the TeO_2 cell. The zero-th order beam continued straight
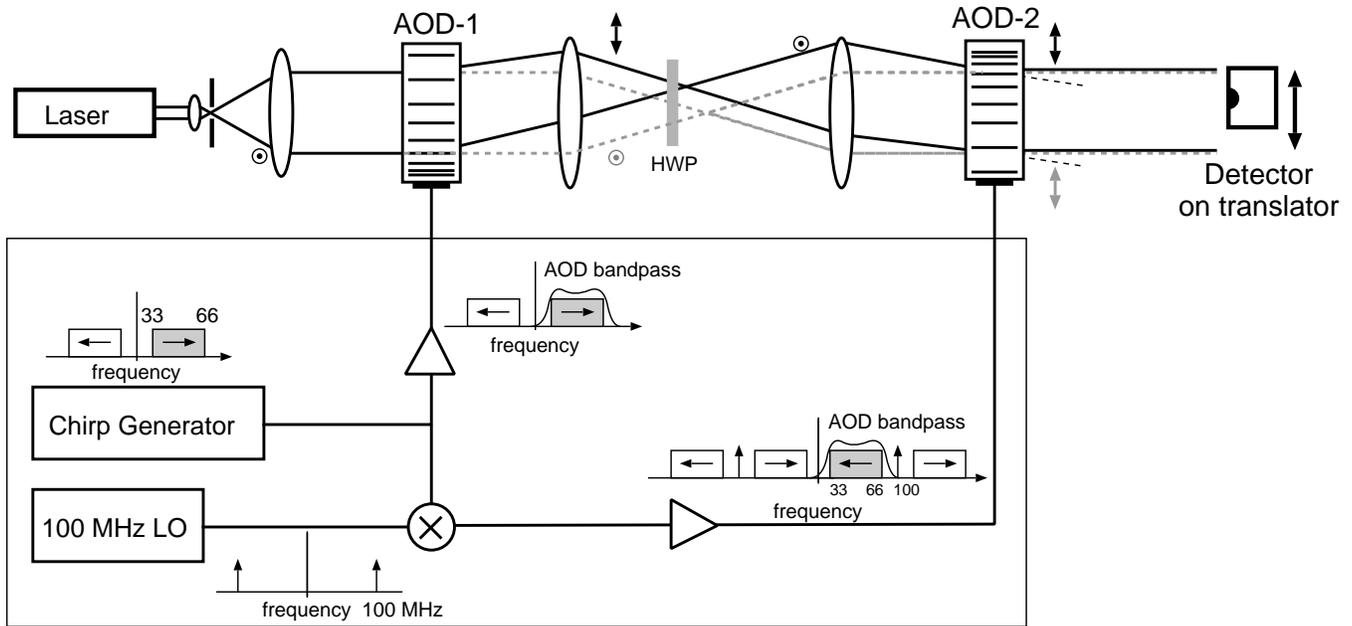
Figure 3: Acousto-optic system for forming up-shifted and down shifted array of chirps with a variable spatial scale factor of the distributed local oscillators. If the chirps are resolvable in the aperture of the AODs, the output plane should have a resolvable frequency ramp across it, which can be used to program an OCT delay ramp for TTD steering of a 1-D phased array.

along the system, and was used downstream as a heterodyne reference. After both the orders from the first Bragg cell were polarization-rotated by 90 degrees by a half-wave plate, the diffracted order was imaged onto a second Bragg cell. The RF signal propagating through this second Bragg cell is a down-chirp covering the same bandwidth as the first, and is produced by mixing the chirp output with a frequency of $3f_0$ and using the negative order which now sweeps from $2f_0$ to f_0. Because the diffraction of this second AOD was also polarization switching, and thus preferentially diffracted the previously diffracted order from AOD 1, the resulting overlapped output of this two-stage AOD system consisted of the undiffracted portion of the laser (consecutive 0-orders) and the doubly-diffracted signals from AOD-1 and AOD-2. When the chirp-rates of the RF chirps were high enough, and the chirps became resolvable across the aperture of the AODs (as indicated in Fig.3), then we would expect a resolvable linear frequency ramp across the outpur plane. Because the zero-th order of both AODs was allowed to pass and was co-aligned and co-polarized with the doubly-diffracted, spatially-varying frequency-shifted beams, we were able to directly measure the heterodyne beat note in the output plane. By translating the output-plane detector we were able to directly measure the frequency shift as it varied across the ouput plane. Figure 4 shows the resulting experimental data. The detector was translated to 6 equally spaced positions (spanning a total of 2.5 mm), and for the chirp durations (ranging from $17 - 170$ μs) the resulting beat note was recorded and its frequency was plotted. The chirps spanned frequencies from $30 - 105$ MHz, and as such had chirp rates ranging from $0.44 - 4.4$ $\frac{\text{MHz}}{\mu\text{s}}$. The output plane exhibited the type of linear frequency ramps that are required to create the TTD ramps for OCT-based broadband beam steering. The greatest complete differential frequency ramp covered 9 MHz, so for the prior example of using a multi-GHz optical programming chirp with a chirp rate of around 5 $\frac{\text{MHz}}{\mu\text{s}}$ (50 GHz in the 10 ms material lifetime) and frequency ramps spanning up to 9 MHz, the resulting time delays could span $0 - 1.8$ μs. With such a time delay, a 540 m diameter antenna array covering

**Output Plane Frequency Shifts for Various Chirp Durations**
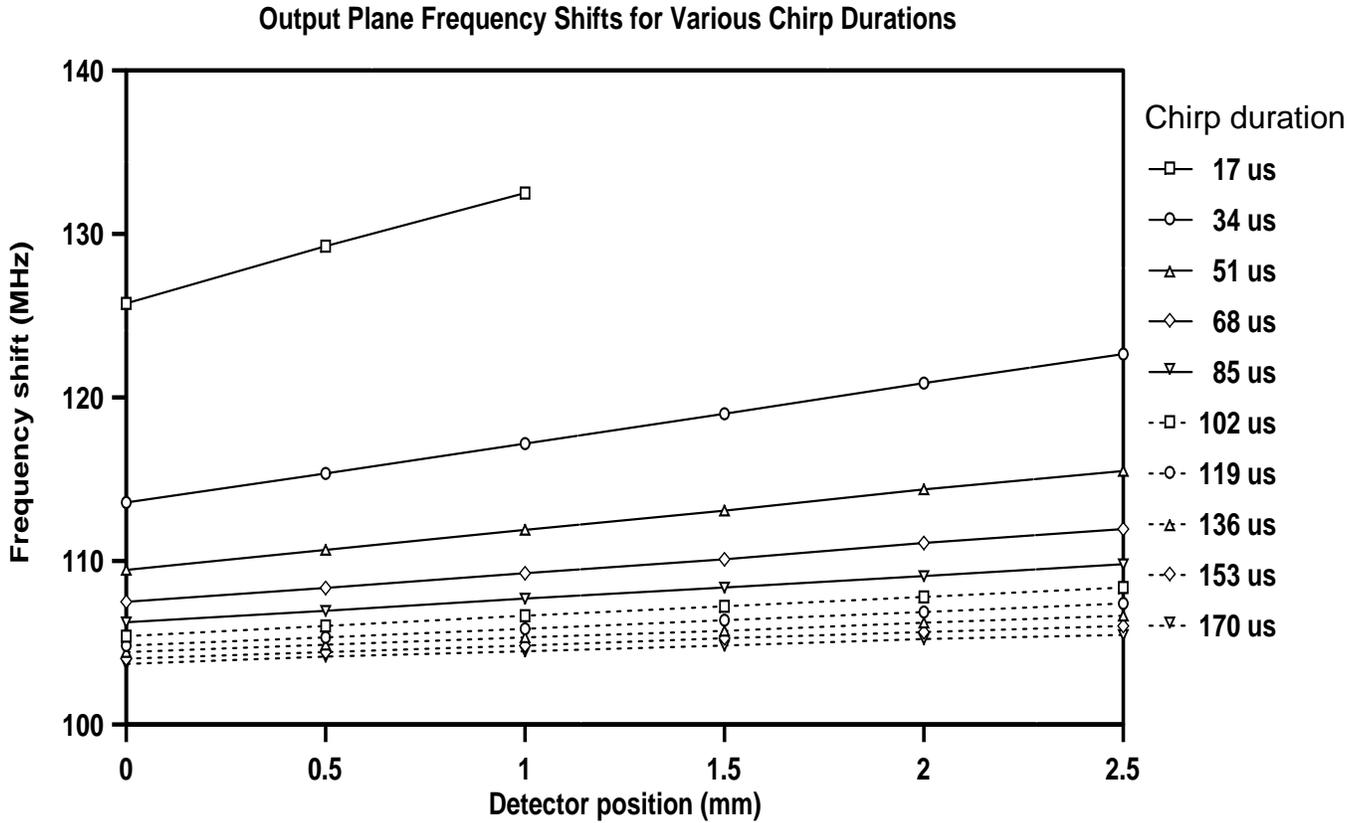
Figure 4: Experimental results from chirped-AOD spectral-frequency-ramp generator. Shown are the measured frequency shifts in various positions of the output plane with increasing chirp duration. Since the chirp bandwidth remains constant, the chirp rate decreases with increasing chirp duration, and results in smaller frequency ramps across the output, as expected.

tens of GHz, could be steered from boresight to endfire!

During the course of this project this acousto-optic systems was not yet combined with a broadband OCT processor, but the next logical step would be to transfer this technology to MSU, and build a full broadband antenna array beamformer. In lieu of building such a beamformer, we decided to build another optical processor that relies of parallel channels of photon echo processing to deliver the desired result. One such processor is a time-integrating correlator, which is explained in the next section. This experiment was beyond the scope of work of the DEPSCoR program, but was nonetheless an ideal demonstration of the spatial parallelism capabilities of SSH processors, so was performed as a synergistic collaboration of this project with a DARPA AOSP project.

3   Time-integrating Correlator

In this section we show how to extend spectrally-integrating time-domain photon-echo processing to a spatio-temporal processing domain in which a modulated optical signal is scanned linearly in space by the diffraction from an appropriately programmed spatial-spectral holographic grating scanner. This one-dimensional scanner performs perhaps the simplest non-separable spatio-temporal diffraction function that allows a demonstration of the spatially parallel and mutually coherent processing capabilities of spatial-spectral holography, and it allows an investigation of the requirements and limitations to programming such a parallel array of photon-echoes. This photon-echo scanner performs a function that is in many ways analogous to an acousto-optic deflector (AOD), in which a temporally modulated RF input $s(t)$ is displayed as a scrolling tapped delay line, $\tilde{s}(t - x/v)$, at an acoustic velocity v. In fact, the spatial-spectral grating used in the experiment to produce the scanned diffraction was recorded by interfering the image of the traveling-wave diffraction from an AOD with a modulated signal produced by an acousto-optic modulator (AOM), where both were driven by the same chirp waveform. The input signal applied to both the AOD and AOM can be considered to be a band-limited impulse for simplicity, but any spectrally uniform signal spanning the full device bandwidth (such as a chirp, pseudo-noise sequence, or broadband random noise) can be utilized as well, with a much higher optical efficiency than the impulse. When this recorded spatial-spectral grating is re-illuminated by a Bragg-matched, temporally modulated optical beam propagating along the direction of the recording beam (or a Bragg degenerate tilted version) then the diffraction will scan just like the output from an AOD at a velocity scaled from the AOD velocity by the magnification of the imaging system. This spatial-temporal holographic reconstruction of the scanning behavior of the AOD is just a generalization of the associative wavefront reconstruction property of conventional spatial holograms when illuminated by one of the exposing spatial fields.[3] In the spatial-spectral holography (SSH) case, the spatio-temporal characteristics of the object AOD are reproduced in the scanned output, including even the non-ideal characteristics associated with the bandshape of the transducer (multiplied by the power spectrum of the recording signal), acoustic diffraction, absorption, and reflections, as well as the frequency-dependent Bragg-matched characteristics of the diffraction (Schaefer-Bergman patterns).[4] However, most slow-shear TeO$_2$ devices, such as the AOD used in these experiments, have such good performance that these deleterious effects can be neglected in a simplified analysis and often in operation as well. Thus, the spatio-temporal diffraction from such a spatial-spectral grating can be considered to be a near identical replica of the imaged diffraction from the AOD, allowing the implementation of similar systems to those originally built using AODs.

A related approach has been used by Le Gouët et al[5–7] to implement a power spectrum analyzer by Fourier transforming with a lens the diffracted output of the spatial-spectral holographic scanner and placing an integrating photo-diode array in the Fourier plane, in exact analogy to the acousto-optic spectrum analyzer.[8] Their system can instead be thought of as a frequency-multiplexed set of spectrally-selective diffraction gratings with diffraction angle proportional to offset RF frequency from the carrier. In their case of power spectrum analysis the relative phases of the different frequency components diffracted from the SSH are of course unimportant, since each is individually mod-square detected by the detector array at the Fourier plane where they are separated. Therein lies the key difference to the experiment discussed here, since the time-integrating correlator requires phase coherence between all of the spectrall channels.

In this experiment we demonstrated that an appropriately programmed SSH does indeed faithfully reproduce the fully coherent scanning behavior of the AOD. However, to demonstrate directly

that this spatial-spectral holographic scanner does holographically duplicate the scanning function-
ality of the object AOD in its entirety would require an interferometric, GHz-frame-rate coherent
field imager. Since such a device does not exist, so instead an interferometric time-integrating
correlator was used, since such a system fundamentally requires phase-locked coherence between
the diffractions of different frequency components originating from different spatial locations in the
SSH. This implicit demonstration proves that the SSH scanner does indeed faithfully reproduce
the scanning behavior of the AOD. While this particular implementation of scanner recording and
readout is also bandwidth limited by the acousto optics used, a future goal might be to circumvent
these limitations by performing the spatial and spectral scans independently, and over much greater
bandwidths. For example, it is possible to combine the spatial scanning of an AOD with the high
bandwidth spectral scans of a chirped laser or an electro-optically modulated laser to record a high
bandwidth scanner. This, however will be a topic for future study. Before explaining the details
of the current experiment, we first discuss the theory of the scanner, as well as an acousto optic
implementation of a time integrating correlator.

3.1   Scanner Theory

A pair of spatio-temporal fields, $E_j(\vec{r}, t)$, where $j = 1, 2$, incident on a cryogenically-cooled, inho-
mogeneously broadened absorber (IBA) medium will engrave a spatial-spectral holographic grating
in the atomic ground-state (and also possibly the excited-state) population distribution which will
holographically modulate the dielectric properties in both space and frequency. The propagation
of the fields into the volume of the IBA crystal is most easily represented in terms of the spatio-
temporal Fourier transforms of these fields incident at the planar IBA material boundary, $z = 0$,
$\mathcal{F}_{\vec{x}, t}\{E_j(\vec{x}, t)\} = \mathcal{E}_j(\vec{k}_T, \omega)$, where $\vec{x} = (x, y)$, $\vec{k}_T = (k_x, k_y)$, and $\mathcal{F}$ is the operator representing
Fourier transformation with respect to the subscript variables. Propagation and interference can be
represented in terms of the Fresnel diffraction operator[9] represented as a phase advancement of the
transverse spatial Fourier components throughout the volume of the crystal of index n (assumed
isotropic for simplicity),

$$E(\vec{r}, \omega) = \mathcal{D}_z\{E(\vec{x}, t)\} \equiv \mathcal{F}_{\vec{k}_T}^{-1}\left\{\mathcal{E}(\vec{k}_T, \omega)e^{-i(\omega t - z\sqrt{(\omega n/c)^2 - k_T^2})}\right\}, \tag{12}$$

where $\vec{r} = (x, y, z)$, z measures the depth of propagation into the crystal, and $\mathcal{F}^{-1}$ is the inverse
Fourier transform operator. Two spatio-temporally modulated beams that propagate into the IBA
crystal will interfere locally (in $\vec{r}$ and ω) and the term responsible for the stimulated photon echo
goes as $E_1^*(\vec{r}, \omega)E_2(\vec{r}, \omega)$. The accumulation of the spectral grating, G, leads to a spatial-spectral
hologram at time t_0 throughout the crystal volume which is blurred out by convolution with a
Lorentzian, $l(\omega)$, of line width $1/T_2$, as given by

$$G(\vec{r}, \omega', t_0) = \int \frac{e^{i\omega t_0}T_2}{1 - i(\omega - \omega')T_2}E_1^*(\vec{r}, \omega)E_2(\vec{r}, \omega)d\omega. \tag{13}$$

The readout of this spatial-spectral grating occurs when a third field propagates into the IBA,
locally multiplies by G, and then the diffracted component propagates to the output face. Diffracted
contributions throughout the crystal thickness L and the IBA material inhomogeneous lineshape,
$g(\omega)$, need to be integrated, giving

$$E_d(\vec{x}, t) = \int_0^L dz \int d\omega e^{i\omega t} g(\omega) \mathcal{D}_{L-z}\{\mathcal{D}_z\{E_3(\vec{x}, \omega)\}G(\vec{r}, \omega, t_0)\}$$

$$= \int_0^L dz \int d\omega g(\omega) e^{i\omega t}$$
$$\mathcal{D}_{L-z}\left\{\mathcal{D}_z\{E_3(\vec{x},\omega)\}\left[\left[\mathcal{D}_z\{E_1(\vec{x},\omega)\}\right]^* \mathcal{D}_z\{E_2(\vec{x},\omega)\}\right] * l(\omega)\right\} * l(\omega). \tag{14}$$

When the spatial characteristics of E_3 appropriately match E_1 (generalized Bragg matching[10]) and the temporal characteristics of E_1 match E_2 except for a delay (eg linear phase factor in the spectral domain), then the spatial propagation operators holographically cancel and the full spatio-temporal characteristics of field $E_2(\vec{x},\omega)$ resolvable with the coherence-time line-shape spectral blurring are coherently stored in the SSH, and available for Bragg-matched readout by E_3.

An acousto-optic deflector illuminated by a Bragg-matched Gaussian beam produces a diffracted beam for an applied signal $s(t)$ that can be represented either in the time domain as a traveling wave, or in the frequency domain as Doppler-shifted plane waves propagating at an angle proportional to their frequency,

$$\begin{aligned} E_2(x,y,t) &= e^{-i(\omega_0 t - \vec{k}_0 \cdot \vec{x})} p_\Omega(x) q(y) s(t-x/v) \\ &= e^{-i(\omega_0 t - \vec{k}_0 \cdot \vec{x})} \int_{-\infty}^0 S(\Omega) T_\Omega(x,y) e^{i\Omega t} d\Omega. \end{aligned} \tag{15}$$

Where Ω is the RF angular frequency which is only integrated over a single sideband, and the window function of the illuminated AOD is

$$p_\Omega(x)q(y) = \left[\Pi\left(\frac{x}{X}-.5\right)e^{-[(x-x_0)/a_x]^2}e^{-\alpha_0 x(\Omega/2\pi)^2}\right]\left[\Pi\left(\frac{y}{Y}\right)e^{-(y/a_y)^2}\right], \tag{16}$$

where Π is a unit width rectangle function, the device width is X, height is Y, and the elliptical Gaussian beam width is a_x by a_y, centered at x_0 (with respect to the transducer at $x=0$), and the acoustic attenuation is quadratically frequency dependent. The corresponding Fourier response function is $P_\Omega(k_x)Q(k_y) = \mathcal{F}\{p_\Omega(x)q(y)\}$. For a more complete description of AOD behavior the frequency dependent transmission response T_Ω can be used,[4] which represents the frequency-dependent Bragg-matched acoustic diffraction,

$$T_\Omega(x,y) = H(\Omega)B(\Omega)\mathcal{F}_{\vec{k}_T}^{-1}\left\{\delta(k_x - \Omega/v + b_y k_y^2) * P_\Omega(k_x)\right\}Q(k_y) \tag{17}$$

$H(\Omega)$ represents the transducer electro-acoustic bandwidth (typically tuned over 1 octave), and $B(\Omega) = \text{sinc}(\Delta k L/2)$ is the acousto-optic Bragg matched bandwidth with the details of the frequency dependence of $\Delta k(\Omega)$ depending on the device design and is typically parabolic for birefringent or phase-array devices. For the ideal traveling-wave scanner model the out of the plane acoustic curvature b_y is set to zero, so the delta-function Fourier transforms to $e^{-i\Omega x/v}$, and the image of the AOD on the IBA crystal is

$$E_2(x,y,t) = e^{-i(\omega_0 t - M\vec{k}_0 \cdot \vec{x})}Q\left(\frac{y}{\lambda F_y}\right)p\left(\frac{x}{M}\right)\int_{-\infty}^0 S(\Omega)H(\Omega)B(\Omega)e^{i\Omega(t-\frac{x}{v_M})}d\Omega. \tag{18}$$

This diffracted AOD field is imaged onto the SSH crystal with magnification M in the x dimension (so $v_M = v/M$) and focused in the y dimension with a cylinder (F_y) to a line focus of width $a_2 = \lambda F_y/a_y$.

The temporally-modulated and tilted reference wave from the AOM (with wave-vector $\vec{k}_r$) has a spatial profile designed to maximally overlap with the AOD object wave

$$E_1(x,y,t) = e^{-i(\omega_0 t - \vec{k}_r \cdot \vec{x})}e^{-[(x-x_0/M)/(a_x/M)]^2}e^{-(y/a_2)^2}\tilde{s}(t) \tag{19}$$

where $\tilde{s}(t)$ is the single-sideband temporal-modulation signal, which occurs before the acoustic waves in the AOD propagate into the deflector aperture. This ensures that the signal from the AOM acts as pulse one of a three pulse photon-echo sequence, whereas the signals from the AOD act as a bank of second pulses. This is vital to ensure that causality is observed, since the echo that will be produce can not occur before the readout pulse. After recording the SSH scanner, the readout field is generated by a different temporally modulated waveform, which can cover up to the bandwidth of the scanner recorded in the material (given by the product $|S(\Omega)|^2 H(\Omega)B(\Omega)$) and with a possible Bragg degenerate tilt $(\vec{k}_d \cdot (\vec{k}_r - \vec{k}_0) = 0)$,

$$E_3(x,y,t) = e^{-i(\omega_0 t - (\vec{k}_r + \vec{k}_d)\cdot\vec{x})} e^{-[(x-x_0/M)/(a_x/M)]^2} e^{-(y/a_2)^2} \tilde{r}(t) \tag{20}$$

Which yields an output from the SSH given by

$$\begin{aligned}
E_d(x,y,t) &= e^{-i(\omega_0 t - (M\vec{k}_0 + \vec{k}_d)\cdot\vec{x})}[e^{-[(x-x_0/M)/(a_x/M)]^2} e^{-(y/a_2)^2}]^2 \\
&\quad \mathcal{F}^{-1}_{\vec{k}_T}\left\{ q(k_y \lambda F_y) \int_{-\infty}^{0} R(\Omega)|S(\Omega)|^2 H(\Omega)B(\Omega)e^{i\Omega t} P_\Omega(Mk_x - \Omega/2\pi v)d\Omega \right\} \\
&\approx e^{-i(\omega_0 t - (M\vec{k}_0 + \vec{k}_d)\cdot\vec{x})} L\left(\frac{x}{v_M}\right) p\left(\frac{x}{M}\right) Q\left(\frac{y}{\lambda F_y}\right) \\
&\quad \times \left[e^{-[(x-\frac{x_0}{M})/(\frac{a_x}{M})]^2} e^{-(\frac{y}{a_2})^2} \right]^2 \tilde{r}\left(t - \frac{x}{v_M}\right)
\end{aligned} \tag{21}$$

where $L(x/v_M) = e^{\frac{-x/v_M}{2T_2}}$ is the exponential coherence loss scaled into space by the magnified acoustic velocity, $v_M = v/M$. This shows that when the recording signal power spectrum $|S(\Omega)|^2$ is flat over the device bandwidths spanned by $H(\Omega)B(\Omega)$ (corresponding to recording with an impulse, chirp, or white noise) that the diffracted field from the SSH scanner duplicates the full spatio-temporal characteristics of the AOD scanner as long as the coherence lifetime exceeds the phonon lifetime and time delay in the illuminated portion of the AOD. If desired, an additional tilt, $\vec{k}_d$, can be added to the diffracted field to allow simple spatial filtering to separate the diffraction from the writing beams.

3.2 Acousto-optic time-integrating correlator (TIC)

Since this low bandwidth SSH TIC demo is based on copying the operation of an AOD into an SSH, and then using the SSH scanner in the topology of a classic interferometric acousto-optic time-integrating correlator,[11, 12] the implementation of this type of AO-based processor will be described first. As seen in Fig. 5, the diffracted field from a slow-shear wave TeO$_2$ AOD (in which $v = .62$mm/μsec) is imaged onto a 1-dimensional CCD detector array via a 4-F imaging system with a DC block in the Fourier plane (this is also known as Schlieren imaging). This traveling-wave modulation is interferometrically combined with an off-axis modulated plane wave reference signal produced by the collimated diffracted field from an AOM. An RF signal, $s(t)$, is applied to the AOD and diffracts the Bragg-matched incident plane wave with a scrolling time-delay modulation that is characteristic of AODs. The single-sideband (SSB) diffracted signal, $\tilde{s}(t - \frac{x}{v})$, is imaged onto the CCD, where it is interfered with a SSB temporally-modulated reference signal, $\tilde{r}(t)$, from the reference AOM. In radar applications that use time integrating correlators, both the transmit and reference signal are identical broadband high time-bandwidth (TB) signals, such as a broadband chirp or noise-like waveform, with a reference delay τ_d, $\tilde{r}(t) = \tilde{s}(t - \tau_d)$. The radar
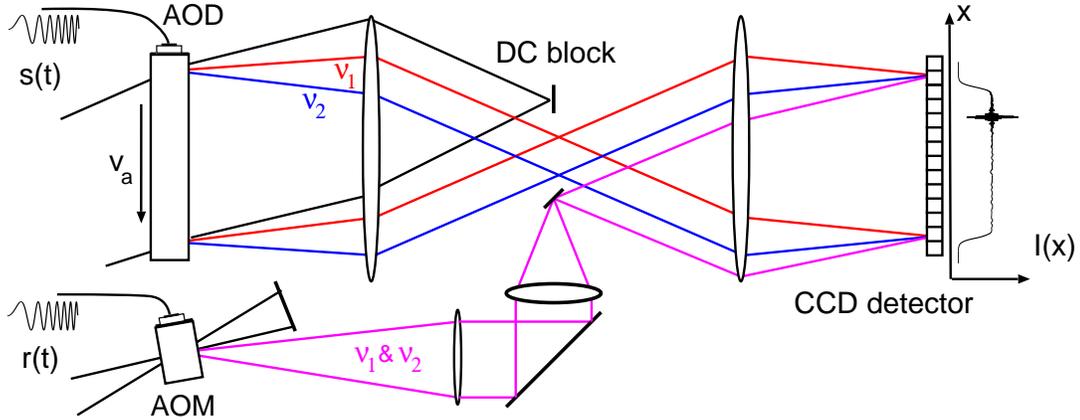
Figure 5: Additive interferometric acousto-optic time-integrating correlator. The traveling-wave spatio-temporal diffraction from the AOD is imaged onto the CCD detector array where it interferes with an off-axis temporally modulated signal diffracted by the AOM. The time-integrated correlation peak appears at a spatial position proportional to the relative delay between the two signals on a high frequency spatial carrier that allows the demodulation of the correlation signal from the bias and coherent artifacts.

return consists of a complex linear superposition of delayed copies of the reference plus uncorrelated noise, $s(t) = \sum_m |a_m| e^{i\phi_m} s(t - \tau_m) + n(t)$ and is correlated with the local, time-delayed copy of the transmit signal. By by measuring the position of the correlation peak, one can infer the range delay information of the target. A correlator is then the optimal linear detector to measure the delays $\tau_m - \tau_d$, amplitudes a_m, and phases ϕ_m, as the positions, amplitudes, and phases of the carrier of each correlation peak on the detection CCD. The fringe pattern caused by the interference of the two described signals is given by

$$
\begin{aligned}
I(x) &= \int_0^T \left| r(t) e^{i2\pi u_0 x} + s(t - x/v) \right|^2 dt \\
&= \mathcal{R} \left\{ e^{i2\pi u_0 x} \int_0^T r^*(t) s(t - \frac{x}{v}) dt \right\} + \text{bias},
\end{aligned}
\tag{22}
$$

where u_0 is the spatial frequency of the tilted reference wave, and $\mathcal{R}$ represents the real part. The temporal integral over the time window T is due to the accumulation of photo-generated charge within each CCD pixel, which can readily integrate over a time approaching .1-1 second at room temperature, and with a cooled CCD, integration can be extended to many minutes. The intensity distribution on the CCD is thus the correlation of $s(t)$ and $r(t)$ riding on a spatial carrier, as well as background terms, as illustrated graphically in Fig. 5. For matched signals with bandwidth B, the correlation peak is a sharp spike whose shape is the Fourier transform of the signal power spectrum with spatial width on the CCD $\sigma = B v_M$, for magnification M, and it is modulated by a carrier spatial frequency $u_0 > 1.5/\sigma$. Therefore, the CCD pixel spacing, Δ_x, must be fine enough to ensure adequate Nyquist sampling of the carrier and correlation, $\Delta_x < 1/2u_0 + 1/\sigma$. The correlation peak is produced at a CCD position $x = \tau_d v_M$, where τ_d is the relative time-delay. The goal of this experiment is to successfully replace the AOD with an SSH that is appropriately programmed to duplicate the traveling-wave scrolling delay line function.

In order to record the spatio-temporal characteristics of the acousto-optic deflector into the SSH in a coherent fashion, we built the system shown in Fig. 6. A broadband RF signal, $s(t)$,
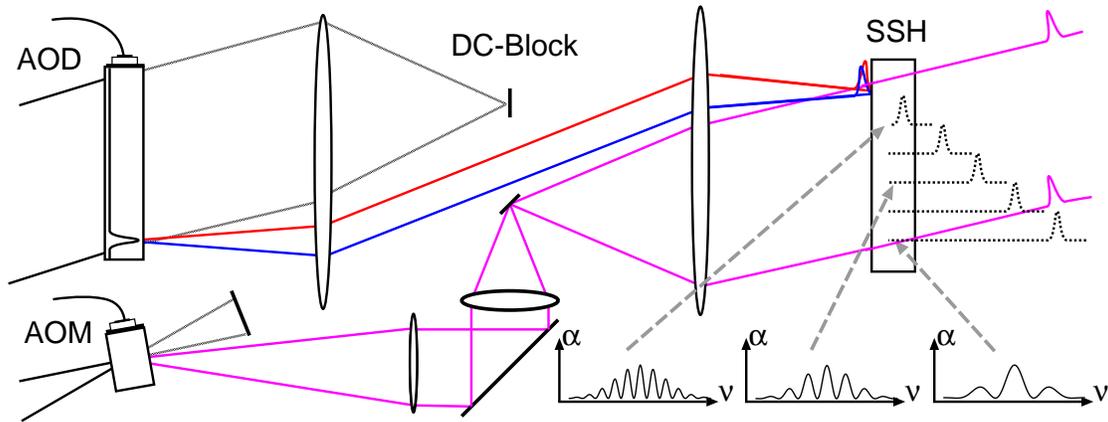
Figure 6: Recording a spatial-spectral holographic deflector: An RF pulse injected into the AOM gives a diffracted optical pulse that acts as reference pulse which is collimated to illuminate the entire SSH at an angle. The same RF pulse launches an acoustic pulse that travels through the AOD producing a diffraction that is imaged onto the SSH with linearly increasing time delays. The interference between these beams produces a spatial-spectral grating, that encodes the time delay as the periodicity of the spectral modulation which increases linearly across the crystal.

was injected simultaneously into the AOD and the AOM (a pulse is illustrated and described in the text, but chirps were used in the experiments since they have greater power efficiency). The diffracted light from the AOM was collimated and projected on the entire crystal immediately, and acted as pulse one of the 3-pulse photon echo sequence. The spatio-temporal diffraction from the AOD was telescopically imaged with a Schlieren filter onto the SSH and acted as pulse two. Note, that the temporal separation of these two pulses varied linearly in space, because of the scrolling time-delay diffraction from the AOD. Using this approach, time delays of up to the coherence time of the Tm^{3+}:YAG can be recorded in the SSH. Once the SSH was prepared, the readout process by a new signal, $r(t)$, was relatively straight-forward. This modulated signal, generated by the programming/readout AOM, and whose bandwidth fell within that of the prepared SSH scanner, now acted as pulse three of the photon-echo sequence and diffracted off the SSH in both space and time. This produced a scanned diffracted field that holographically recreated the field that would have diffracted off the AOD had the electrical signal $r(t)$ been applied to the transducer of the programming AOD.

As a first test to verify that the SSH was in fact operating as a scanner, we reproduced some of the earlier spectrum analysis experiments that our collaborators in France performed. In this experiment, a lens was used to spatially Fourier transform the scanner's output, and project the resulting Fourier plane onto a CCD camera. Any subsequent signal (whose bandwidth lay within that of the SSH's) that read out the SSH was Fourier transformed onto the CCD, thus mapping the time-domain signal into a spatial representation of its spectrum. The setup used for this experiment is shown in Fig. 7. When this experiment was performed, the tapered amplifier had not been built, so it was severely power limited. By programming and reading out only a small number of spectral bins, we were still able to recover the spectrum of an interesting signal. The SSH was programmed with the system illustrated in Fig. 6 and read out using a 1 MHz square wave riding on a 70 MHz carrier. The signal detected on the CCD was corrected for irregularities due to the AO bandshapes, and can be seen in Fig. 8. The spectrum clearly shows the 1st and 3rd harmonics of the 1 MHz
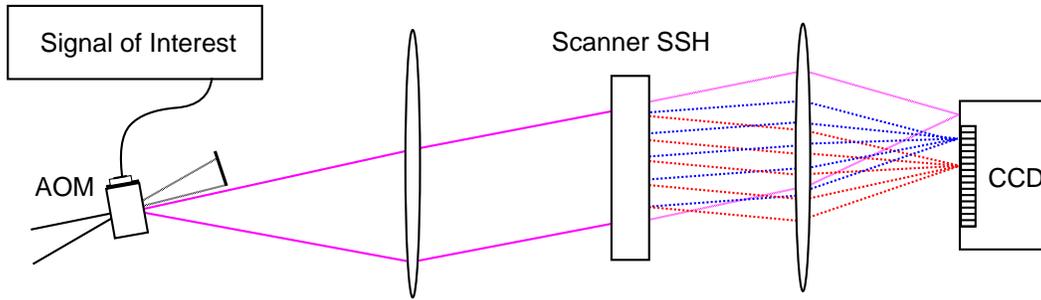
Figure 7: Spectrum analyzer using frequency-to-angle mapping in an SSH. An SSH programmmed with a scanner functionality is read out with an RF modulated optical carrier. Optical frequencies which fall within the SSH's bandwidth are diffracted at particular angles, which, when Fourier transformed with a lens, result in the spectrum of the RF signal on the CCD.
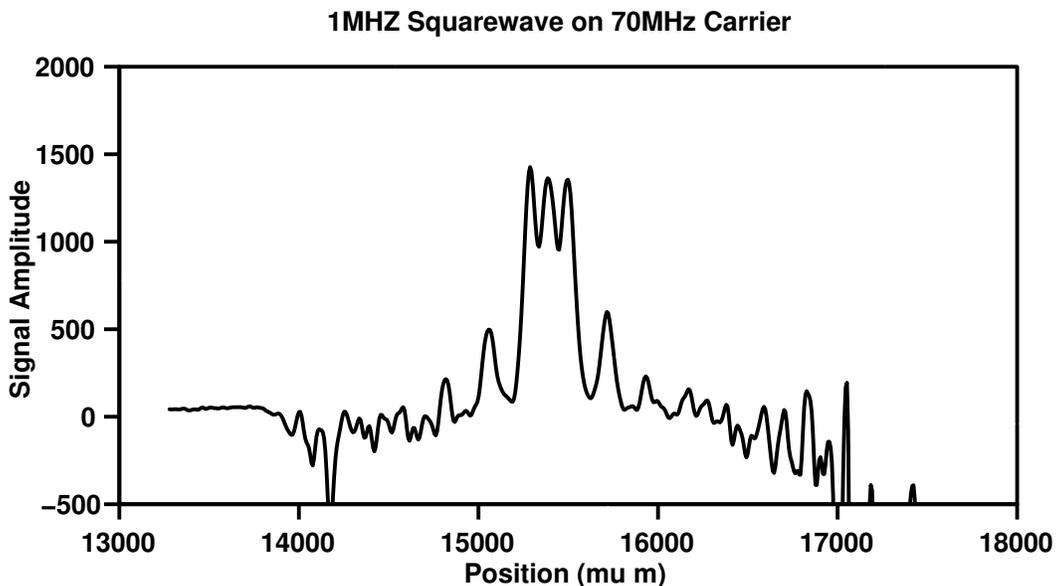

Figure 8: Spectrum analysis result using the spatial SSH spectrum analyzer. After programming an SSH as a scanner, it was read out by and AOM which was driven by a 1 MHz square wave on a 70 MHz RF carrier. The plot shows the CCD signal after it was corrected for AO bandshape effects. The spectrum clearly shows the carrier and 1st and 3rd harmonics.

square wave, and the fifth harmonic appears to be barely above the noise floor, so this system had a SNR of about 13 – 15 dB. This experiment was, however, just a stepping stone on the way to building the SSH time-integrating correlator.

By building a time-integrating correlator (TIC) around the recorded scanner SSH, we could verify whether or not the recording and readout processes were indeed spatially coherent, since the TIC could only operate properly if the detailed phase relationships between each of the angular and frequency components diffracted by the SSH were preserved to duplicate those produced by the AOD. If, and only if, the SSH offered a fully coherent replacement for the AOD could the SSH TIC give a correlation peak.
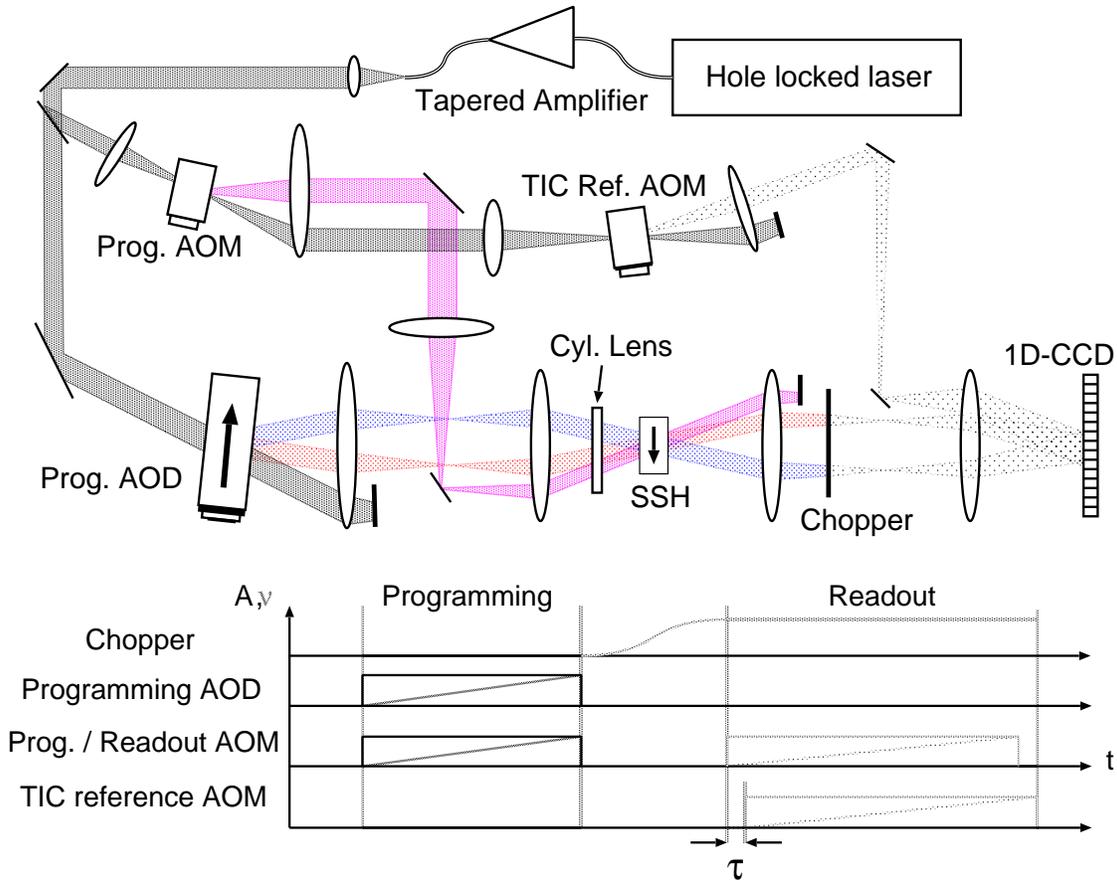
Figure 9: Experimental setup for programming of the spatial-spectral holographic scanner for operation in a time-integrating correlator and the signal and chopper timing diagram. The programming AOD was imaged onto the SSH in x and focused in y to a line illuminating the SSH where it interfered with a tilted and collimated temporally-modulated signal from the programming AOM. Repetitive application of the same chirp signals (or any broad-band signal) to the AOD and AOM accumulated up an efficient SSH scanner. During the recording phase of the SSH the readout CCD was blocked by the chopper.

3.3 Spatial-Spectral Holographic Time-Integrating Correlator Experiment

The experimental setup of the SSH TIC is shown in Figs 9 and 10, and illustrate the recording phase for the SSH scanner and readout/TIC phases respectively. The 7 mW output from hole-locked Velocity laser was injected into a tapered amplifier system, resulting in 140 mW of narrow linewidth optical radiation at 793 nm. This relatively high power was needed because hundreds of parallel photon-echo channels were recorded in a relatively large area of the 0.1% doped Tm^{3+}:YAG crystal. The total illuminated beam area for the TIC measured 2.6 mm wide by 50 μm tall, rather than the typical 30 – 100 μm diameter Gaussian beam typically used for 1-D photon-echo experiments and spectral-integrating correlators. The crystal area illuminated was thus nearly 200 times larger, so in addition we accumulated the scanner by recording multiple exposure sequences.

To determine the appropriate amount of accumulation in this geometry, we performed a simple
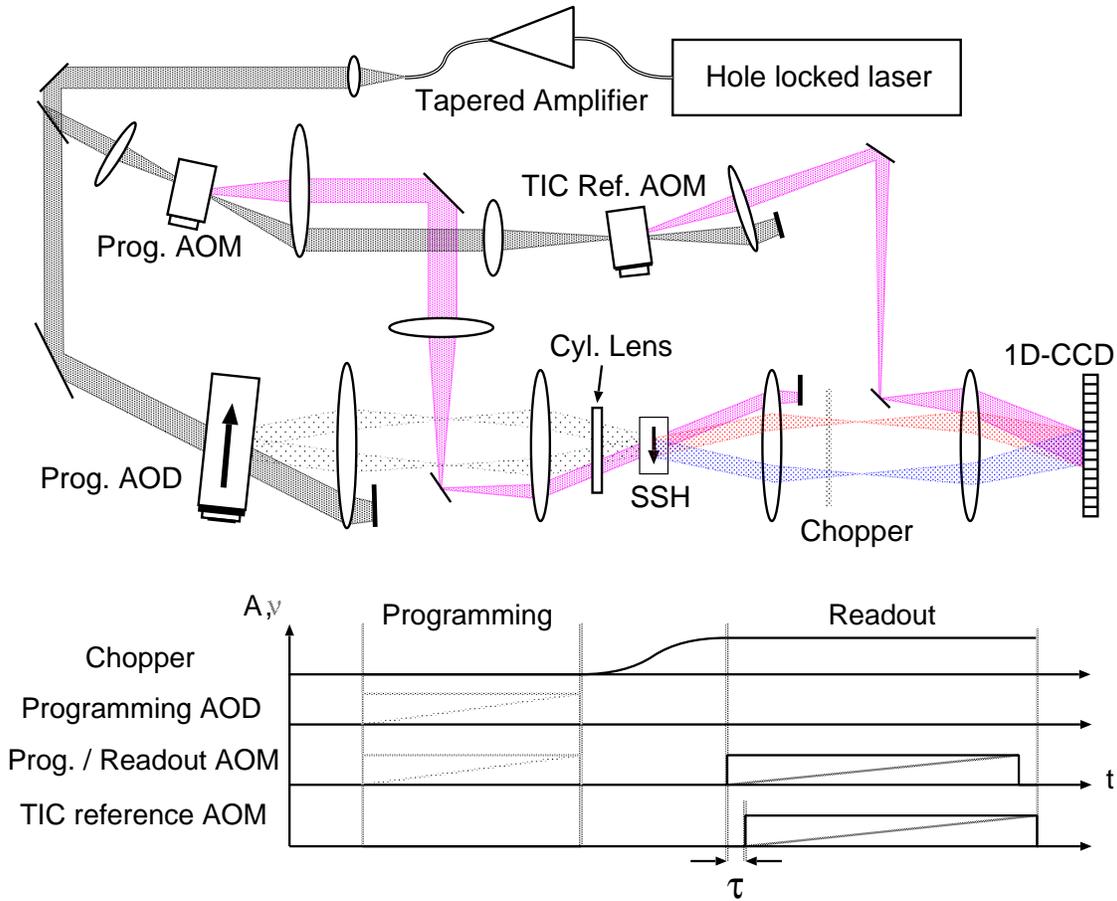
Figure 10: During the readout phase of the time-integrating correlation, the AOD was turned off, the programming AOM was driven by the correlation waveform which illuminated the SSH to produce a linearly scanned diffraction which passed through the open chopper and was imaged onto the CCD. At the same time the reference waveform (which is the same chirp driving the readout AOM but delayed by τ) drove the TIC reference AOM, and the modulated diffracted beam was collimated and illuminated the CCD at a tilted angle. The photo-generated charge produced by these beams interfering in each pixel was time-integrated to produce the correlation fringes.

1-D photon echo experiment using 30 MHz bandwidth temporally overlapping linear frequency chirps (TOLFC)[13] spread out spatially to cover a 6 mm × 50 μm area. This was a larger area than the final experiment utilized, because at the time we were using an optical system with a different magnification than in the final SSH-TIC experiment. After a sequence of accumulated exposures, we measured the echo strength, as shown in Fig. 11. Previous studies,[?,14] indicate that accumulation requires excellent laser stability, ideally well under 10 kHz. Stabilized accumulation should result in a quadratic increase of photon echo intensity peak size with number of accumulated programming sequences, eventually rolling off when the IBA approaches saturation. Without hole-locking, the free-running external-cavity diode laser (ECDL) linewidth degraded to greater than 100 kHz, and although single shot echoes were easily produced, accumulation of multiple engraving sequences quickly washed out the spectral grating, resulting in smaller echoes. Since we did see a quadratic increase in echo size for the first $2-5$ pulses, followed by a regime where the echo efficiency increased
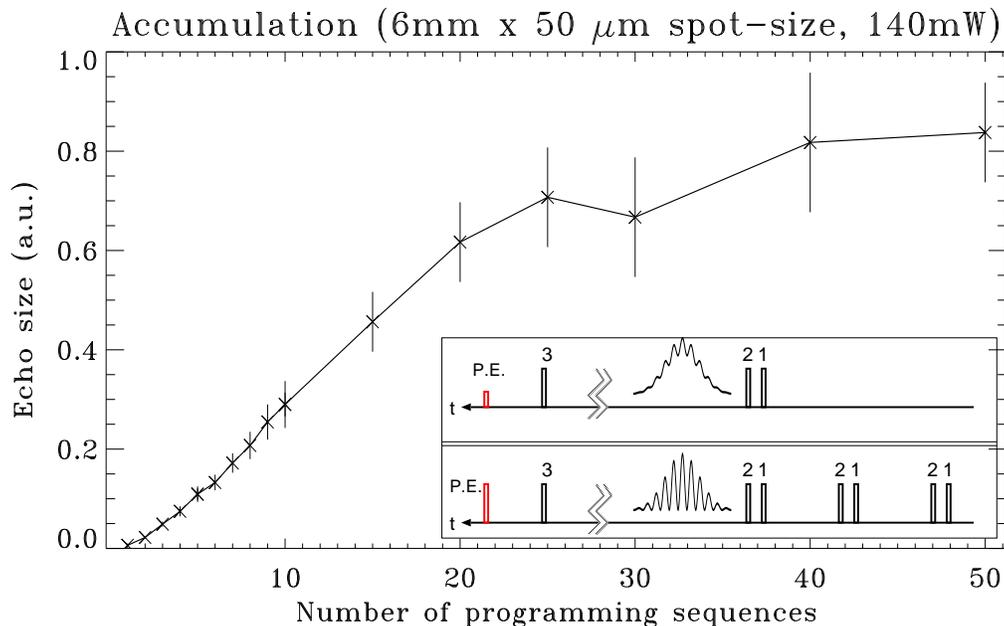
Figure 11: Accumulation results in SSH time-integrating correlator. By applying the same TOLFC pulse sequence a number of times, the accumulation process was optimized for the beam size and geometry specific to this experiment.

linearly and then saturated after $20 - 25$ cycles, we estimate that laser linewidth may not be as good as 10 kHz, but certainly was much better than 100 kHz. Thus, when recording the SSH scanner we typically accumulated for 25 repetitions, and then switched to a readout mode that lasted for the duration of the bottleneck lifetime in Thulium of $T_B = 10$ ms. Alternatively, a continuous mode could be used in which, as the chopper rotates, exposure cycles are alternated with readout cycles during which the diffractions from the SSH scanner created time-integrated correlations, and the CCD detector array was able to integrate for 0.1 seconds on chip, and even longer after analog-to-digital conversion using digital averaging. Such long coherent integration is important because it enhances the processing gain, $\text{PG} = \text{SNR}_{\text{out}}/\text{SNR}_{\text{in}}$, which is the ratio of output signal-to-noise ratio (SNR) to input SNR, and is ideally given by the product of the processing bandwidth, B, and the integration time, T, (divided by the duty factor for such an interleaved correlation). This is to be contrasted with incoherently averaging a sequence of photon-echo correlation peaks from a conventional spectrally integrating correlator (for example using averaging on an oscilloscope), which results in an increase of SNR that only increases with the square root of the number of averages. A single long continuous exposure could be used with a never ending random-noise waveform applied to both AOD and AOM, but then an angularly multiplexed (in the direction of Bragg degeneracy) readout scheme would need to be employed. Since the recording light scattered from the crystal, the uncoated windows of the cryostat, and other components in the experiment onto the CCD, we instead used a chopper to time-multiplex the recording and SSH read-out to produce the TIC. After careful alignment of spatial filters in various Fourier and image planes before and after the crystal the scatter produced by the readout beam was low enough to detect the TIC fringes. We took further measures to guard the CCD from external light, including building

an opaque plexiglass box with light baffels around the CCD. Even with all those measures in place, we still had to turn off the room lights, and shield light from surrounding monitors, oscilloscopes, etc, because the long-term integration on the CCD was extremely sensitive to stray light. This experiment would have greatly benefited from the antireflection coated windows, since these would have greatly reduced the amount of stray light.

In the first phase of the experiment, shown in Fig. 9, the SSH is programmed with the scrolling time-delay functionality of a Bragg cell by injecting a 50 μs chirp spanning 60 to 90 MHz into a slow-shear wave AOD and imaging the 30 mW of diffracted output onto the SSH. At the same time, an identical chirp is injected into an AOM, whose diffracted output (40 mW) is anamorphically expanded, overlapped, and aligned at a tilted angle with the AOD image on the SSH, thereby recording a spatial spectral grating in the Tm^{3+}:YAG crystal. The magnification of the imaging system was chosen as M=0.6 to optimally project a 4.3 mm (Gaussian $1/e^2$ width) aperture of the AOD, corresponding to 6.9 μs of delay into a 2.6 mm $\times$ 50 μm area of the SSH, while taking into consideration various experimental constraints such as the numerical aperture of the available lenses as well as the closest distance that these elements could be placed to the crystal. Since we were illuminating about 4mm of the AOD, in which the acoustic velocity was 0.62 mm/μs, the spatio-temporal diffraction from the AOD recorded a linearly increasing time delay ramp at different spatial locations in the IBA crystal, ranging from 0 - 6.4 μs (referenced to the undelayed signal from the AOM). This time delay ramp spanned a little less than the coherence time, T_2, so the available time delay was not be limited by the coherence time but instead by the illuminated aperture of the AOD. During this programming phase, the chopper (located after the cryostat) was closed, thus preventing light from the AOD from reaching the 1-D CCD. In the readout phase shown in Fig. 10, the AOD was turned off, the chopper opened, and the SSB waveform $\tilde{s}(t)$ that was to be correlated (generated by the programming AOM) illuminated the SSH, resulting in a spatio-temporally scanned diffraction $\tilde{s}(t - \frac{x}{v_M})$ in the same direction and with the same velocity, v_M, as the magnified image of the acoustic wave in the AOD had at the time of programming. Around the time of the SSH diffraction, the correlation reference signal $\tilde{r}(t)$ was generated in a second (TIC reference) AOM, and is interfered with the echoed, scanned output from the SSH. The power of the TIC reference beam was set to use about half of the dynamic range of the CCD, so that the correlation peak interference could be optimally detected. The photogenerated charges were locally accumulated on the 1-D CCD for a time T_{CCD} that could be longer than the lifetime T_1 (in this case T_{CCD}=50 ms and $T_B = 10$ ms), as long as the grating was periodically re-written.

The CCD captured a time-integrated, interferometric correlation peak, which was modulated by high spatial-frequency fringes and riding on top of a nonuniform bias that was also corrupted with coherent artifacts, as shown in the upper trace of Fig. 12. The position of the correlation peak depended on the time-delay, τ, between the signals injected into the programming/readout AOM and the TIC-reference AOM (see Fig. 9 & 10). Since the correlation peak is modulated by a spatial carrier, high-pass filtering eliminated the slowly-varying bias term, as well as most of the fixed pattern and coherent artifact noise, as shown in the second trace. Finally, to get the incoherent correlation peak, the spatial carrier was removed by down conversion, giving the final correlation peak as shown in the lowest trace of Fig. 12, which accurately portrays the 2 μs delay which was present between the signals diffracted off the SSH and the TIC reference AOM.

Next, we investigated the range of delays that could be detected by the SSH time-integrating correlator by incrementally increasing the delay between the signal and the reference. Figure 13 is an overlay of several of the resulting correlation peaks produced in real-time by the CCD through digital high pass filtering, mod-squaring, and low-pass filtering, and shows delay measurements from
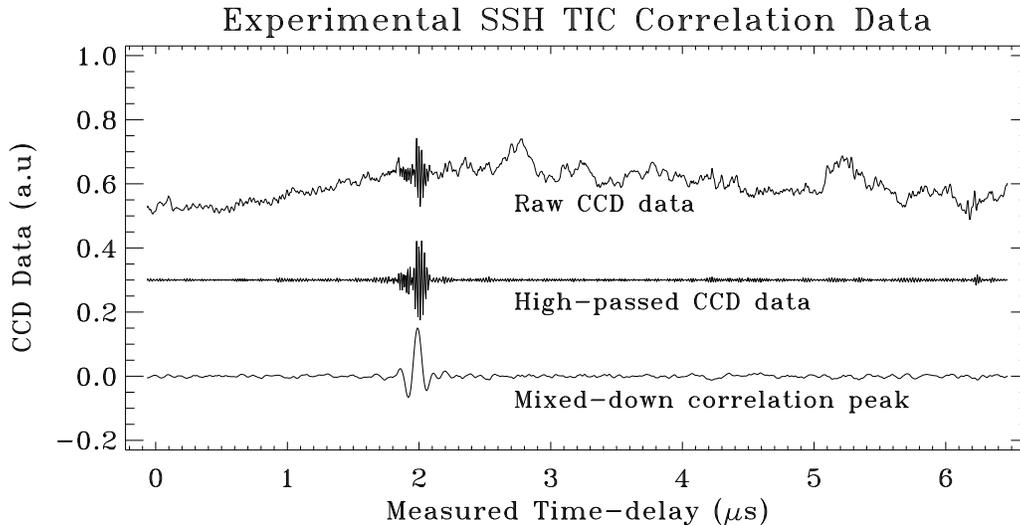
Figure 12: Experimental spatial-spectral holographic time-integrated correlation data captured on the 1-D CCD for identical but delayed 30 MHz chirps applied to the two acousto-optic modulators. Raw data from the CCD has a bias term with a Gaussian profile and some amount of coherent background noise due to dust on the optical components or multiple reflections in the uncoated cryo windows. High-pass filtering removes the bias and most of the noise, but allows the modulated correlation peak to remain due to the high frequency spatial carrier. Digital down conversion to base-band highlights the correlation peak envelope as shown in the bottom trace.

0.5 - 5.5 μs, although peaks were visible from 0 - 6 μs. Even though the correlation peak shape differs slightly from that in Fig. 12. The difference in peak shape is due to the limited functionality of the CCD's onboard signal processing. In particular, whereas the data in Fig. 12 was downconverted by downconversion in the spectral domain, the data in Fig. 13 was just mod-squared, and then low-pass filtered. The resulting FWHM of both types of processing is, however, identical at 40ns. Figure 14 The ratio of processable time-delay to the correlation peak width gives the number of resolvable time-delays, as well as the number of resolvable spots that were programmed into the SSH by the AOD – in our case $N_{\text{SSH}} = \frac{6\mu s}{40 \text{ns}} = 150$.

For an AO-TIC system with the same time-aperture and bandwidth, the fundamental limit on the number of resolvable spots is given by the AOD's time-bandwidth product, which for the overlapping 3dB bandwidth of the AOD and AOM of $B = 30$MHz and Gaussian $1/e^2$ illuminated AOD aperture of $T_A = 6\mu s$ yields $N_{\text{AO}} = T_A B_A = 180$. The nonuniformity across the correlation window for both the AO-TIC and SSH-TIC were limited by the spatial profile of the TIC correlation reference beam and the beam illuminating the AOD, as well as acoustic attenuation in the AOD, while the SSH-TIC was also limited by the AOM intensity profile at the SSH and by the T_2 coherence lifetime. These experiment shows that there was little if any additional degradation due to the use of a spatial-spectral holographic copy of the AOD for the traveling-wave deflector in the interferometric time-integrating correlator, rather than the AOD itself. The biggest detriment appears to be the exponential decay due to the coherence lifetime, T_2.

The SSH scanner behaves precisely like an acousto-optic device that is illuminated by an appropriate Bragg-matched CW beam with one small, but imporant difference, which will be explained here. In some systems AODs are illuminated by modulated beams, or one AOD is imaged onto
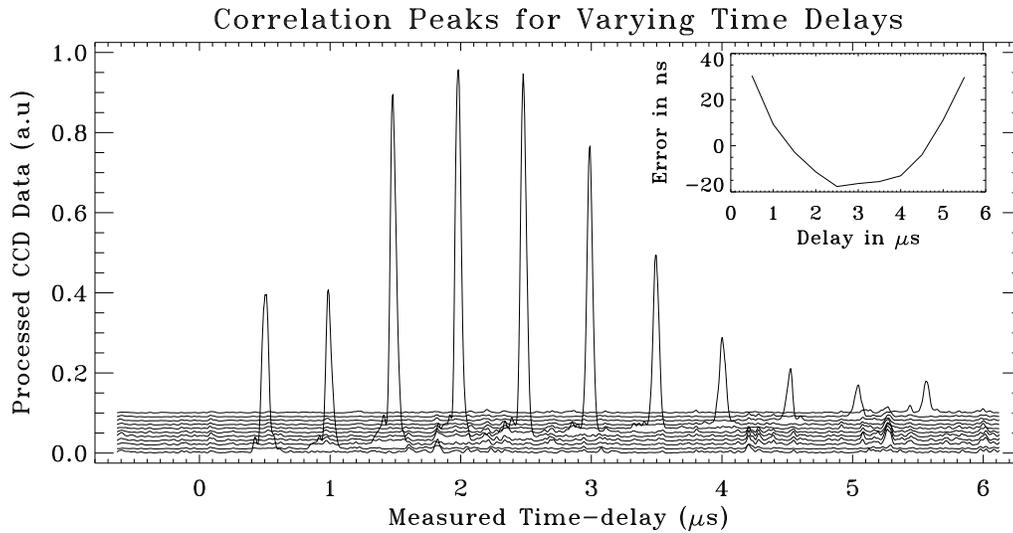
Figure 13: SSH-TIC output for varying time-delays showing 11 of the 150 independently resolvable time delays. This data is processed in real-time by the CCD post processing electronics, first it is high pass filtered, then it is mod-squared and low-pass filtered to produce the correlation envelopes. The peak height varies due to beam-overlap and beam-shape effects, as well as possible variations of the SSH diffraction efficiency across its scan window due to laser linewidth, beam profile, and coherence time effects. The peak position is quite linear compared to the known time delay with a small quadratic error of less than the peak width, possibly due to distortion in the imaging system, rather than any effect of the SSH scanner.
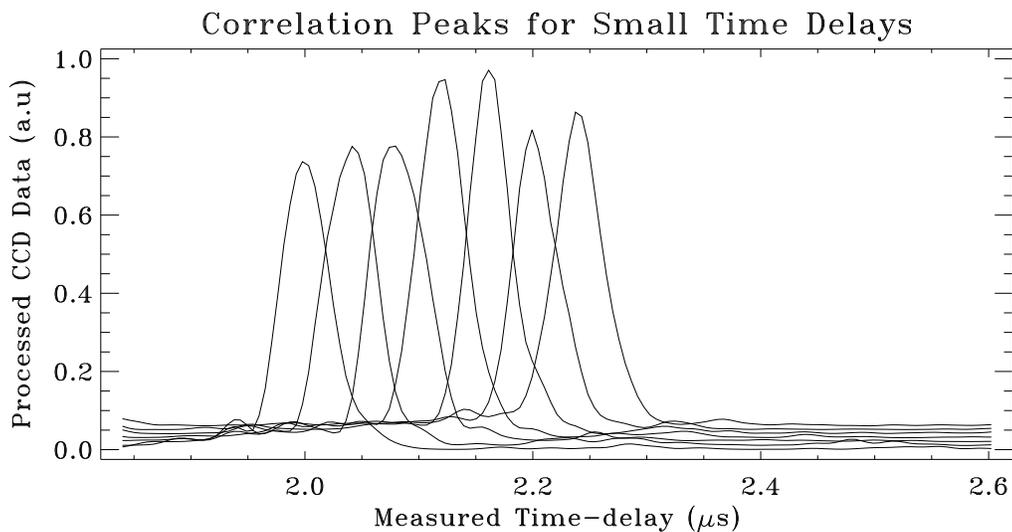

Figure 14: Detailed view of smaller range of delays for SSH time-integrating correlator. By varying the delays of the TIC reference in 40 ns increments from 2 μs to 2.24 μ the FWHM of 40ns becomes clearly visible.

another and the multiply diffracted output is used.[9] In these type of multiplicative geometries the AOD generates new frequencies given by sum or difference of applied RF frequencies, and it is im-

portant to realize that in this regard the SSH scanner is fundamentally different than an AOD. The SSH acts as a programmable spatio-temporal filter that can arbitrarily spatially rearrange existing temporal frequency components that are incident on the spatial-spectral hologram, but since there are no moving gratings in an SSH as there are in an AOD, no new temporal frequency components can be generated. For this reason, the SSH scanner cannot be used as a replacement for an AOD in multiplicative acousto-optic signal processors, but instead can only be used in systems that only use one AO device in series, such as the power spectrum analyzer,[6] acousto optic signal excisors,[15] or in additive architectures that achieve signal multiplication through an interferometric combination of modulated fields as in the interferometric time-integrating correlator presented here. Another interesting possibility is a hybrid system that uses AODs for low bandwidth multiplicative operations, and combines these with SSH scanners for ultra-wide bandwidth additive interferometric optical signal processing. For example by combining the one-dimensional SSH TIC demonstrated here with a pair of multiplicative AODs driven by counter-propagating chirp waveforms it is possible to make an array of Doppler compensated correlation outputs as required for a time-integrating ambiguity function processor.[16]

Since we have demonstrated the ability to precisely copy the behavior of an AOD into a spatial-spectral hologram by appropriately programming it, and then using it in a system normally implemented using the AOD, one must wonder why this was useful, since the holographic copy of the AOD had all of the limitations of the AOD in terms of bandwidth, time-aperture, and resulting time-bandwidth (TB) product.

The answer is that the spatial-spectral holographic scanner can be programmed with a combination of AODs and high bandwidth optical sources (either chirped lasers or modulated stabilized signals), much like that used for the TTD frequency shift ramps explained in section 2. Using such a combination would allow the programming of scanners that have the high spatial resolution of AOD Bragg cells (thousands of spots), but with the bandwidths of chirped lasers (10's, maybe 100's of GHz). For example, by using a chirped laser or a modulated CW laser that is syncronized with a scanner, Le Gouët et. al. have shown how to produce a scanner similar to the one demonstrated here, but without the acousto-optic bandwidth restriction. Their system is instead limited only by the material bandwidth and linear sweep range of the frequency scanned laser.[6] In their approach they combine the spatial deflection of a pair of AODs with a frequency tunable ECDL. By linearly sweeping both the laser's frequency as well as the angle at which the light illuminates the SSH, they were able to record an SSH that maps input frequencies covering up to 3 GHz to unique diffraction angles, thus performing an operation that is similar to that of an acousto-optic Bragg cell. This approach also enables the dynamic reprogramming of the SSH bandwidth and scan range enabling spectral zooming onto features of interest within a rapid reprogramming time of only 10 ms for Er^{3+} or Tm^{3+} based materials.[7] However, since the phase of the ECDL as it's frequency swept is not necessarily continuous, adjacent spectral channels are not likely to be coherent with each other. Therefore, if their SSH scanner was used in an experiment such as the time-integrating correlator, the random phases of the various spectral bins would cause the correlation peak to be blurred out at best, and probably completely indistinguishable.

The principal goals in the presented experiments were to provide an initial demonstration of the fully-coherent time-domain scanning functionality of the SSH scanner, and its complete equivalence to an AOD within the context of an interferometric time-integrating correlator, thereby unambiguously demonstrating the spatio-temporal wavefront reconstruction capabilities of the SSH. We also investigated the limitations on resolution, the requirements for laser power and accumulation and the approaches to read-write multiplexing, all of which would be similar to the TTD frequency

ramp generator in section 2.

4 Conclusion

In this project, we demonstrated the programmable generation of an array of temporal frequencies linearly varying in space that is required to create a TTD ramp for broad-band antenna-array beamsteering using OCT signal processing. The OCT TTD generator was demonstrated by MSU, showing that the individual components of the broad-band array beamforming processor function as predicted. All that is needed to demostrate the full array processor is to build an optical front-end, and integrate all of the individual components. The second major experiment toward this project was an OCT-based time-integrating correlator. This experiment illustrated that parallel arrays of OCT processors can indeed be recorded and read out phase-coherently, illustrating the parallel processing capability that these materials possess.

References

[1] J. L. Legouet, "Rf spectrometer based on spectral hole burning." French Patent application FR 098 2 626.

[2] K. D. Merkel, W. R. Babbitt, K. E. Anderson, and K. H. Wagner, "Variable-time-delay optical coherent transient signal processing," *Opt. Lett.*, vol. 24, 1999.

[3] G. R. Knight, "Holographic associative memory and processor," *Applied Optics*, vol. 14, pp. 1088–1092, 1975.

[4] I. C. Chang and D. L. Hecht, "Characteristics of acoustooptic devices for signal processors," *Optical Engineering*, vol. 21, pp. 76–81, 1982.

[5] L. Menager, I. Lorgere, J. L. Le Gouet, D. Dolfi, and J. P. Huignard, "Demonstration of a radio-frequency spectrum analyzer based on spectral hole burning," *Opt. Lett.*, vol. 26, pp. 1245–1247, 2001.

[6] I. Lorgere, L. Menager, V. Lavielle, J. L. Gouet, D. Dolfi, S. Tonda, and J. Huignard, "Demonstration of a radio-frequency spectrum analyser based on spectral hole burning," *J. Mod. Optics*, vol. 49, p. 2459, 2002.

[7] V. Lavielle, I. Lorgere, J. L. Gouet, S. Tonda, and D. Dolfi, "Wideband versatile radio-frequency spectrum analyser," *Optics Letters*, vol. 28(6), p. 384, Mar 15 2003.

[8] P. Kellman and T. R. Bader, "Acoustooptic channelized receivers," *Optical Engineering*, vol. 23, pp. 2–6, 1984.

[9] J. W. Goodman, *Introduction to Fourier optics.* McGraw-Hill, 1968.

[10] J. Shamir and K. Wagner, "Generalized Bragg selectivity in volume holography," *Applied Optics*, vol. 41, pp. 6773–6785, 2002.

[11] T. Turpin, "Time integrating optical processors," *SPIE - Real-Time Signal Processing*, vol. 154, 1978.

[12] P. Kellman, *Time-integrating optical signal processing.* PhD thesis, Stanford Univ., 1979.

[13] R. Reibel, Z. Barber, M. Tian, and W. R. Babbitt, "Temporally overlapped linear frequency-chirped pulse programming for true-time-delay applications," *Optics Letters*, vol. 27, no. 7, p. 494, 2002.

[14] K. D. Merkel, R. K. Mohan, Z. Cole, A. Chang, T. andOlson, and W. R. Babbitt, "Multi-gigahertz radar range processing of baseband and rf carrier modulated signals in Tm:YAG," *Journal of Luminescence*, vol. current volume, p. unknown, 2003.

[15] D. W. Jackson and J. L. Erickson, *Acousto-Optic Signal Processing*, pp. 107 – 137. Dekker, 1983.

[16] J. D. Cohen, "Ambiguity processor architecture using one-dimensional acousto-optic transducers," in *Real-time signal processing II*, vol. SPIE 180, pp. 134–142, 1979.